# NAVAL POSTGRADUATE SCHOOL

MONTEREY, CALIFORNIA

# DISSERTATION

**AIR-SEA ENTHALPY AND MOMENTUM EXCHANGE AT MAJOR HURRICANE WIND SPEEDS**

by

Michael Monroe Bell

June 2010

Dissertation Supervisor: Michael Montgomery

**Approved for public release; distribution is unlimited**

THIS PAGE INTENTIONALLY LEFT BLANK

| REPORT DOCUMENTATION PAGE | | | *Form Approved OMB No. 0704-0188* |
|---|---|---|---|
| Public reporting burden for this collection of information is estimated to average 1 hour per response, including the time for reviewing instruction, searching existing data sources, gathering and maintaining the data needed, and completing and reviewing the collection of information. Send comments regarding this burden estimate or any other aspect of this collection of information, including suggestions for reducing this burden, to Washington headquarters Services, Directorate for Information Operations and Reports, 1215 Jefferson Davis Highway, Suite 1204, Arlington, VA 22202-4302, and to the Office of Management and Budget, Paperwork Reduction Project (0704-0188) Washington DC 20503. | | | |
| **1. AGENCY USE ONLY** (*Leave blank*) | **2. REPORT DATE** June 2010 | **3. REPORT TYPE AND DATES COVERED** Dissertation | |
| **4. TITLE AND SUBTITLE:** Air-Sea Enthalpy and Momentum Exchange at Major Hurricane Wind Speeds | | **5. FUNDING NUMBERS** | |
| **6. AUTHOR(S) Michael Monroe Bell** | | | |
| **7. PERFORMING ORGANIZATION NAME(S) AND ADDRESS(ES)** Naval Postgraduate School Monterey, CA  93943-5000 | | **8. PERFORMING ORGANIZATION REPORT NUMBER** | |
| **9. SPONSORING / MONITORING AGENCY NAME(S) AND ADDRESS(ES)** Office of Naval Research Arlington, VA 22203 National Science Foundation Arlington, VA 22230 | | **10. SPONSORING / MONITORING AGENCY REPORT NUMBER** | |
| **11. SUPPLEMENTARY NOTES**  The views expressed in this thesis are those of the author and do not reflect the official policy or position of the Department of Defense or the U.S. Government. IRB Protocol number _____. | | | |
| **12a. DISTRIBUTION / AVAILABILITY STATEMENT** Approved for public release; distribution is unlimited | | **12b. DISTRIBUTION CODE** | |

**13. ABSTRACT (maximum 200 words)**

Air–sea exchanges of heat and momentum are important elements in understanding and skillfully predicting tropical cyclone intensity, but the magnitude of the corresponding wind-speed dependent bulk exchange coefficients is largely unknown at major hurricane wind speeds greater than 50 m s$^{-1}$. Since direct turbulent flux measurements in these conditions are extremely difficult, the momentum and enthalpy fluxes were alternatively deduced via axisymmetric angular momentum and total energy budgets. A comprehensive error analysis was performed using both idealized numerical simulations to quantify and mitigate potentially significant uncertainties resulting from unresolved budget terms and observational errors. An analysis of six missions from the 2003 CBLAST field program in major hurricanes Fabian and Isabel was conducted using a new variational technique. This analysis indicates a near-surface mean drag coefficient ($C_D$) of $2.4 \times 10^{-3}$ with a 46% standard deviation and a mean enthalpy coefficient ($C_K$) of $1.0 \times 10^{-3}$ with a 40% standard deviation for wind speeds between 52 and 72 m s$^{-1}$. These are the first known estimates of $C_K$ and the ratio of enthalpy to drag coefficient ($C_K/C_D$) in major hurricanes. The results suggest that there is no significant change in the magnitude of the bulk exchange coefficients estimated at minimal hurricane wind speeds, and the ratio $C_K/C_D$ is likely less than 0.75 for wind speeds greater than 50 m s$^{-1}$.

| **14. SUBJECT TERMS**   Air-sea interaction, tropical cyclones, surface fluxes, drag coefficient, CBLAST | **15. NUMBER OF PAGES** 155 |
|---|---|
| | **16. PRICE CODE** |

| **17. SECURITY CLASSIFICATION OF REPORT** Unclassified | **18. SECURITY CLASSIFICATION OF THIS PAGE** Unclassified | **19. SECURITY CLASSIFICATION OF ABSTRACT** Unclassified | **20. LIMITATION OF ABSTRACT** UU |
|---|---|---|---|

THIS PAGE INTENTIONALLY LEFT BLANK

# AIR-SEA ENTHALPY AND MOMENTUM EXCHANGE AT MAJOR HURRICANE WIND SPEEDS

Michael M. Bell
Civilian, United States Navy
B.A., University of Florida, 1996
B.S., Metropolitan State College of Denver, 2001
M.S., Colorado State University, 2006

Submitted in partial fulfillment of the
requirements for the degree of

**DOCTOR OF PHILOSOPHY IN METEOROLOGY**

from the

**NAVAL POSTGRADUATE SCHOOL
June 2010**

Author:          _____
                                    Michael M. Bell

Approved by:

_____          _____
Michael Montgomery                    Kerry Emanuel
Professor of Meteorology              Professor of Meteorology
Dissertation Supervisor


_____          _____
Russell Elsberry                      Patrick Harr
Professor of Meteorology              Professor of Meteorology


_____          _____
Qing Wang                             Francis Giraldo
Professor of Meteorology              Professor of Mathematics


Approved by:    _____
                    Philip Durkee, Chair, Department of Meteorology

Approved by:    _____
                    Douglas Moses, Associate Provost for Academic Affairs

THIS PAGE INTENTIONALLY LEFT BLANK

# ABSTRACT

Air–sea exchanges of heat and momentum are important elements in understanding and skillfully predicting tropical cyclone intensity, but the magnitude of the corresponding wind-speed dependent bulk exchange coefficients is largely unknown at major hurricane wind speeds greater than 50 m s$^{-1}$. Since direct turbulent flux measurements in these conditions are extremely difficult, the momentum and enthalpy fluxes were alternatively deduced via axisymmetric angular momentum and total energy budgets. A comprehensive error analysis was performed using both idealized numerical simulations to quantify and mitigate potentially significant uncertainties resulting from unresolved budget terms and observational errors. An analysis of six missions from the 2003 CBLAST field program in major hurricanes Fabian and Isabel was conducted using a new variational technique. This analysis indicates a near-surface mean drag coefficient ($C_D$) of $2.4 \times 10^{-3}$ with a 46% standard deviation and a mean enthalpy coefficient ($C_K$) of $1.0 \times 10^{-3}$ with a 40% standard deviation for wind speeds between 52 and 72 m s$^{-1}$. These are the first known estimates of $C_K$ and the ratio of enthalpy to drag coefficient ($C_K/C_D$) in major hurricanes. The results suggest that there is no significant change in the magnitude of the bulk exchange coefficients estimated at minimal hurricane wind speeds, and the ratio $C_K/C_D$ is likely less than 0.75 for wind speeds greater than 50 m s$^{-1}$.

THIS PAGE INTENTIONALLY LEFT BLANK

# TABLE OF CONTENTS

THIS PAGE INTENTIONALLY LEFT BLANK

# LIST OF FIGURES

THIS PAGE INTENTIONALLY LEFT BLANK

# LIST OF TABLES

THIS PAGE INTENTIONALLY LEFT BLANK

# LIST OF ACRONYMS AND ABBREVIATIONS

| | |
|---|---|
| ASIST | Air-Sea Interaction Saltwater Tank |
| AXBT | Airborne expendable bathythermograph |
| AVHHR | Advanced Very High Resolution Radiometer |
| BM08 | Bell and Montgomery (2008) |
| CBLAST | Coupled Boundary Layers Air-Sea Transfer Experiment |
| $C_D$ | Bulk momentum exchange coefficient |
| $C_E$ | Bulk moisture exchange coefficient |
| $C_K$ | Bulk enthalpy exchange coefficient |
| Dropsonde | NCAR GPS dropwindsonde |
| E-PI | Emanuel's Potential Intensity |
| GPS | Global Positioning System |
| HEXOS | Humidity Exchange Over the Sea |
| NCAR | National Center for Atmospheric Research |
| NWP | Numerical Weather Prediction |
| NOAA | National Oceanic and Atmospheric Administration |
| PTH | Pressure, Temperature, relative Humidity |
| RE87 | Rotunno and Emanuel (1987) |
| RMW | Radius of Maximum Wind |
| SAMURAI | Spline Analysis at Mesoscale Utilizing Radar and Aircraft Instrumentation |
| SST | Sea-Surface Temperature |
| TC | Tropical Cyclone |
| TCBL | Tropical Cyclone Boundary Layer |

| | |
|---|---|
| TRMM | Tropical Rainfall Measuring Mission |
| TMI | TRMM Microwave Imager |
| USAF | United States Air Force |
| VAR | Variational |
| WRF | Weather Research and Forecasting Model |

# ACKNOWLEDGMENTS

THIS PAGE INTENTIONALLY LEFT BLANK

# I.  INTRODUCTION

Heat, moisture, and momentum exchange at the air–sea interface are primary processes in hurricane intensification and maintenance with important theoretical and practical implications (Kleinschmidt 1951; Malkus and Riehl 1960; Ooyama 1969; Emanuel 1986, 1995b). Wind-speed dependent bulk aerodynamic formulas often are used to represent the turbulent fluxes associated with air-sea interactions, relying on drag ($C_D$), moisture ($C_E$), and enthalpy ($C_K$) exchange coefficients. However, as Ooyama (1969) stated, "Unfortunately, there is little information on $C_E$ under hurricane conditions, other than the semispeculative guess that the exchange coefficients of latent heat, sensible heat and momentum are probably of the same magnitude." Nearly 40 years after that pioneering study, enthalpy and momentum exchange coefficients are still largely unknown at major hurricane wind speeds (>50 m s$^{-1}$, equivalent to category three and higher on the Saffir-Simpson scale). There are known sensitivities of theoretical and numerical models of major hurricanes to the magnitude of these exchange coefficients. It is therefore important to improve our understanding and forecasts of these phenomena, given the high impact that their damaging winds and storm surge can have on coastal populations, global economics, marine, and Naval operations.

It is very difficult to directly measure hurricane surface layer fluxes over the ocean due to the extreme conditions and challenging deployment of instrumentation. In situ measurements by ships or manned aircraft are very hazardous, and fixed sensors are unlikely to be in the correct location or robust enough to obtain the needed measurements. Due to these hazards and difficulties in obtaining direct air-sea flux measurements, only fluxes at higher altitudes and minimal hurricane force winds have been obtained (Black et al. 2007; French et al. 2007; Drennan et al. 2007; Zhang et al. 2008). Measurements of the drag and enthalpy exchange coefficients at high wind speeds also have been made in laboratory experiments (Donelan 2004; Haus et al. 2010), but are limited to wind speeds less than ~50 m s$^{-1}$. Global positioning system (GPS) dropwindsonde profiles were used to calculate flux profiles and deduce the drag coefficient at the highest wind speeds yet (Powell et al. 2003; Vickery et al. 2009), but

this technique has not been attempted for retrieving the enthalpy exchange coefficient. Indirect retrievals of the drag coefficient in hurricanes have been conducted using ocean measurements (Shay and Jacob 2006; Jarosz et al. 2007), but this methodology is not applicable for deducing enthalpy exchange coefficients.

An indirect approach to retrieving momentum exchange using an angular momentum budget was originally proposed over fifty years ago (Palmen and Riehl 1957). In this formulation, the surface stress is obtained by measured transports of absolute angular momentum in an axisymmetric cylindrical coordinate system. If the flux of this quantity is known at the top and sides of a prescribed control volume, the flux at the air-sea interface can be obtained via residual. A similar budget can be derived for total energy to deduce the enthalpy exchange coefficient. The central focus of this research was the application of this budget method to major hurricanes using recent observations. After Palmen and Riehl (1957) introduced the budget methodology, additional studies used the angular momentum budget to deduce the drag coefficient with improved datasets (Miller 1962, 1964; Hawkins and Rubsam 1968; Hawkins and Imbembo 1976). The quality and density of hurricane observations has improved significantly since that time, as well as the analysis techniques used to composite the data.

In practical application for this dissertation research, some of the budget terms were very difficult to calculate with observational data, and known uncertainties also must be acknowledged. To gain insight into the relative importance of the various sources of error in the energy/momentum budget method, the sensitivity to errors in unresolved budget terms, sea-surface temperature (SST), center placement, gridding method, and size of control volume were examined systematically using numerical model data where the surface fluxes were known. These results were then utilized to determine a quantitative estimate of the confidence level of the magnitude of the retrieved bulk exchange coefficients. A high-resolution dataset collected in Hurricanes Fabian and Isabel (2003) as part of the Coupled Boundary Layers Air-Sea Transfer (CBLAST) experiment (Black et al. 2007) was used to apply this energy/momentum budget method to real tropical cyclones. Both tropical cyclones (TCs) achieved category four intensity and the data collected present a significant advance in the measurement of major hurricanes. Although comprehensive analyses of the structure of

Hurricane Isabel have been performed elsewhere using dropsonde, in situ flight level, Doppler radar, and satellite data (Montgomery et al. 2006; Aberson et al. 2006; Bell 2006; Bell and Montgomery 2008), one unique aspect of the dataset has yet to be fully utilized. A series of rapid dropsonde releases in the eyewall region of these two hurricanes were performed to accurately construct control volume composites for use in the budget method. These dropsonde "sequences" are used in conjunction with Doppler radar, in situ, and radiometer data to construct composite analyses for the air-sea exchange calculations presented in this dissertation.

To deduce momentum and energy fluxes from these sequences, the data must be gridded in an axisymmetric coordinate system moving with the tropical cyclone. A simple objective analysis scheme (Barnes 1973) was used in the previous Isabel studies to obtain the kinematic and thermodynamic structure. Recent advances in data assimilation techniques will be used here to improve this analysis by deriving a variational procedure that provides a maximum likelihood estimate of the gridded structure given estimates of background and observational errors. Additionally, this system allows for the incorporation of Doppler radar data, which increases the spatial coverage and improves the kinematic measurements in the analysis. This integrated variational technique also can provide a unique framework for future theoretical TC studies and numerical model initialization.

To provide a broad scientific context for the current research, Chapter II is a review of relevant previous studies on air-sea fluxes in tropical cyclones. A derivation of the equations for total energy and angular momentum conservation in an axisymmetric, cylindrical coordinate system necessary for calculations using the budget method is provided in Chapter III, and this is followed by a comprehensive error analysis. This error analysis includes results from numerical simulations of a hurricane vortex, wherein the sensitivities to simulated observational deficiencies are explored. The variational methodology for deducing the axisymmetric tropical cyclone structure from real observations is described in Chapter IV. The results of the analysis using the described methods are presented in Chapter V. The concluding chapter summarizes the key findings of this study and discusses potential implications for both theoretical understanding of hurricane intensity and numerical weather.

THIS PAGE INTENTIONALLY LEFT BLANK

## II.    TROPICAL CYCLONE SURFACE FLUXES

## A.    THEORETICAL AND PRACTICAL IMPLICATIONS

Reynolds decomposition of the momentum and thermodynamic equations leads to the well-known turbulence closure problem, in which the number of unknown variables exceeds the number of equations for the prediction of atmospheric flow (Stull 1988). In the surface layer, where the turbulent fluxes are nearly constant, the fluxes are often parameterized by bulk aerodynamic formulae that require wind-speed dependent exchange coefficients for momentum, heat, and moisture. In a tropical cyclone, the surface stress can be represented in a cylindrical coordinate system in which the tangential (swirling) wind is the dominant component as

$$\tau_{z\theta} \equiv -\overline{\rho w'v'} = C_D \rho \, | \vec{u}_h | \, v \tag{2.1}$$

where $v$ denotes the tangential wind, $w$ the vertical wind, $\rho$ the density, $| \vec{u}_h |$ the horizontal wind speed, $C_D$ the drag coefficient, primes denote perturbation quantities, and the overbar is a Reynolds averaging operator. In the axisymmetric coordinate system used in this study, the Reynolds averaging operator encompasses both azimuthal and temporal averaging. A similar expression for the enthalpy flux can be derived:

$$F_{zk} = F_{zT} + F_{zq} \equiv \overline{\rho} c_p \overline{w'T'} + \overline{\rho} L \overline{w'q'} = C_K \overline{\rho} \, | \vec{u}_h | \, (k^* - k) \tag{2.2}$$

where $T$ denotes the temperature, $c_p$ the specific heat of air, $L$ the latent heat of vaporization, $q$ the water vapor, $k$ the enthalpy, $k^*$ the saturation enthalpy at the sea surface, and $C_K$ the bulk enthalpy exchange coefficient (Emanuel 1995). Since the ocean surface characteristics change significantly with increasing wind speed (Black et al. 1986), a simple extrapolation of the bulk exchange coefficient magnitudes derived at low wind speeds to 50 m s$^{-1}$ and beyond is not necessarily justified. Emanuel (2003) presented a similarity hypothesis for enthalpy and drag coefficients at very high wind speeds using dimensional analysis, and proposed that their magnitudes become independent of wind speed at approximately hurricane force and higher (>33 m s$^{-1}$). That analysis suggested also that the enthalpy coefficient should vary as a function of

5

temperature, such that the ratio $C_K/C_D$ would be approximately unity at typical near-surface air temperatures in major hurricanes. The earlier work of Ooyama (1969), Rosenthal (1971), and Emanuel (1986, 1995) suggests a strong dependence of $C_K/C_D$ on intensity. Therefore, validating or rejecting these hypotheses about the behavior of the bulk exchange coefficients at major hurricane wind speeds has important implications for tropical cyclone intensity theory and numerical weather prediction (NWP).

The importance of air-sea energy and momentum exchange in hurricanes was first introduced by Kleinschmidt (1951) in the form of an energy balance between the amount of sensible and latent heat a TC can extract from the ocean surface and the momentum lost to the sea through frictional dissipation. Malkus and Riehl (1960) presented a potential intensity (PI) theory based on the concept of a steady-state TC at maximum intensity that maintains this energy balance, and they derived an expression for the maximum tangential wind of a TC given the a priori SST, air temperature, and bulk heat and momentum exchange coefficients. While they acknowledged the importance of latent heat fluxes from the sea surface, the bulk moisture exchange coefficient was not explicitly included in their equation for maximum tangential wind. Ooyama (1969) and Rosenthal (1971) were the first to explicitly link the flux of water vapor, or latent heat, with numerically simulated hurricane intensity. Emanuel (1986) expanded these concepts and derived an expression for maximum intensity assuming a steady-state balance between the amount of energy obtained from the ocean and that dissipated by friction in the boundary layer, which is similar in general terms to that presented by Kleinschmidt (1951) and Malkus and Riehl (1960). The primary parameters that govern Emanuel's PI (E-PI) are the sea-surface temperature, the outflow temperature, boundary layer relative humidity, and the ratio of the bulk enthalpy ($C_K$) and momentum ($C_D$) exchange coefficients ($C_K/C_D$). Due to limited high-resolution surface flux measurements in the extreme conditions of a hurricane eyewall, exchange coefficients are the most uncertain of these parameters at wind speeds above category one (Black et al. 2007).

Bell (2006), Montgomery et al. (2006), and Bell and Montgomery (2008) carried out an extensive test of the E-PI predictions using observations collected during Hurricane Isabel as part of the 2003 CBLAST field program. Since little guidance existed

for the magnitude of the bulk exchange coefficients at major hurricane wind speeds for the main potential intensity estimate, the ratio of bulk enthalpy and momentum exchange coefficients was assumed to be unity ($C_K/C_D = 1$). The range of E-PI estimates from Bell and Montgomery (2008) is ~30 m s$^{-1}$ by changing the assumptions in the calculations (Fig. 1, note that all figures appear at the end of the subsections). The upper-bound estimate neglects entirely the ocean cooling, includes dissipative heating, and assumes that $C_K/C_D = 1$. The lower-bound estimate assumes $C_K/C_D = 0.5$ and that the ocean cooling effect is compensated by the dissipative heating effect. Accurate determination of the bulk exchange coefficients would clearly help narrow the uncertainty of these estimates.

Recent research (Smith et al. 2008; Bryan and Rotunno 2009) has suggested that the primary discrepancy between observed and simulated axisymmetric intensities and the E-PI theoretical limit and is due to the implicit assumption of gradient wind balance in the boundary layer. In three-dimensional simulations by Montgomery et al. (2010), the maximum intensity has a much lower sensitivity to the surface drag coefficient than in the axisymmetric simulations. The role of radial transport of moist entropy across the eye-eyewall interface in two dimensions (Persing and Montgomery 2003) and three dimensions (Eastin et al. 2002; Cram et al. 2003) is also not currently included in PI theory. While it is clear that a revised PI theory will need to be developed to address these legitimate limitations, this does not diminish the importance of estimating surface fluxes at high wind speeds as part of accurate determination of hurricane maximum intensity.

The importance of understanding of air-sea exchange at high wind speeds is not limited to the theoretical domain. While tropical cyclone track forecasts have been found to be relatively insensitive to the parameterization of surface fluxes of enthalpy and momentum, the ability to skillfully predict tropical cyclone intensity and structure has been found to be dependent on meaningful and accurate parameterization of these processes (Davis et al. 2008). Ooyama (1969) was the first to demonstrate the importance of parameterized air-sea fluxes for growth and maintenance of a tropical cyclone using a simplified three-layer model of the moist atmosphere. Rosenthal (1971) and Rotunno and

Emanuel (1987) further demonstrated this importance in hurricane models, and Emanuel (1995) demonstrated sensitivity of the simulated intensity to the prescribed surface exchange coefficients in a simplified model framework. Subsequent studies by Braun and Tao (2000), Bao et al. (2002), and Davis et al. (2008) using full physics models have also shown the sensitivity of hurricane intensity forecasts to modifications in the surface roughness length parameterization used to calculate heat and momentum fluxes. Hurricane simulations using the Navy Coupled Ocean/Atmosphere Mesoscale Prediction System are also sensitive to the surface flux and sea spray parameterizations (J. Doyle 2009, personal communication). Despite improvements in the quality of the intensity guidance available to forecasters at the National Hurricane Center, relatively little improvement has been achieved in the forecast of tropical cyclone intensity since 1990 (Rappaport et al. 2009). Reducing errors in the numerical weather model representation of air-sea interaction in major tropical cyclones would likely contribute to improved intensity forecasts issued by the Joint Typhoon Warning Center and the National Hurricane Center.
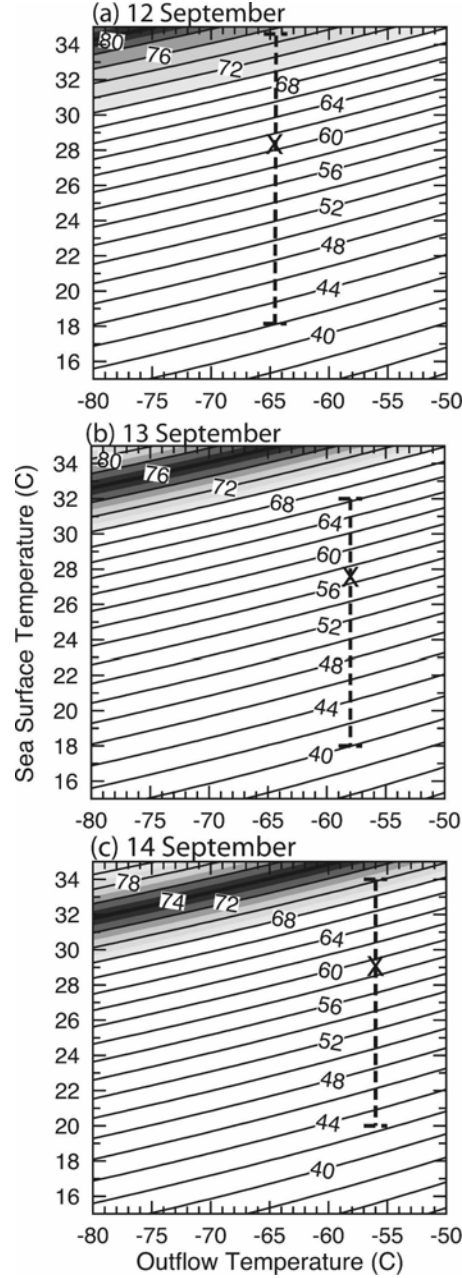
Figure 1. Theoretically predicted azimuthal mean $V_{max}$ at the boundary layer top for varying outflow temperature and near-core SST with a constant RH = 80% (dashed line). 'X' indicates the primary potential intensity estimate for the observed near environment around Isabel (using 27.5 °C SST near eyewall region associated with Fabian's wake), which yields a 56.6 m s$^{-1}$ mean $V_{max}$. The dark solid curve represents the average storm-relative tangential wind speed at the top of the boundary layer derived from the dropwindsonde measurements. The shading represents the 6 m s$^{-1}$ standard deviation of this mean value. This a priori E-PI estimate assumes $C_K/C_D$ =1. From Bell and Montgomery (2008).

## B.	PREVIOUS SURFACE FLUX OBSERVATIONS

Surface fluxes are typically measured by one of three methods–eddy correlation, inertial dissipation, or flux-profile relationships. Each of these methods has different advantages and disadvantages depending on the measurement apparatus and field conditions, but all three present difficulties in the TCBL. At major hurricane wind speeds, the main challenge for these types of measurements is placement and robustness of the sensors. Given that the spatial and temporal occurrence of these wind speeds is very small compared to the ocean basin size and seasonal timescales in which hurricanes occur, the probability of a fixed sensor encountering them is very low. Additionally, operational ocean sensors (such as buoys) typically are not designed to withstand the extreme conditions found in the open ocean at the base of a major hurricane eyewall, and instrumented ships prudently avoid these conditions as well. Therefore, laboratory experiments and observations from research aircraft deployed in tropical cyclones are currently the most viable choices for obtaining information about surface fluxes at high wind speeds. However, low-altitude flying in the turbulent boundary layer at the base of an eyewall is also very hazardous, which requires that remote sensing or expendables (i.e., dropwindsondes) be used to obtain measurements in this region. This generally limits the use of the eddy correlation or inertial dissipation methods except in special circumstances where it is safe to fly in the boundary layer and the aircraft is equipped with high-resolution sensors. Similarly, the flux-profile method was not viable until the development of the modern NCAR GPS dropwindsonde (Hock and Franklin 1999, hereafter "dropsonde"). It is perhaps not surprising, then, that the first attempts to determine surface fluxes in tropical cyclones were performed by indirect retrievals similar to that proposed in this study.

Palmen and Riehl (1957) reported the first calculation of the drag coefficient in a tropical cyclone using a tangential wind budget using two composite wind fields created by Hughes (1952) at low levels and Jordan (1952) at upper levels. Hughes (1952) analyzed 84 flights from 28 storms in which reconnaissance was available during 1945–1947, while Jordan (1952) used rawinsonde observations collected from islands and coastal stations near tropical cyclones during the period 1945–1951. These two

composites were combined to create an axisymmetric tropical cyclone structure with one degree latitude horizontal resolution and variable vertical resolution for use in the budget calculations. The original resolution of the low-level data was 0.5 degrees with the lowest reported winds at 500 ft (152 m), and no upper-air data were obtained within ~200 km of the center. To derive the surface stress, the tangential momentum equation was integrated from the surface to the top of the inflow layer, assuming steady-state and cylindrical axisymmetry, which yielded:

$$\tau_{z\theta} = \frac{1}{g} \int_{pH}^{p0} \xi_a u \, dp - \frac{1}{g} \int_{pH}^{p0} w \frac{\partial v}{\partial z} \, dp$$

(2.3)

where $\xi_a$ denotes the absolute vorticity $f + \partial(rv)/r\partial r$, and $p0$ and $pH$ are the pressures at the surface and top of the inflow layer, respectively. Vertical motion was derived from the mass continuity equation with a presumed zero boundary condition at the surface. This calculation yielded a $C_D$ of $2.1 \times 10^{-3}$ for the innermost radial ring with a surface layer wind speed of ~26 m s$^{-1}$, but it apparent that this was a coarse estimate given the extensive averaging used to create the dataset. Subsequent budgets of angular momentum and energy were calculated in that study, but no computation of an enthalpy exchange coefficient was attempted.

This budget method was repeated in several subsequent studies with improved datasets. Miller (1962) used an aircraft dataset collected in Hurricane Helene (1958) to extend the Palmen and Riehl (1957) results by using a single storm as opposed to a composite, and at higher surface wind speeds. This study yielded drag coefficients ranging from $2.4 \times 10^{-3}$ to $3.2 \times 10^{-3}$ for winds from 30 to 40 m s$^{-1}$. Aircraft data from Hurricane Donna (1960) were used to calculate drag coefficients of $3.6 \times 10^{-3}$ and $4.19 \times 10^{-3}$ at 36 and 52 m s$^{-1}$, respectively by Miller (1964), as shown in Figure 2. These results indicated that drag coefficient continued to increase with wind speed as storms reached major hurricane intensity. Hawkins and Rubsam (1968) and Hawkins and Imbembo (1976) continued these analyses with Hurricane Hilda (1964) and Hurricane Inez (1966), and extended the wind speed behavior of the drag coefficient to nearly 70 m s$^{-1}$ as shown in Figure 3. To match the maximum drag coefficient of $4.6 \times 10^{-3}$ at 67 m s$^{-1}$ found using the Inez dataset, the least-squares curve fit was changed from linear to

11

quadratic. Hawkins and Rubsam (1968) also included a more comprehensive error analysis of the budget method, calculating the surface stress using both the integrated tangential momentum equation (so-called "vorticity" method) and the angular momentum form, which is similar to the current study. These two methods are analytically equivalent, but produced slightly different numerical results. Also particularly relevant to the current study, Hawkins and Rubsam also compared the results obtained when changing the top of the integration volume from the top of the inflow layer to the top of the atmosphere (100 hPa). The differences between the two integration methods and different boundary conditions suggested an error in the drag coefficient estimates of about ±30%. An energy budget was also calculated, but the $C_H$ and $C_E$ values were assumed to be equal in magnitude to the derived $C_D$, as opposed to being retrieved from the budget itself. In summary, none of these studies using budget methods indicated that the drag would level off or decrease at major hurricane wind speed, and none presented estimates of a heat or enthalpy exchange coefficient. Frank (1984) also used an angular momentum budget to estimate the drag coefficient from a composite analysis of Hurricane Frederic (1979). Frank estimated a ±50% error in $C_D$ using this method by calculating a standard deviation of estimates from different radial bands.

Moss and Rosenthal (1975) used the same aircraft dataset from Hurricane Inez (1966) to calculate the drag coefficient using the Deardorff boundary layer parameterization (Deardorff 1972), and their results compared very favorably to those obtained by Hawkins and Imbembo (1976) using the angular momentum budget. They also provided an estimate of the bulk heat exchange coefficient at 48 m s$^{-1}$, but they admitted that it clearly had a high bias. Moss and Rosenthal also directly compared these drag coefficients with the simple Deacon's formula ($C_D = 1.1 \times 10^{-3} + 4 \times 10^{-5}|V|$) and a formula proposed by Miller (1969, $C_D = 1 \times 10^{-3} + 7 \times 10^{-5}|V|$), and concluded that these equations gave values that were too low at high wind speeds, but too high at low wind speeds for Inez, but were reasonable for the dataset from Hurricane Daisy (1958). Although not specifically conducted in the TCBL, Large and Pond (1981, 1982) performed eddy correlation and inertial dissipation estimates of open ocean heat and momentum exchange in wind speeds up to ~25 m s$^{-1}$, and their results have been

validated by subsequent studies (Smith et al. 1992). These measurements added further support to the hypothesis that the drag coefficient continues to increase with wind speed up to 25 m s$^{-1}$. In contrast, Large and Pond (1982) showed no significant wind speed dependence on the moisture flux in this wind speed range, and this result has also been further validated (DeCosmo et al. 1996).

Powell et al. (2003) used a flux-profile relationship to infer the drag coefficient from dropsonde profiles released in hurricane eyewalls. The wind speed is obtained via the displacement of the dropsonde's GPS position as it descends toward the ocean surface after release from a research aircraft. Although the dropsonde is a Lagrangian measurement as it travels several kilometers downwind as it falls, the wind profiles can be treated in an Eulerian framework by assuming the azimuthal variation in the wind speed is small compared to the vertical variation. Fitting the vertical profile to a least-squares logarithmic line yields the surface roughness ($z_0$) as the intercept and the friction velocity (u*) as the slope from the flux-profile relationship in a neutral surface layer. The implied drag coefficient from these results are plotted with estimates from the earlier budget studies in Figure 4. Powell et al. provided the first indications of a decrease in the drag coefficient from maximum values around ~2.5x10$^{-3}$ at 30-40 m s$^{-1}$. Additional dropsonde profiles have been collected in major hurricanes since the 2003 study, including some used in this research, which have extended the wind speed dependence to near 60 m s$^{-1}$ (Figure 5) with a near constant drag coefficient even at this intensity (Vickery et al 2009).

Additional evidence that the drag coefficient does not increase above ~35 m s$^{-1}$ was reported by Donelan et al. (2004) using laboratory tank measurements. The eddy correlation method was used for wind speeds up to 26 m s$^{-1}$, and a momentum budget retrieval was used for wind speeds from 20–50 m s$^{-1}$. These tank measurements showed a "saturation" of the drag coefficient around hurricane force wind speed (33 m s$^{-1}$), and suggested a limiting aerodynamic roughness of the surface waves above these speeds. The momentum budget approach used in the laboratory has also been utilized in field experiments with ocean current measurements. Shay and Jacob (2006) used airborne expendable current profilers released into Hurricane Gilbert (1988) to estimate the

downward kinetic energy flux and retrieve the drag coefficient up to ~40 m s^{-1}, which leveled off above 28 m s^{-1} to a value near $3.5 \times 10^{-3}$ (dashed line in Figure 4). A similar approach was used by Jarosz et al. (2007) to deduce the drag coefficient from acoustic Doppler current profilers moored in the path of Hurricane Ivan (2006). A momentum budget using this dataset indicated a quadratic relationship with wind speed, with a peak value near $2.5 \times 10^{-3}$ at ~33 m s^{-1} that then decreased to $1.5 \times 10^{-3}$ at 45 m s^{-1}.

The uncertainty in the magnitude of the drag and enthalpy exchange coefficients in the TCBL was one of the factors leading to the deployment of the NOAA P-3 aircraft as part of the CBLAST field campaign (Black et al. 2007). Due to the safety hazards mentioned previously, the aircraft were only flown in the clear air boundary layer between rainbands, but fortunately favorable conditions for turbulence observations were achieved in two major hurricanes. French et al. (2007) reported the measurements of momentum flux from 48 flux calculation legs flown within 400 m of the surface in Hurricanes Isabel and Fabian (2003). These results provided the first open-ocean eddy correlation measurements in the TCBL at hurricane-force wind speeds. Estimates of the drag coefficient versus wind speed from this study (Figure 6) indicated no discernable dependence on speed in the range measured. Although the French et al. results slightly differ from those reported by Powell et al. (2003) and Donelan et al. (2004), general agreement exists that the extrapolated Large and Pond (1981) formula results in too high drag coefficients. Latent heat (Drennan et al. 2007) and enthalpy (Zhang et al. 2008) fluxes derived from eddy correlation measurements during CBLAST are consistent with a lack of dependence of the drag coefficient on wind speed as suggested in other studies. Recent laboratory research also indicates that the enthalpy exchange coefficient is nearly independent of wind speeds between 13 and 40 m s^{-1} (Haus et al. 2010, Jeong et al. 2010). Enthalpy exchange coefficients as a function of wind speed from the HEXOS, CBLAST, and laboratory experiments taken from Haus et al. (2010) indicate some scatter but no significant trend with increasing wind speed above ~10 m s^{-1} (Figure 7).

In summary, most recent research has indicated a steady or slightly decreasing drag coefficient with increasing wind speed beyond 30 m s^{-1}, and also near-constant enthalpy exchange coefficient in hurricane-force winds. The limited estimates of the drag

coefficient above 50 m s$^{-1}$ are inconclusive as to the magnitude, with earlier budget studies suggesting a substantially higher drag than the flux-profile method of Powell et al. (2003) and Vickery et al. (2009). Although no known eddy correlation measurements exist at these wind speeds, the laboratory tank momentum budget in Donelan et al. (2004) is in closer agreement with the studies of Powell et al. and Vickery et al. The magnitude of the enthalpy exchange at major hurricane wind speeds is even more uncertain. While there currently is no evidence to suggest that the wind speed independence should not continue above 35 m s$^{-1}$, photographs of the sea surface in these conditions depict a different character to the sea state than in minimal hurricane winds (Black et al. 1986). The sea state at Beaufort category 19 (>50 m s$^{-1}$) shown in Figure 8b is described as "low clouds, spray, and foam merge into large, white areas frequently referred to as 'white sheets' by reconnaissance crews" that cover the entire surface at these wind speeds. White water only covers about 30–40% of the photograph at ~30 m s$^{-1}$ (Figure 8a), with narrow, parallel streaks being the defining characteristic. It must be noted that parameterizing the complexity of the air-sea interaction at these wind speeds with 10 m bulk exchange coefficient may be an over-simplification, but given the established theoretical and numerical reliance on these quantities it is still believed to be a useful endeavor.
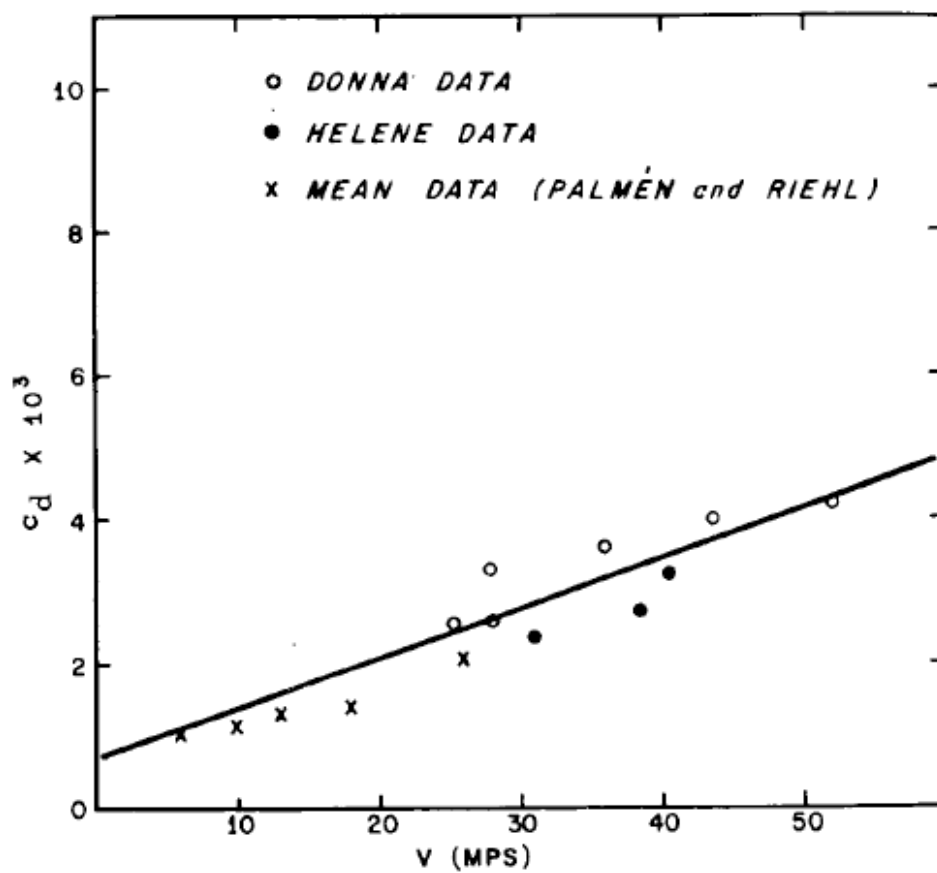
Figure 2.    Drag coefficient $C_D$ as a function of wind speed over water. From Miller (1964).

DRAG COEFFICIENTS FOR HURRICANE INEZ VS. A BACKGROUND
OF OTHER HURRICANE AND LOWER SPEED DETERMINATIONS
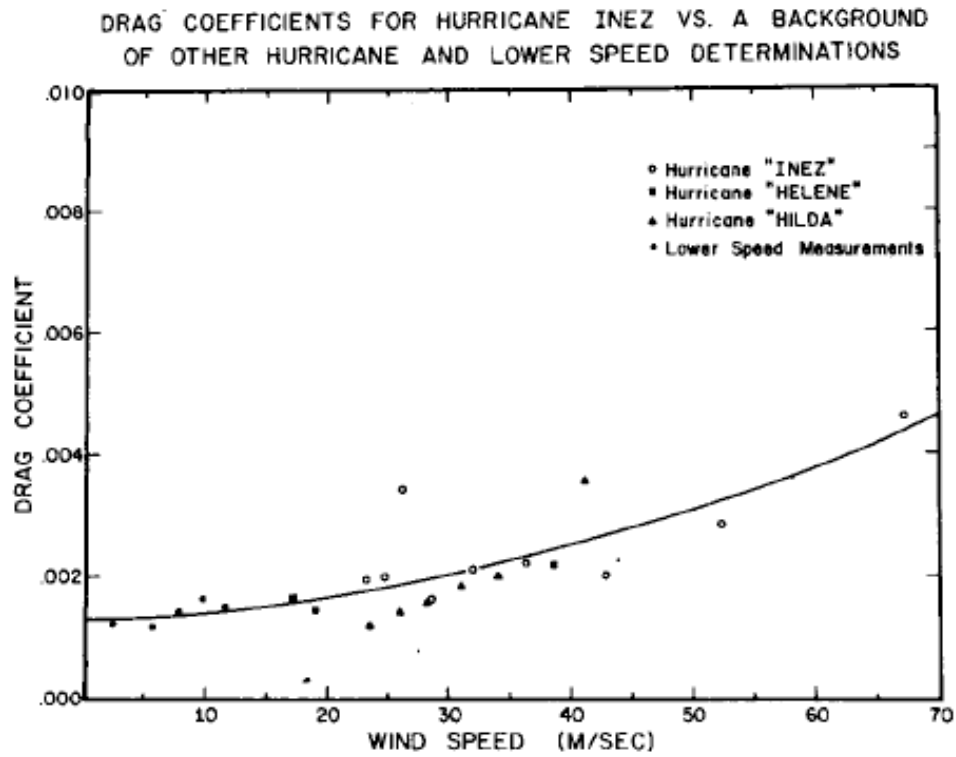
Figure 3.    Drag coefficients for Hurricane Inez (1966) from Hawkins and Imbembo (1976) plotted with values for Hurricanes Hilda and Helene and some lower speed determinations.

17
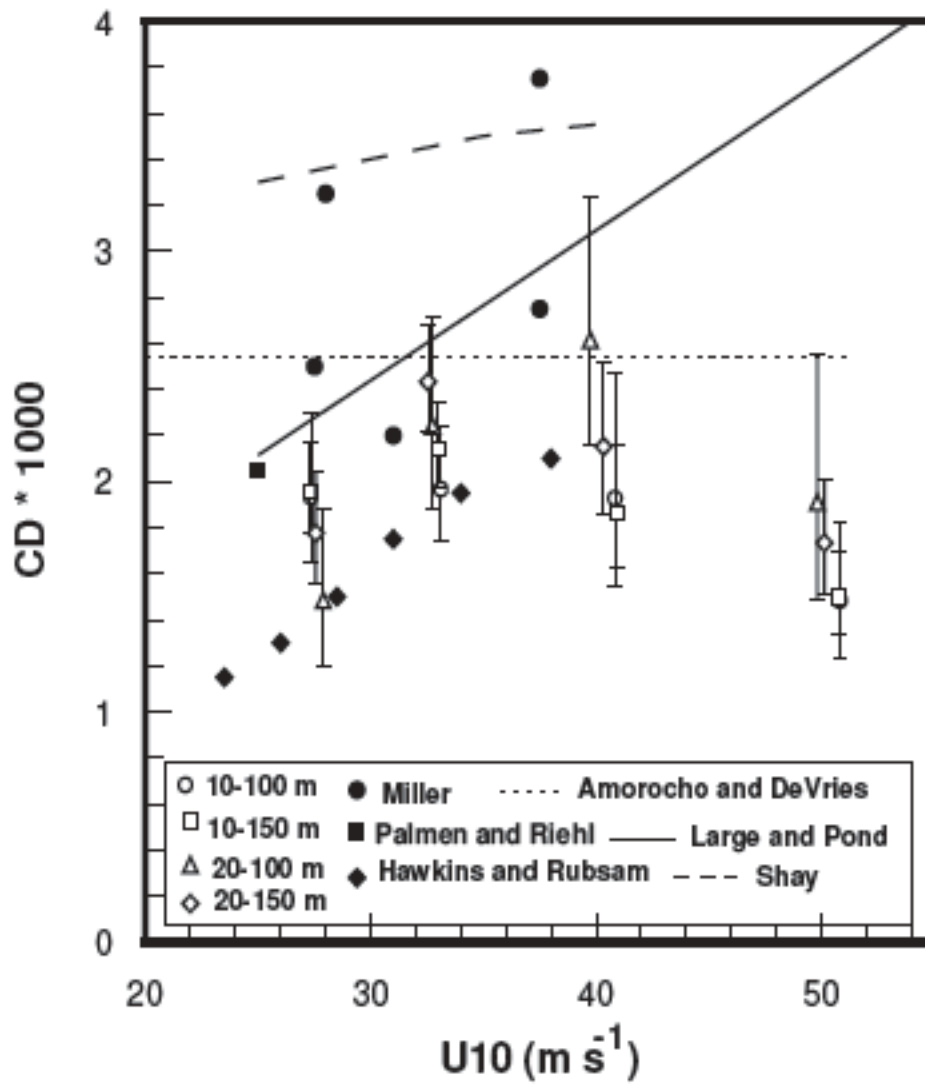
Figure 4.  Drag coefficient as a function of 10 m wind speed from dropsonde flux-profile relationship (open symbols) from Powell et al. (2003) and previous studies (closed symbols, lines).
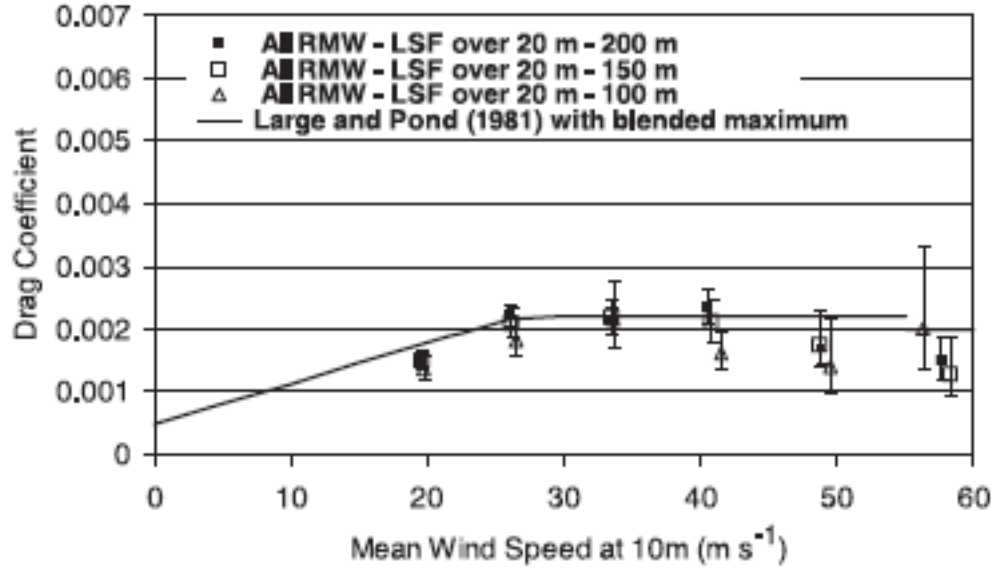
Figure 5.    Variation of the drag coefficient with mean wind speed at 10 m altitude near the radius of maximum wind (RMW). From Vickery et al. (2009).
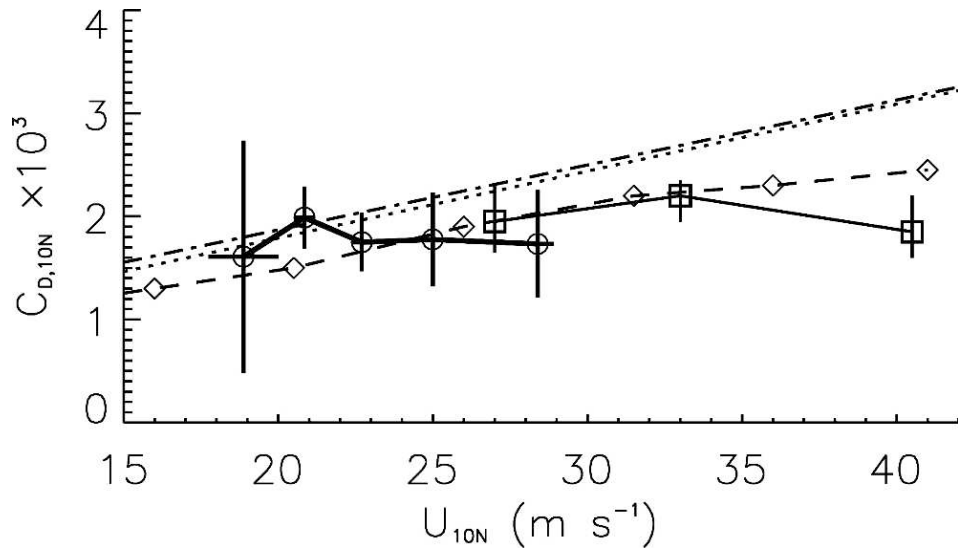


Figure 6.    Estimated drag coefficient as a function of $U_{10}$ for the 48 flux runs from French et al. (2007) showing the binned values (circles) and the 95% confidence interval from this study and extrapolation of results from Large and Pond (1981) and Smith (1980), dotted and dashed–dotted, respectively. Also shown are results from Donelan et al. (2004; diamonds) and Powell et al. (2003; squares) to 42 m s$^{-1}$.
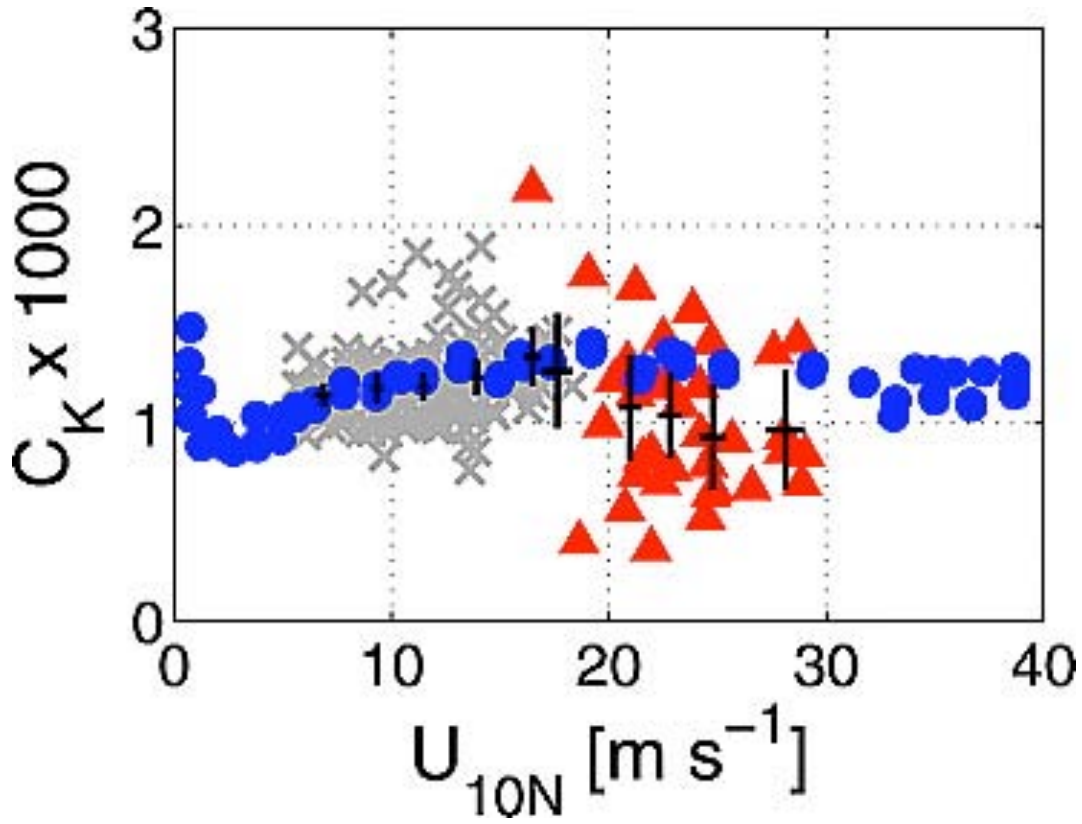
Figure 7.    Wind speed dependence of $C_K$ from Haus et al. (2010). ASIST laboratory results (•) and CBLAST (▲) measurements are shown with HEXOS results (x). After binning observations by wind speed, the mean and 95% confidence intervals as determined from a t-distribution of the combined HEXOS and CBLAST field data are shown in black.
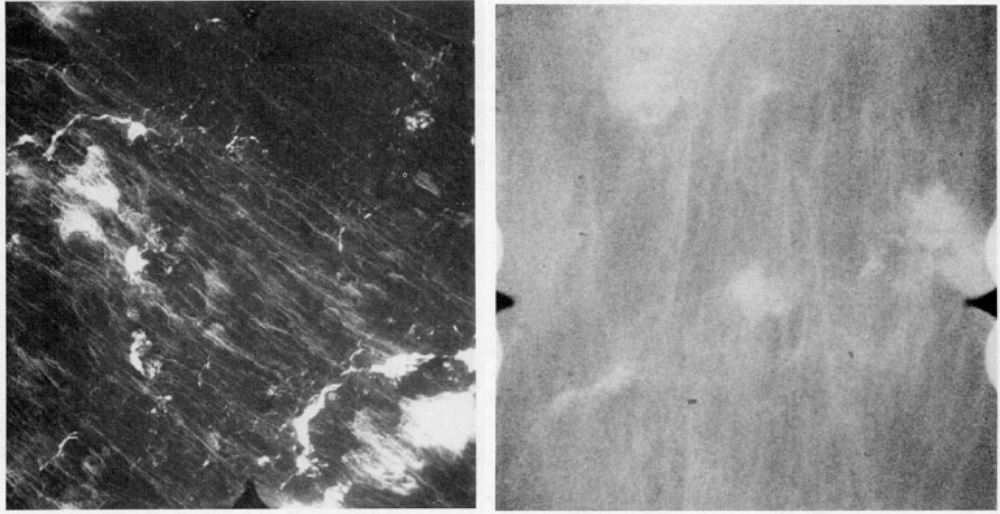
Figure 8.    Typical appearance of the sea surface in hurricane conditions of Beaufort category (a) 11 and (b) 19. The photographs were taken in (a) Hurricane Eloise at an altitude of 312 m at 2246 UTC 22 September 1975. The aircraft was in the right-front quadrant of the storm about 140 km from the center. The flight-level wind was 32.8 m s$^{-1}$ and the mean and sustained 20 m winds were 27 and 30 m s$^{-1}$, respectively. (b) Hurricane David at an altitude of 454 m at 1104 UTC 30 August 1979. The aircraft was in the right-rear quadrant about 45 km from David's center. The flight-level wind was 63.0 m s$^{-1}$, and the mean and sustained winds were 50 and 57 m s$^{-1}$, respectively. Mean and sustained winds are ten and one-minute averages, respectively. From Black et al. (1986).

THIS PAGE INTENTIONALLY LEFT BLANK

# III. BUDGET METHODOLOGY

## A. CONSERVATION OF ANGULAR MOMENTUM

To determine the bulk momentum exchange coefficient, the flux form of the azimuthally-averaged tangential momentum equation in cylindrical coordinates is:

$$\frac{\partial(\rho v)}{\partial t} + \frac{\partial(\rho ruv)}{r\partial r} + \frac{\partial(\rho wv)}{\partial z} + \frac{\rho uv}{r} + \rho fu = F_\theta \tag{3.1}$$

where $u$ is the radial wind, $v$ the tangential wind, $w$ the vertical wind, $\rho$ the density, $f$ the Coriolis parameter, and $F_\theta$ molecular friction/diffusion. Multiplying Equation (3.1) by the radius $r$, and assuming that $F_\theta$ is small above the viscous sublayer yields:

$$\frac{\partial}{\partial t}(\rho rv) + \left[\frac{\partial}{\partial r}(\rho urv) + \rho uv\right] + \frac{\partial}{\partial z}(\rho wrv) + \{\rho ruf\} = 0 \tag{3.2}$$

By the chain rule, the term in brackets reduces to:

$$\frac{\partial(\rho u(rv))}{\partial r} + \rho uv = \frac{\partial(r\rho u(rv))}{r\partial r} \tag{3.3}$$

Considering the final term in braces, the axisymmetric mass continuity equation is:

$$\frac{\partial \rho}{\partial t} + \frac{\partial(\rho ru)}{r\partial r} + \frac{\partial(\rho w)}{\partial z} = 0 \tag{3.4}$$

Assuming an $f$-plane approximation, the Coriolis parameter is a constant and therefore multiplying the continuity equation by $r^2 f/2$ yields:

$$\frac{r^2\partial(\rho f)}{2\partial t} + \frac{r\partial(\rho ruf)}{2\partial r} + \frac{r^2\partial(\rho wf)}{2\partial z} = 0 \tag{3.5}$$

By the chain rule, the second term can be expressed as:

$$\frac{r\partial(\rho ruf)}{2\partial r} = \frac{\partial(\rho ruf(r^2))}{2r\partial r} - \rho ruf \tag{3.6}$$

23

Therefore:

$$\rho ruf = \frac{\partial(\rho fr^2)}{2\partial t} + \frac{\partial(\rho ru(fr^2))}{2r\partial r} + \frac{\partial(\rho wfr^2)}{2\partial z} \qquad (3.7)$$

Substituting (3.3) and (3.7) into (3.2) yields:

$$\frac{\partial}{\partial t}\left[\rho\left(rv + fr^2/2\right)\right] + \frac{\partial}{r\partial r}\left[\rho ru\left(rv + fr^2/2\right)\right] + \frac{\partial}{\partial z}\left[\rho w\left(rv + fr^2/2\right)\right] =$$
$$\frac{\partial(\rho M)}{\partial t} + \frac{\partial(\rho ruM)}{r\partial r} + \frac{\partial(\rho wM)}{\partial z} = 0 \qquad (3.8)$$

where the absolute angular momentum is defined as $M \equiv r\overline{v} + \frac{1}{2}fr^2$

Each variable is then separated into a mean and perturbation quantity, such that $v = \overline{v} + v'$, where the mean is both an azimuthal and temporal average. Reynolds averaging and making the Boussinesq approximation (e.g., neglecting $\rho'$) yields:

$$\frac{\partial(\rho M)}{\partial t} + \frac{\partial(\rho ruM)}{r\partial r} + \frac{\partial(\rho wM)}{\partial z} + \frac{\partial(r\overline{\rho u'M'})}{r\partial r} + \frac{\partial(\overline{\rho w'M'})}{\partial z} = 0 \qquad (3.9)$$

The Reynolds stresses are then defined as $\tau_{r\theta} \equiv -\overline{\rho u'v'}$ and $\tau_{z\theta} \equiv -\overline{\rho w'v'}$, where the subscripts represent the wind directions of the covariances ($r$ is the radial direction, $\theta$ is the tangential direction, and $z$ is the vertical direction). Expanding the last two terms

$$\frac{\partial(r\overline{\rho u'M'})}{r\partial r} = \frac{\partial(r^2\overline{\rho u'v'})}{r\partial r} = -\frac{\partial(r^2\tau_{r\theta})}{r\partial r}$$
$$\frac{\partial(\overline{\rho w'M'})}{\partial z} = \frac{\partial(r\overline{\rho w'v'})}{\partial z} = -\frac{r\partial\tau_{z\theta}}{\partial z} \qquad (3.10)$$

yields the axisymmetric angular momentum equation in flux form:

$$\frac{\partial(\rho M)}{\partial t} + \frac{\partial(\rho ruM)}{r\partial r} + \frac{\partial(\rho wM)}{\partial z} - \frac{\partial(r^2\tau_{r\theta})}{r\partial r} - \frac{r\partial\tau_{z\theta}}{\partial z} = 0 \qquad (3.11)$$

Integrating over a control volume from $z_1$ to $z_2$ and $r_1$ to $r_2$ yields the integrated flux form of the conservation of angular momentum in axisymmetric cylindrical coordinates:

$$\int_{z_1}^{z_2}\int_{r_1}^{r_2}\frac{\partial(\rho M)}{\partial t}rdrdz$$

$$+\int_{z_1}^{z_2}\int_{r_1}^{r_2}\left[\frac{\partial(\rho ruM-r^2\tau_{r\theta})}{\partial r}dr\right]dz+\int_{r_1}^{r_2}\int_{z_1}^{z_2}\left[\frac{\partial(\rho wM-r\tau_{z\theta})}{\partial z}dz\right]rdr=$$

$$\int_{z_1}^{z_2}\int_{r_1}^{r_2}\frac{\partial(\rho M)}{\partial t}2\pi rdrdz$$

$$+\int_{z_1}^{z_2}2\pi r\left[\rho uM-r\tau_{r\theta}\right]\Big|_{r_2}dz-\int_{z_1}^{z_2}2\pi r\left[\rho uM-r\tau_{r\theta}\right]\Big|_{r_1}dz$$

$$+\int_{r_1}^{r_2}\left[\rho wM-r\tau_{z\theta}\right]\Big|_{z_2}2\pi rdr-\int_{r_1}^{r_2}\left[\rho wM-r\tau_{z\theta}\right]\Big|_{z_1}2\pi rdr=0 \tag{3.12}$$

Rearranging (3.12) and dividing by $2\pi$, the radially-integrated turbulent momentum flux at $z_1$ is then:

$$\int_{r_1}^{r_2}\left[\tau_{z\theta}\right]\Big|_{z_1}r^2dr=$$

$$-r_2\int_{z_1}^{z_2}\left[\rho uM-r\tau_{r\theta}\right]\Big|_{r_2}dz+r_1\int_{z_1}^{z_2}\left[\rho uM-r\tau_{r\theta}\right]\Big|_{r_1}dz$$

$$-\int_{r_1}^{r_2}\left[\rho wM-r\tau_{z\theta}\right]\Big|_{z_2}rdr+\int_{r_1}^{r_2}\left[\rho wM\right]\Big|_{z_1}rdr-\int_{z_1}^{z_2}\int_{r_1}^{r_2}\frac{\partial(\rho M)}{\partial t}rdrdz \tag{3.13}$$

From (3.13), the integrated surface stress for an arbitrary control volume may be calculated. A schematic of a hypothetical control volume is shown in Figure 9, which illustrates the approximate location of $z_1$, $z_2$, $r_1$, and $r_2$ for an idealized hurricane flow. Note that $z_1$ does not necessarily have to be at 10 m altitude, but could be anywhere in the surface layer assuming the fluxes are nearly constant in that layer.

Assuming the vertical stress at $z_1$ can be represented by a bulk formula, $\tau_{z\theta}\equiv-\overline{\rho w'v'}=C_D\rho|\vec{u}_h|v$, and neglecting the radial variation of $C_D$ over the control volume yields the drag coefficient:

$$C_D = \left( -r_2 \int_{z_1}^{z_2} \left[ \rho u M - r\tau_{r\theta} \right] \Big|_{r_2} dz + r_1 \int_{z_1}^{z_2} \left[ \rho u M - r\tau_{r\theta} \right] \Big|_{r_1} dz \right.$$
$$\left. - \int_{r_1}^{r_2} \left[ \rho w M - r\tau_{z\theta} \right] \Big|_{z_2} r dr + \int_{r_1}^{r_2} \left[ \rho w M \right] \Big|_{z_1} r dr - \int_{z_1}^{z_2} \int_{r_1}^{r_2} \frac{\partial(\rho M)}{\partial t} r dr dz \right) /$$
$$\int_{r_1}^{r_2} \left[ \rho \,|\,\vec{u}_h \,|\, v \right] \Big|_{z_1} r^2 dr \tag{3.14}$$

Since the tendency and additional flux terms cannot be calculated using the current dataset, the working form for use with these observations is

$$C_D = \left( -r_2 \int_{z_1}^{z_2} \left[ \rho u M \right] \Big|_{r_2} dz + r_1 \int_{z_1}^{z_2} \left[ \rho u M \right] \Big|_{r_1} dz \right.$$
$$\left. - \int_{r_1}^{r_2} \left[ \rho w M \right] \Big|_{z_2} r dr + \int_{r_1}^{r_2} \left[ \rho w M \right] \Big|_{z_1} r dr \right) / \left( \int_{r_1}^{r_2} \left[ \rho \,|\,\vec{u}_h \,|\, v \right] \Big|_{z_1} r^2 dr \right) + \mathbf{R} \tag{3.15}$$

where the unresolved residual is

$$\mathbf{R} = \left( r_2 \int_{z_1}^{z_2} \left[ r\tau_{r\theta} \right] \Big|_{r_2} dz - r_1 \int_{z_1}^{z_2} \left[ r\tau_{r\theta} \right] \Big|_{r_1} dz + \int_{r_1}^{r_2} \left[ r\tau_{z\theta} \right] \Big|_{z_2} r dr - \int_{z_1}^{z_2} \int_{r_1}^{r_2} \frac{\partial(\rho M)}{\partial t} r dr dz \right) /$$
$$\int_{r_1}^{r_2} \left[ \rho \,|\,\vec{u}_h \,|\, v \right] \Big|_{z_1} r^2 dr \tag{3.16}$$

Alternatively, one can obtain the average surface stress by dividing (3.13) by the integrated square of the radius $\int_{r_1}^{r_2} r^2 dr$, or divide by the mass-weighted term $-\int_{r_1}^{r_2} \rho r^2 dr$ to obtain the average friction velocity $u^*$ in the control volume. The residual terms were also unresolved in the previous studies utilizing a budget methodology. An accurate determination of the surface stress, friction velocity, or drag coefficient from this formulation requires minimal errors in the specification of the axisymmetric mass and wind fields, strict adherence to axisymmetric mass continuity, and a small magnitude of the unresolved residual terms. Each of these error sources is examined in Chapter III.D.
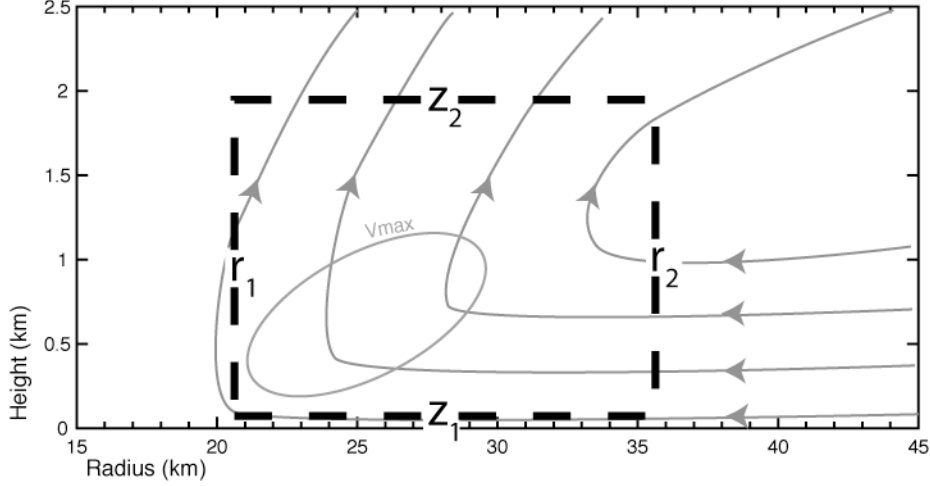
Figure 9.    Schematic illustrating hypothetical control volume (black dashed line) used for the budget methodology. A simplified secondary circulation (gray streamlines) and region of maximum wind ($v_{max}$) are shown to indicate the control volume encompasses the eyewall region.

## B.    CONSERVATION OF ENERGY

To determine the bulk moist enthalpy exchange coefficient, the first law of thermodynamics in material form with enthalpy as the state variable is:

$$\rho \frac{D(c_p T)}{Dt} = \frac{Dp}{Dt} + k\nabla^2 T + Q_R + Q_F + Q_L$$

(3.17)

where $c_p$ is the specific heat at constant pressure, $T$ is the temperature, $k$ is the thermal conductivity, $Q_R$ is the diabatic heat exchange due to radiative transfer, $Q_F$ is the heat arising from frictional dissipation of kinetic energy, and $Q_L$ is the latent heat release associated with phase changes of water, with the additional terms defined above in Chapter III.A. The latent heat release is given by:

$$Q_L = \begin{cases} 0 & \text{if } q < q_{sat} \text{ or } Dq_{sat} \leq 0 \\ \dfrac{-\rho L}{1-q_{sat}} \dfrac{Dq_{sat}}{Dt} & \text{if } q \geq q_{sat} \text{ or } Dq_{sat} > 0 \end{cases}$$

(3.18)

with $L$ the latent heat of vaporization, $q$ is the water vapor mixing ratio, and $q_{sat}$ is the saturation mixing ratio. Equation (3.18) can be approximated by

27

$Q_L \approx -L\rho Dq / Dt$ since $q_{sat}$ is small compared to unity, and $Q_L = 0$ when $Dq/Dt = 0$ (Gill 1982). The heat arising from frictional dissipation is:

$$Q_F = \rho v \left( \frac{\partial u_i}{\partial x_j} \right)^2$$

(3.19)

where $v$ is the kinematic viscosity, and the indices $i$ and $j$ represent summation over the three spatial dimensions. Equation (3.17) then becomes:

$$\rho c_p \frac{DT}{Dt} + \rho L \frac{Dq}{Dt} = \frac{Dp}{Dt} + \rho v \left( \frac{\partial u_i}{\partial x_j} \right)^2 + k\nabla^2 T + Q_R$$

(3.20)

where the mass continuity equation has been used to put the first two terms into flux form. This equation describes the internal (sensible and latent heat) energy of an air parcel. To derive the total energy equation, expressions for mechanical (kinetic and potential) energy are also needed for the parcel. Starting with the momentum equation in vector form:

$$\rho \left( \frac{D\vec{u}}{Dt} + 2\vec{\Omega} \times \vec{u} \right) = -\nabla p - \rho \nabla \vec{\Phi} + F_u$$

(3.21)

where $\vec{u}$ is the three-dimensional wind vector, $2\vec{\Omega} \times \vec{u}$ is the Coriolis acceleration, $g$ is gravity, and $F_u$ is molecular friction/dissipation. Dotting $\vec{u}$ into (3.21) yields the kinetic energy equation, where $F_u$ has been separated into its diffusive and dissipative parts:

$$\frac{1}{2}\rho \frac{D\left(u^2 + v^2 + w^2\right)}{Dt} = -\vec{u}\cdot\nabla p - \vec{u}\cdot\rho\nabla\vec{\Phi} + \rho\mu\nabla\left(\frac{1}{2}\vec{u}^2\right) - \rho v\left(\frac{\partial u_i}{\partial x_j}\right)^2$$

(3.22)

with $\mu$ denoting the molecular viscosity. The potential energy is given by the geopotential:

$$\rho \frac{D\vec{\Phi}}{Dt} = \rho\vec{u}\cdot\nabla\vec{\Phi} = wg\rho$$

(3.23)

28

Since $\vec{\Phi}$ depends only on $z$, the partial derivative with respect to time is zero. Adding (3.23) to (3.22) yields the mechanical energy equation:

$$\frac{1}{2}\rho\frac{D\left(u^2+v^2+w^2\right)}{Dt}+\rho\frac{D\vec{\Phi}}{Dt}=\rho\mu\nabla\left(\frac{1}{2}\vec{u}^2\right)-\rho v\left(\frac{\partial u_i}{\partial x_j}\right)^2+\left(\frac{\partial p}{\partial t}-\frac{Dp}{Dt}\right)$$

(3.24)

where the pressure advection has been replaced using the definition of the material derivative, $Dp/Dt = \partial p/\partial t + \vec{u}\cdot\nabla p$. Adding the internal energy equation (3.20) and the mechanical energy equation (3.24) yields the total energy equation in material form:

$$c_p\rho\frac{DT}{Dt}+L\rho\frac{Dq}{Dt}+\frac{1}{2}\rho\frac{D(u^2+v^2+w^2)}{Dt}+\rho\frac{D(\Phi)}{Dt}=$$
$$\rho\frac{D}{Dt}\left(c_pT+Lq+\frac{1}{2}(u^2+v^2+w^2)+\Phi\right)=\rho\mu\nabla\left(\frac{1}{2}\vec{u}^2\right)+k\nabla^2T+Q_R+\frac{\partial p}{\partial t}$$

(3.25)

Note that the dissipative heating terms have cancelled since they represent a conversion between mechanical and heat energy. Here, it is assumed that the diffusive component of friction, thermal conductivity, and radiation on the right side of (3.25) are small and can be neglected in this application. The time derivative of $p$ on the right-hand side does not cancel because the thermodynamic equation was expressed in terms of the enthalpy instead of the internal energy (e.g., $c_pT = c_vT + p/\rho$). In this application, local changes in pressure are associated with acoustic waves in the atmosphere and this term is small and also neglected. With the right side set to zero, Equation (3.25) is known as Bernoulli's equation (Gill 1982). Expanding the material derivative to flux form in azimuthally-averaged cylindrical coordinates:

$$\frac{\partial\left[\rho\left(c_pT + Lq + \frac{1}{2}(u^2 + v^2 + w^2) + gz\right)\right]}{\partial t} + \frac{\partial\left[\rho ru\left(c_pT + Lq + \frac{1}{2}(u^2 + v^2 + w^2) + gz\right)\right]}{r\partial r}$$

$$+ \frac{\partial\left[\rho w\left(c_pT + Lq + \frac{1}{2}(u^2 + v^2 + w^2) + gz\right)\right]}{\partial z} = 0$$

(3.26)

Each variable is then separated into mean and perturbation quantities as before, where the mean is both an azimuthal and temporal average, and are Reynolds-averaged using the Boussinesq approximation. For simplification, several terms may be grouped and defined:

$$E = c_pT + Lq + \frac{1}{2}(u^2 + v^2 + w^2) + gz$$

(3.27a)

$$e = \frac{1}{2}\rho(\overline{u'^2} + \overline{v'^2} + \overline{w'^2})$$

(3.27b)

$$F_{rT} = \rho c_p \overline{u'T'}$$

(3.27c)

$$F_{zT} = \rho c_p \overline{w'T'}$$

(3.27d)

$$F_{rq} = \rho L \overline{u'q'}$$

(3.27e)

$$F_{zq} = \rho L \overline{w'q'}$$

(3.27f)

where $E$ is the total energy of the mean flow, $e$ is the turbulent kinetic energy, and the $F$ terms are radial and vertical fluxes of temperature and moisture in which the subscripts indicate the covariances. The Reynolds averaging yields:

$$\frac{\partial(\rho E)}{\partial t} + \frac{\partial(\rho r u E)}{r\partial r} + \frac{\partial(\rho w E)}{\partial z} + \frac{\partial(r F_{rT})}{r\partial r} + \frac{\partial F_{zT}}{\partial z} + \frac{\partial(r F_{rq})}{r\partial r} + \frac{\partial F_{zq}}{\partial z} =$$

$$\frac{\partial p}{\partial t} - \frac{\partial e}{\partial t} - \frac{\partial(rue)}{r\partial r} - \frac{\partial(we)}{\partial z} - \frac{\partial(r\overline{u'e})}{r\partial r} - \frac{\partial(\overline{w'e})}{\partial z}$$

$$+ \frac{\partial(rw\tau_{rz})}{r\partial r} + \frac{\partial(u\tau_{rz})}{\partial z} + \frac{\partial(rv\tau_{r\theta})}{r\partial r} + \frac{\partial(v\tau_{z\theta})}{\partial z}$$

$$(3.28)$$

Note that terms involving $\tau_{ij}\partial u_i / \partial x_j$ cancel due to conversion of mean kinetic energy to turbulent kinetic energy (e.g., see Lindzen 1990, 90–92), but flux gradients involving $\partial(\tau_{ij}u_i)/\partial x_j$ remain. For lack of an established term, this is coined the "shear flux," as it represents a loss of kinetic energy through the interaction of turbulent momentum fluxes and shearing flow. Grouping terms and integrating over the control volume:

$$\int_{z_1}^{z_2} 2\pi r_2 \left[\rho u E + F_{rT} + F_{rq}\right]\Big|_{r_2} dz - \int_{z_1}^{z_2} 2\pi r_1 \left[\rho u E + F_{rT} + F_{rq}\right]\Big|_{r_1} dz$$

$$+ \int_{r_1}^{r_2} \left[\rho w E + F_{zT} + F_{zq}\right]\Big|_{z_2} 2\pi r dr - \int_{r_1}^{r_2} \left[\rho w E + F_{zT} + F_{zq}\right]\Big|_{z_1} 2\pi r dr =$$

$$\int_{z_1}^{z_2}\int_{r_1}^{r_2} \left[\frac{\partial(p - \rho E - e)}{\partial t}\right] 2\pi r dr dz + \int_{z_1}^{z_2} 2\pi r_2 \left[-ue - \overline{u'e} + w\tau_{rz} + v\tau_{r\theta}\right]\Big|_{r_2} dz$$

$$- \int_{z_1}^{z_2} 2\pi r_1 \left[-ue - \overline{u'e} + w\tau_{rz} + v\tau_{r\theta}\right]\Big|_{r_1} dz + \int_{r_1}^{r_2}\left[-we - \overline{w'e} + u\tau_{rz} + v\tau_{z\theta}\right]\Big|_{z_2} 2\pi r dr$$

$$- \int_{r_1}^{r_2}\left[-we - \overline{w'e} + u\tau_{rz} + v\tau_{z\theta}\right]\Big|_{z_1} 2\pi r dr$$

$$(3.29)$$

Rearranging (3.29) and dividing by $2\pi$, the radially-integrated enthalpy flux at $z_1$ is:

$$\int_{r_1}^{r_2} \left[ F_{zk} \right]\Big|_{z_1} r dr = \int_{r_1}^{r_2} \left[ F_{zT} + F_{zq} \right]\Big|_{z_1} r dr =$$

$$\int_{z_1}^{z_2} r_2 \left[ \rho u E + F_{rk} + ue + \overline{u'e} - w\tau_{rz} - v\tau_{r\theta} \right]\Big|_{r_2} dz$$

$$-\int_{z_1}^{z_2} r_1 \left[ \rho u E + F_{rk} + ue + \overline{u'e} - w\tau_{rz} - v\tau_{r\theta} \right]\Big|_{r_1} dz$$

$$+\int_{r_1}^{r_2} \left[ \rho w E + F_{zk} + we + \overline{w'e} - u\tau_{rz} - v\tau_{z\theta} \right]\Big|_{z_2} r dr$$

$$-\int_{r_1}^{r_2} \left[ \rho w E + we + \overline{w'e} - u\tau_{rz} - v\tau_{z\theta} \right]\Big|_{z_1} r dr$$

$$+\int_{z_1}^{z_2} \int_{r_1}^{r_2} \left[ \frac{\partial(\rho E + e)}{\partial t} \right] r dr dz$$

(3.30)

It is then assumed that the vertical moist enthalpy flux at $z_1$ can be represented by a bulk formula:

$$F_{zk} = F_{zT} + F_{zq} \equiv \bar{\rho} c_p \overline{w'T'} + \bar{\rho} L \overline{w'q'} = C_K \bar{\rho} |\vec{u}_h| (k^* - k)$$

(3.31)

where $k^*$ is the saturation moist enthalpy at the sea surface ($k^* = c_p T_{SST} + Lq^*$), and $q^*$ is the saturation mixing ratio at the surface. Neglecting the radial variation of $C_K$ over the control volume yields the bulk enthalpy exchange coefficient:

$$C_K = \left( \int_{z_1}^{z_2} r_2 \left[ \rho u E + F_{rk} + ue + \overline{u'e} - w\tau_{rz} - v\tau_{r\theta} \right]\Big|_{r_2} dz \right.$$

$$-\int_{z_1}^{z_2} r_1 \left[ \rho u E + F_{rk} + ue + \overline{u'e} - w\tau_{rz} - v\tau_{r\theta} \right]\Big|_{r_1} dz$$

$$+\int_{r_1}^{r_2} \left[ \rho w E + F_{zk} + we + \overline{w'e} - u\tau_{rz} - v\tau_{z\theta} \right]\Big|_{z_2} r dr$$

$$-\int_{r_1}^{r_2} \left[ \rho w E + we + \overline{w'e} - u\tau_{rz} - v\tau_{z\theta} \right]\Big|_{z_1} r dr$$

$$\left. +\int_{z_1}^{z_2} \int_{r_1}^{r_2} \left[ \frac{\partial(\rho E + e)}{\partial t} \right] r dr dz \right) / \int_{r_1}^{r_2} \left[ \rho |\vec{u}_h| (k^* - k) \right]\Big|_{z_1} r dr$$

(3.32)

Similar assumptions as in the momentum equation are made to group unresolved terms into a residual:

$$C_K = \left( \int_{z_1}^{z_2} r_2 \left[ \rho u E \right]\Big|_{r_2} dz - \int_{z_1}^{z_2} r_1 \left[ \rho u E \right]\Big|_{r_1} dz + \int_{r_1}^{r_2} \left[ \rho w E \right]\Big|_{z_2} r dr - \int_{r_1}^{r_2} \left[ \rho w E \right]\Big|_{z_1} r dr + F_{SHEAR} \right)$$

$$\int_{r_1}^{r_2} \left[ \rho \, | \vec{u}_h | (k^* - k) \right]\Big|_{z_1} r dr + \mathbf{R}$$

(3.33)

where the transport of energy by the interaction of turbulence and the mean wind through the lower boundary $F_{SHEAR} = \int_{r_1}^{r_2} \left[ u \tau_{rz} + v \tau_{z\theta} \right]\Big|_{z_1} r dr$ is written separately since it may be resolved indirectly via the results from the drag coefficient calculation. Alternatively, one can obtain the average enthalpy flux by dividing (3.30) by the integrated radius. The unresolved residual is

$$\mathbf{R} = \left( \int_{z_1}^{z_2} r_2 \left[ F_{rk} + ue + \overline{u'e} - w\tau_{rz} - v\tau_{r\theta} \right]\Big|_{r_2} dz \right.$$
$$- \int_{z_1}^{z_2} r_1 \left[ F_{rk} + ue + \overline{u'e} - w\tau_{rz} - v\tau_{r\theta} \right]\Big|_{r_1} dz$$
$$+ \int_{r_1}^{r_2} \left[ F_{zk} + we + \overline{w'e} - u\tau_{rz} - v\tau_{z\theta} \right]\Big|_{z_2} r dr$$
$$\left. - \int_{r_1}^{r_2} \left[ we + \overline{w'e} \right]\Big|_{z_1} r dr + \int_{z_1}^{z_2} \int_{r_1}^{r_2} \left[ \frac{\partial (\rho E + e)}{\partial t} \right] r dr dz \right) \Big/$$
$$\int_{r_1}^{r_2} \left[ \rho \, | \vec{u}_h | (k^* - k) \right]\Big|_{z_1} r dr$$

(3.34)

As with the momentum budget, accuracy in the retrieval of the enthalpy exchange coefficient requires: (i) minimal errors in the specification of the axisymmetric thermodynamic and kinematic fields; (ii) strict adherence to mass continuity; and (iii) a small magnitude of the unresolved residual terms. The validity of these assumptions is presented in the following section, using numerically simulated tropical cyclones' budgets.

## C.    PROOF OF CONCEPT: VERIFICATION USING SIMULATED DATA

To test the accuracy of the methodology described in the previous chapter, comprehensive momentum and enthalpy budget analyses using idealized numerical simulations were undertaken. The first objective is to retrieve bulk drag and enthalpy

exchange coefficients with known magnitudes using numerically simulated observations of tropical cyclones. The second objective (to be described in Chapter II.D) is to use the simulated data sets in a budget error analysis.

Two numerical weather models were used to test the budget methodology. The first was the two-dimensional, axisymmetric hurricane model developed by Rotunno and Emanuel (1987, hereafter RE87); and the second was the three-dimensional Advanced Research Weather and Forecasting Model version 3.0.1.1 (hereafter, WRF). Since the main goal of the numerical modeling effort was to produce idealized, but still physically realistic, hurricane simulations, an effort was made to closely replicate the initial conditions and parameterizations of the two models. The initial atmospheric conditions used for both models was the thermodynamic background defined by the Jordan (1958) mean tropical Atlantic sounding that was modified to be in thermal wind balance (Smith 2006) with the initial tangential winds specified from an analytic mesoscale vortex (RE87, Equation 37). The sea-surface temperature was fixed in the RE87 model at 26.5° C, and at 28.0° C in the WRF simulation. Both simulations used warm rain microphysics, with a single category for all liquid water but variable terminal fall speed depending on the mixing ratio in RE87, and separate categories for cloud and rain water in the WRF model using the Kessler (1969) microphysics scheme. The RE87 model used Newtonian cooling, and radiation was not included in the WRF simulation. In RE87, a uniform 1 km horizontal (radial) and 250 m vertical grid spacing were used in a 1500 km by 25 km domain. All other settings are similar to those from the 4X run of Persing and Montgomery (2003), except the surface fluxes as described below. In WRF, a four-way nested domain was used with a fine mesh containing 205 x 208 gridpoints at 1 km horizontal grid spacing, which tripled with each successive mesh to a 5400 km square coarse domain with 27 km resolution. Fifty vertical levels were unevenly distributed with the highest resolution in the boundary layer using the default WRF sigma levels. The WRF model was run for a total of 8 days, and reached steady state around 150 hours into the simulation. The RE87 model simulations reached steady state from 100–150 hours and were extended to 12 days due to the lower computational requirements. A summary of the model settings is given in Table 1.

In addition to the fundamental geometrical and dynamical differences of the two models, the surface flux and sub-grid turbulence parameterizations use different approaches, which provided independent storm structures and magnitudes of the surface exchange for testing the budget methodology. In the RE87 model, sub-grid turbulence is parameterized by a local, first-order closure that relates turbulent fluxes to resolved grid-scale gradients by an eddy-viscosity assumption. Since the model is axisymmetric, all three-dimensional motions are therefore parameterized by gradients in the azimuthal mean flow. The resolved deformation flow and a prescribed mixing length determine the eddy viscosity following Smagorinsky (1963).

Surface fluxes in the RE87 model are given by bulk aerodynamic formula, such that the bulk surface exchange coefficients can be prescribed exactly. In an effort to determine whether the proposed budget methodology can distinguish effectively between different magnitudes of the drag and enthalpy exchange coefficients, five simulations with different coefficient magnitudes and different $C_K/C_D$ ratios were performed. The "high" magnitude simulations used the Deacon formula, as originally prescribed in RE87:

$$C_D = 1.1 \times 10^{-3} + 4 \times 10^{-5} (u^2 + v^2)^{1/2} \big|_{\Delta z/2}$$

with the corresponding $C_K$ given by a defined ratio of either 1.0 ("high1") or 0.7 ("high0.7") to the drag coefficient. The "mid" magnitude simulations used the same Deacon formula at surface wind speeds up to 35 m s$^{-1}$, but the exchange coefficients then were capped at higher wind speeds. Note that the surface fluxes were not capped above hurricane force, merely the wind-speed dependence of the exchange coefficients. Two "mid" simulations using $C_K/C_D$ of 1.0 ("mid1") and 0.7 ("mid0.7") were performed. A single "low" simulation also was performed in which the bulk exchange coefficients were derived from direct aircraft measurements of the turbulent fluxes reported in Black et al. (2004), Drennan et al. (2004), and Zhang et al. (2008) (see Chapter II.B for a review of these results). For the "low" simulation, $C_K$ was set to $1.1 \times 10^{-3}$ for all wind speeds, and the Deacon formula $C_D$ was capped at $1.9 \times 10^{-3}$. These five RE87 simulations give a range of coefficients for testing the sensitivity of the budget methodology.

The WRF model has several turbulence closures available. The modified Yonsei University Scheme (hereafter YSU) (Noh et al. 2003; Hong et al. 2006) was selected for this study. This scheme employs a non-local boundary layer parameterization in which a parabolic eddy viscosity profile is prescribed to match the estimated model boundary layer depth (defined in the model as the top of a well-mixed layer of virtual potential temperature). Additional vertical fluxes that account for transport by large eddies and entrainment at the top of the PBL are also included in this formulation. Above the boundary layer, the YSU scheme uses a local eddy viscosity assumption which is somewhat similar to the RE87 model except it is formulated in three dimensions. Davis et al. (2008) described modifications to the original YSU scheme for hurricane simulations in a similar manner to the "mid" RE87 runs described above, such that the drag and enthalpy exchange coefficients do not increase beyond 35 m s$^{-1}$. In Davis et al. (2008), the bulk exchange coefficients were not modified directly, but rather were adjusted through the surface roughness by setting $z_0 = 10 \exp\left(-10/u_*^{1/3}\right)$ with lower and upper limits of 1.25 x 10$^{-7}$ m and 2.85 x 10$^{-3}$ m, respectively. This modified surface flux option was selected for this study, but no modifications were made to the WRF source code. The drag and enthalpy exchange coefficients were then inferred from the output $u_*$ and sensible and latent heat fluxes at each gridpoint. The retrieved WRF fluxes were slightly different from those described in Davis et al. (2008), because examination of the v3.0.1.1 code shows a modified roughness formulation that saturates at 28 m s$^{-1}$ instead of 35 m s$^{-1}$ (the -10 in the exponent is equal to -9 in this version). Although the WRF model includes an optional one-dimensional ocean mixed layer model for these simulations, it was not included in this study.

The maximum low-level winds for the simulations are shown in Figure 10. The RE87 winds are reported at 125 m altitude, and the WRF winds are from a diagnostic 10 m value. All six simulations have instantaneous low-level wind speeds exceeding 70 m s$^{-1}$, so that all of these modeled storms are at category five intensity. After a ~4–5 day intensification period, all the simulations reach a relatively steady maximum intensity ranging from 75—120 m s$^{-1}$. The weakest storm was the "high0.7" simulation, and the strongest was the "mid1." The three-dimensional WRF simulation and the "low" RE87

simulation were the two slowest developers, with both storms peaking at 150 hours near 100 m s$^{-1}$ before a slight weakening period. The "0.7" $C_K/C_D$ ratio simulations are weaker than the corresponding "1.0" simulations for the same flux formulation, which is in accord with the predictions of E-PI theory. However, the large difference between the "mid1" and "high0.7" simulated intensity is counter-intuitive in terms of E-PI theory, which depends only on the $C_K/C_D$ ratio and not on the absolute magnitudes of the exchange coefficients. The RMW is ~5 km smaller in the "mid1" simulation than in the "high1" (not shown), which is consistent with a higher tangential wind for a similar absolute angular momentum distribution, but a more detailed comparison of the differences in the model simulations is beyond the scope of this study. While some of the simulated storms are significantly stronger than observed tropical cyclones, they are sufficiently realistic for testing the momentum and energy budget methodology outlined in Chapters II.B and II.C, with the caveat that the exact magnitudes of various terms may be over- or under-estimated compared with actual storms.

A representative sample of the simulated structures from the RE87 simulations re-analyzed by the SAMURAI software developed for this study is shown in Figure 11. The SAMURAI analysis is described in detail in Chapter IV. The analysis is shown here to facilitate a better comparison of the structure with the observed storms presented in Chapter V. A comparison of the raw model results with the SAMURAI analysis is discussed in Chapter II.D.4 below. The 6-hour averaged axisymmetric tangential wind (Fig. 11, top) at 168 hours from the "low" simulation has a maximum of ~110 m s$^{-1}$ at 1 km altitude and 20 km radius, with a well-defined secondary circulation. The top of the inflow layer has a steep downward slope inside the RMW that approximately matches the level of the maximum tangential wind, and outside the RMW the top is at a relatively high altitude of 2 km. Upward motion and outflow maxima are found just above the maximum tangential wind. The secondary circulation is aligned closely with the angular momentum and energy contours in the eyewall region, with a relative energy maximum (~351 kJ kg$^{-1}$) near the surface just radially inward of the RMW. The model vortex has a similar kinematic and thermodynamic structure as in previous RE87 simulations (Persing

37

and Montgomery 2003). Although some variations in the structure are simulated depending on the flux configuration, all runs are qualitatively similar.

To obtain the WRF axisymmetric structure, a SAMURAI analysis was performed using circulation centers derived using the method described in Chapter V.C.2. Since the simulation was on an *f*-plane with no environmental flow, the wind, pressure, and circulation centers were nearly coincident and practically stationary over the period. Hourly analyses were created using the 15-minute model output with independent estimates of the center position from alternating east-west and north-south slices analogous to the "figure-4" flight pattern used in aircraft reconnaissance. No noise or center position perturbations were added, which thus yields the "best" analysis possible for these simulated fields. The intent was to emulate the analysis procedure used with the CBLAST dataset and provide a best-case scenario for understanding errors associated with neglecting the residual budget terms discussed in Chapters III.A and III.B, as well as small errors introduced in the analysis process.

An example of the model output used in the analysis is shown in Figure 12, with the 1 km altitude fine-mesh horizontal wind vectors and speed and simulated 50 dBZ radar reflectivity contour at 144 hours. The eyewall is apparent as a nearly symmetric 15-km wide annulus of high reflectivity co-located with a region of strong winds over 80 m s$^{-1}$ and a peak wind speed exceeding 120 m s$^{-1}$ on the inner edge of the high-rain region. Some radial outflow is also evident in the wind vectors at this inner reflectivity edge. Minimal structural changes are simulated in the eyewall region over the 24-hour period (144–168 hours) used for the budget analysis.

The axisymmetric SAMURAI analysis at 144 hours for the WRF simulated structure (Figure 13) is generally similar to the RE87 structure, but is notably different in several details. For example, the wind maximum in the WRF simulation is found at lower altitudes and radially inward of the location in the RE87 "low" simulation. Furthermore, the sloping inflow reaches only 1-km height in the outer part of the domain, and is ~20 m s$^{-1}$ stronger than the RE87 inflow near the surface, and is topped by a stronger outflow region. Mostly congruent secondary circulation and angular momentum and energy contours are also found in this simulation, but the energy values are higher. It is noted

that the density is lower in the WRF simulation than in the RE87 simulation (not shown), such that mass-weighted energy is not as different as Figures 13 and 14 might suggest. However, the axisymmetric kinematic and thermodynamic structures of the RE87 and WRF simulations are clearly distinct from a budget standpoint. While this is an interesting research result, the objective of this section is to test the budget method with reasonably realistic, balanced terms, and not to establish the fidelity of the simulations to a real tropical cyclone. A systematic exploration of the differences between the axisymmetric and 3D models is therefore deferred to a later study.

Bulk exchange coefficients diagnosed from the model output for the "high1," "mid1," and "low" RE87 experiments and WRF are shown in Figure 14. The RE87 code was modified to output all of the subgrid terms, including the residual terms and surface stress, heat, and moisture fluxes. Since these surface flux terms were prescribed by the bulk aerodynamic formula, the diagnosed exchange coefficients match the analytic values very closely, as expected. For the WRF simulations, the equivalent drag and enthalpy exchange coefficients were diagnosed using the bulk aerodynamic formula and the output friction velocity and surface heat fluxes. These $C_K$ and $C_D$ values are slightly lower than the 10 m analytic values since the fluxes were calculated at the lowest sigma level (~40 m altitude). For the WRF, the drag coefficient (Fig. 14a) levels off at 28 m s$^{-1}$, with an increasing $C_K$ (Fig. 14b) near 1.9x10$^{-3}$ for wind speeds around 60 m s$^{-1}$. This flux profile corresponds reasonably well to the "mid1" flux configuration used in the RE87 experiments. All of these magnitudes are within the range of expected values for the exchange coefficients in real tropical cyclone boundary layers.

Since all of the subgrid scale terms could be recorded from the RE87 simulations, it was also possible to test the proposed retrieval method when all terms in the budget were included. This test for a representative sample from the "high1," "mid1," and "low" simulations is shown in Figure 15. The exact match of the derived and prescribed coefficients is as expected, and serves as a validation of the retrieval method when all the terms are known. These results were independent of the control volume used for the retrieval. Since the goal was to simply validate the retrieval methodology, an equivalent

test was not performed with the WRF model due to the added complexity of calculating and storing the Reynolds averaged fluxes in cylindrical coordinates.

Table 1.    Summary of numerical simulation configurations

| Model | RE87 | WRF |
|---|---|---|
| Horizontal grid spacing | 1 km radial | 1 km fine to 27 km coarse |
| Vertical grid spacing | 250 m | 50 uneven sigma levels starting at 40 m spacing |
| Microphysics | Warm rain | Kessler |
| Surface Layer | "high1," "high0.7," "mid1," "mid0.7," "low" bulk aerodynamic formulations | YSU similarity with hurricane modification (isftcflx=1) |
| PBL | 1$^{st}$ order, local closure | YSU scheme |
| Lateral Boundary conditions | Jordan sounding | Jordan sounding |
| SST (C) | 26.5 | 28.0 |
| Radiation | Newtonian cooling | None |
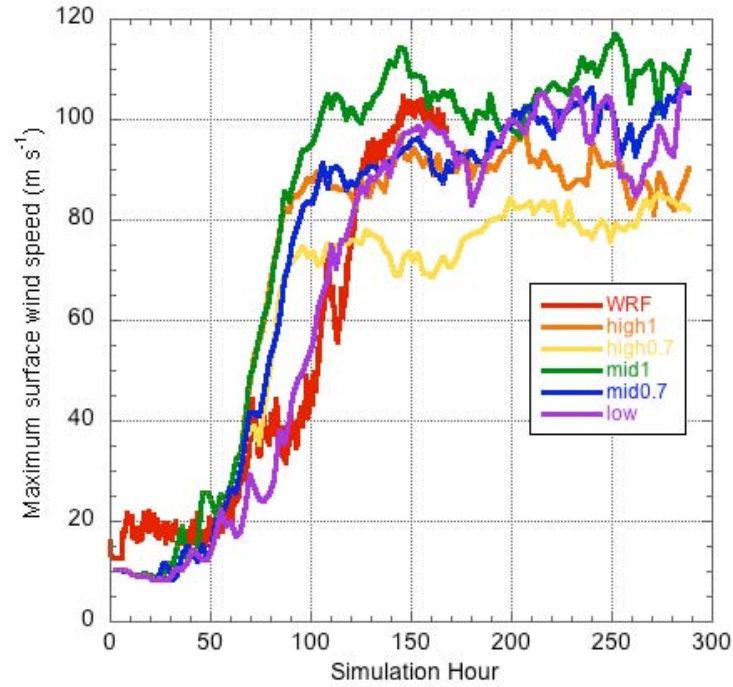
Figure 10.    Simulated maximum low-level wind for the control runs used in sensitivity testing. Low-level winds are maximum instantaneous 10 m winds diagnosed every 15 minutes from the WRF simulation, and are maximum instantaneous axisymmetric 125 m winds every six hours from the five RE87 simulations (see inset).
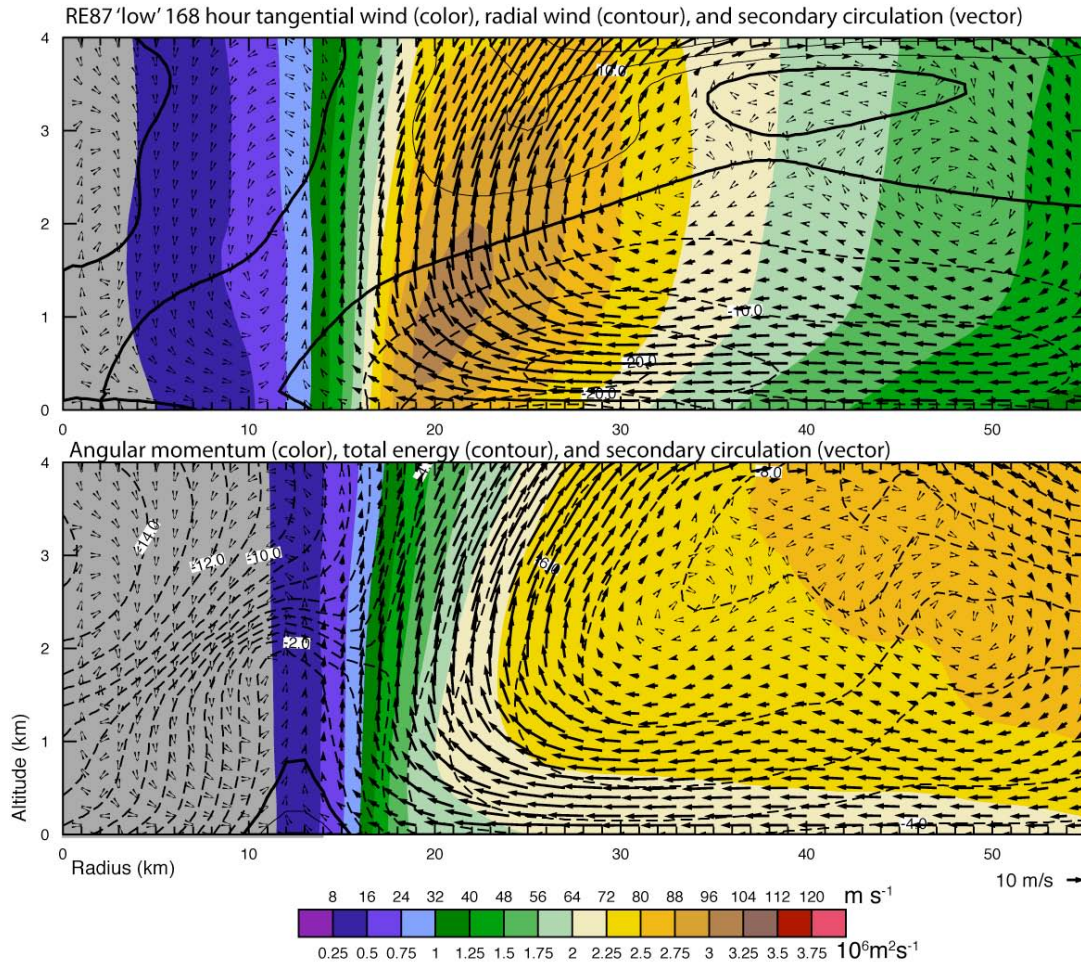
Figure 11.    RE87 "low" simulation axisymmetric structure at 144 hours. Top panel shows tangential wind (color, m s$^{-1}$), radial wind (5 m s$^{-1}$ contours), and secondary circulation. Bottom panel shows angular momentum (color, $10^6$m$^2$s$^{-1}$), total energy (350 kJ kg$^{-1}$ + 1 kJ kg$^{-1}$ contours), and secondary circulation (vector). Solid contours indicate positive values, and dashed contours indicate negative values.
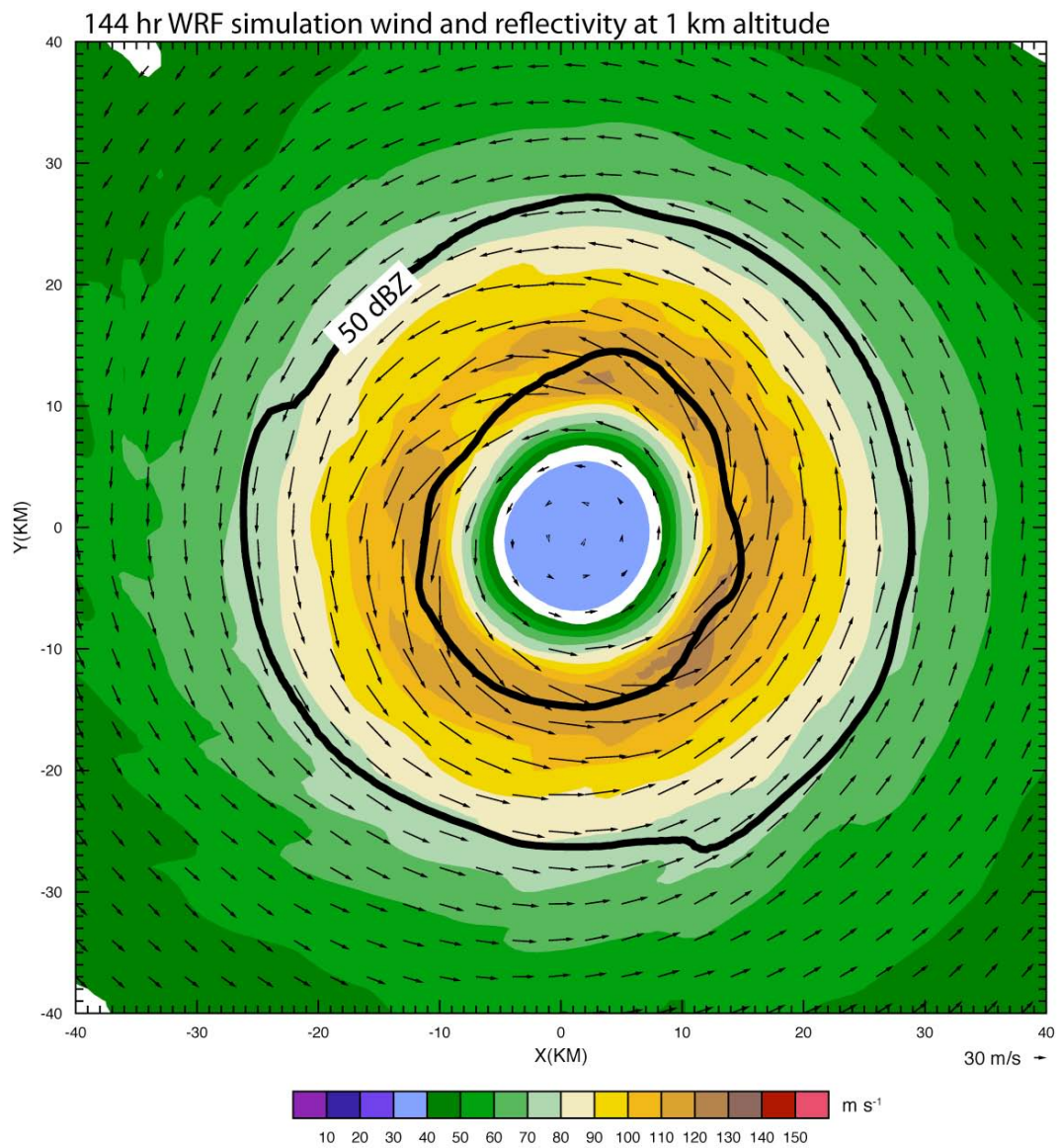
Figure 12.    Wind vectors (scale vector at bottom right) and speed (color scale, m s$^{-1}$) at 1 km altitude and simulated radar reflectivity 50 dBZ contours at 144 hours from the WRF simulation.
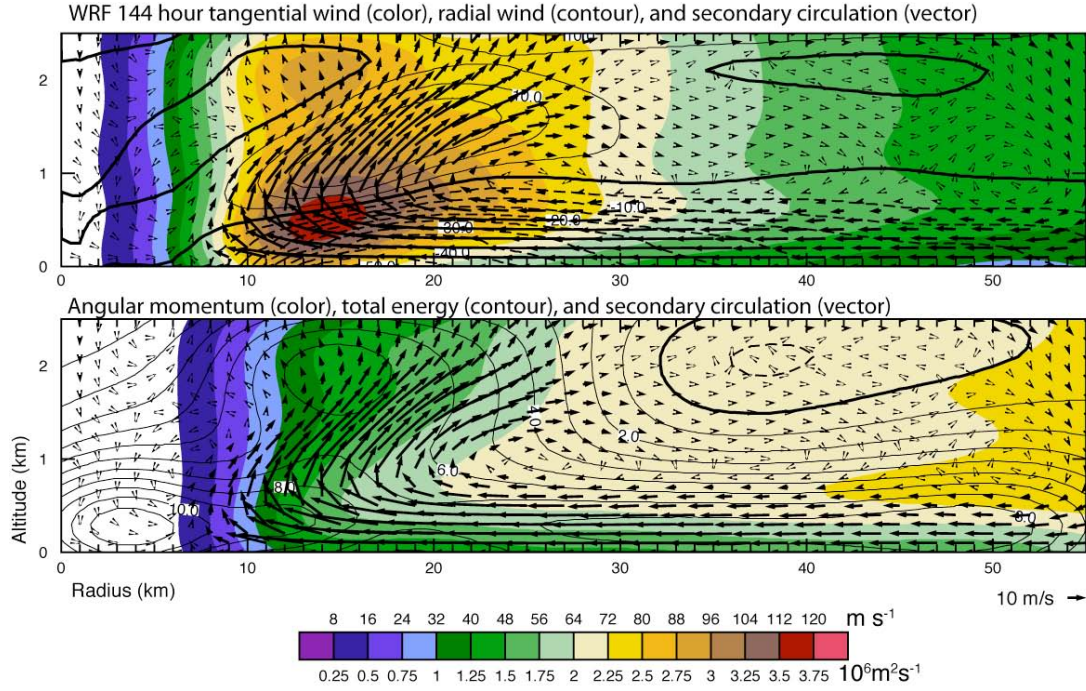
Figure 13.        WRF axisymmetric structure at 144 hours. Contours as in Figure 11.
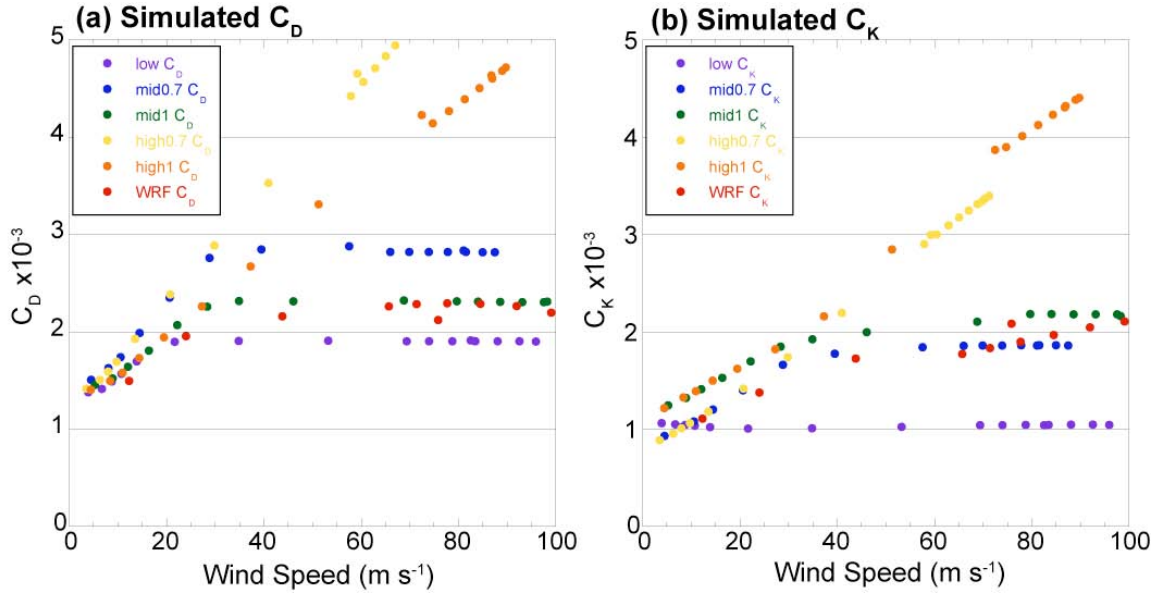


Figure 14.        Diagnosed (a) $C_D$ and (b) $C_K$ from five RE87 simulations and WRF simulation (see insets for color symbols) used in the sensitivity analysis.
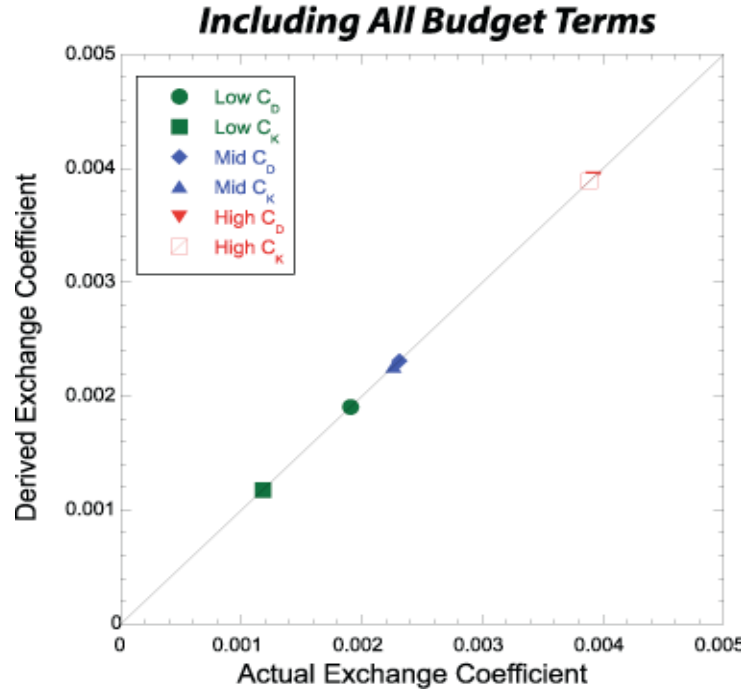
Figure 15.　　Retrieved exchange coefficients from selected RE87 simulations (see inset) using budget methodology with all terms included.

## D.　ERROR ANALYSIS

### 1.　Impact of Unresolved Budget Terms

The baseline validation of the methodology indicates excellent agreement between the derived and prescribed exchange coefficients when all budget terms were included. However, several of the terms cannot be estimated with the CBLAST dataset. Although the actual magnitude of the unresolved terms in nature is unknown, first-order estimates obtained from the RE87 output are shown in Figure 16. The root mean square values were determined from 1008 samples of the 6-hourly averaged simulated values from 168–288 hours in the RE87 integrations with different flux configurations. Control volumes were varied in size and shape from 18.5–44.5 km radius, and from the lowest model level (125 m) to 1.625–3.125 km altitude to get a representative sample of the various quantities. This analysis indicates that the leading term in the budget is the flux of mean quantities through the outer surface of the control volume, and the second leading term is the mean flux through the top of the volume—both of these terms are known quantities. Although the subtraction of several large-magnitude terms to obtain a small

45

residual generally is problematic in finite precision mathematics, in this case the desired surface fluxes are the third leading term, so there is some confidence in the ability to retrieve this quantity with reasonable accuracy. Radial eddy fluxes were the smallest terms in both budgets, which suggests that they can be neglected with minimal error in the inner core region. The two mean fluxes across the inner and bottom interface are known, with the latter being a smaller term that mainly satisfies integrated mass continuity. Unresolved terms of numerical significance are the volume-integrated tendency/storage term, the "shear flux" term, and vertical eddy fluxes. Each of these is discussed in more detail below.

Whereas the simulated storms were relatively steady in their intensities over multi-day timescales, the wind speed timeseries (Figure 10) indicates that there was non-negligible variability on hourly or more frequent timescales. Since the tendency term is integrated over the entire control volume, it has the potential to be a significant term in the budget. To examine the variability of the tendency term more carefully, budget retrievals were performed using both instantaneous and time-averaged model output. A finite-difference calculation for the momentum and energy tendencies on the original, staggered grid from consecutive model timesteps was found to be close to the recalculated value from the momentum (3.11) and energy (3.28) equations using unstaggered model output. A power spectrum of the intensity time series has a spectral peak at the 25-minute period (not shown), which is consistent with the period of a local inertial oscillation (Shapiro and Franklin 1995). However, the magnitude of the oscillation may be larger in the axisymmetric simulation than in observed storms. Experiments with different averaging periods appeared to damp this oscillation, but introduced additional errors in the storage term. Most notably, the unstaggered, time-averaged output did not explicitly enforce mass continuity with the numerical precision of the staggered, instantaneous gridpoint values. This discrepancy proved to be a significant source of error, with fluctuations in the retrieved exchange coefficient magnitudes exceeding 500%. This unacceptable level of uncertainty could be reduced by strictly enforcing mass continuity through a recalculation of vertical velocity from the given divergence field, but this adjustment led to unbalanced fields that required non-

46

negligible tendency terms to close the budget. In this sense, a larger tendency term can be alternately viewed as an artificial, residual storage of either momentum or energy inside the volume resulting from errors in the resolved fluxes across the top and sides of the control volume. These volume-integrated tendency terms also were found to be spatially coherent, and were manifest primarily as a sensitivity to the size and shape of the control volume if the terms were neglected. A more detailed examination of the sensitivity to the control volume is presented in Chapter III.E, but this order of magnitude analysis indicates that the estimated error in the exchange coefficients from neglecting this term is $\pm20$–100% for moderate $C_D$ and $C_K$ values (e.g., between 1 and 2.5 $x10^{-3}$).

The "shear flux" term represents an integrated loss of kinetic energy through the lower boundary resulting from the interaction of the mean wind shear and turbulent stress, $F_{SHEAR} = \int_{r_1}^{r_2} \left[ u\tau_{rz} + v\tau_{z\theta} \right] \Big|_{z_1} rdr$. The shear flux term is ~40–60% of the magnitude of the surface fluxes, which results in a significant low bias if neglected. However, the surface stress can be estimated by the bulk aerodynamic formula using the drag coefficient derived from the momentum budget, and the mean wind. This correction works well with the numerically modeled budgets when the drag coefficient is specified exactly, but in the real data the errors due to uncertainties in the surface stress and mean wind causes uncertainty. Sensitivity tests indicate that a $\pm50$% error in $C_D$ translates to a $\pm20$% error in the magnitude of $C_K$ from this term. To avoid adding too much noise to the $C_K$ estimates, the mean $C_D$ derived from all six missions was used in this study to estimate the surface stress used in evaluating the "shear flux" for $C_K$. Including errors in the mean wind, $\pm20$% appears to be a reasonable estimate of the $C_K$ error introduced by estimating this term.

Unresolved vertical turbulent fluxes at the top of the control volume are typically the same sign as the surface fluxes in the lower troposphere, which represents an unresolved flux of momentum into the volume, and a flux of energy out of the volume. This leads to an underestimation of both the drag and enthalpy exchange coefficients if neglected (see Equations 3.14 and 3.32). In the RE87 simulations, these eddy terms

47

showed a strong dependence on the altitude of the volume top, and were 10–30% of the surface flux magnitudes for the 1.625–3.125 km tops used in Figure 15.

For the CBLAST analysis, the choice of volume top is not straightforward. Traditional formalism for the planetary boundary layer assumes that the magnitude of the turbulent fluxes decreases to zero at the top of the PBL, but an examination of the vertical structure of turbulence using the CBLAST dataset (Zhang et al. 2009) suggests a separation of the TC boundary layer height defined mechanically and thermodynamically (Smith and Montgomery 2009). In between the outer rainbands of Hurricane Isabel, the potential temperature mixed layer depth was 400 m, while the momentum and humidity fluxes decreased to zero at 700 m, and the inflow layer extended to ~1 km. A similar depth of the inflow layer at the eyewall was reported in Montgomery et al. (2006), but the virtual potential temperature mixed layer was only 150 m deep. Smith et al. 2008 have suggested that the PBL has different characteristics in the main updraft region versus the inflow region outside the eyewall. In the eyewall, turbulent eddies may be transported upward where flow erupts abruptly out of the PBL. Under such circumstances, one might expect these turbulent contributions to increase the magnitude of the unresolved turbulent fluxes at the top of the control volume. Examining a range of relevant altitudes is a practical approach to addressing this uncertainty. Sensitivity tests described in Chapter III.E suggest that volume tops below and near the top of the inflow layer are the most appropriate for the budget calculation.
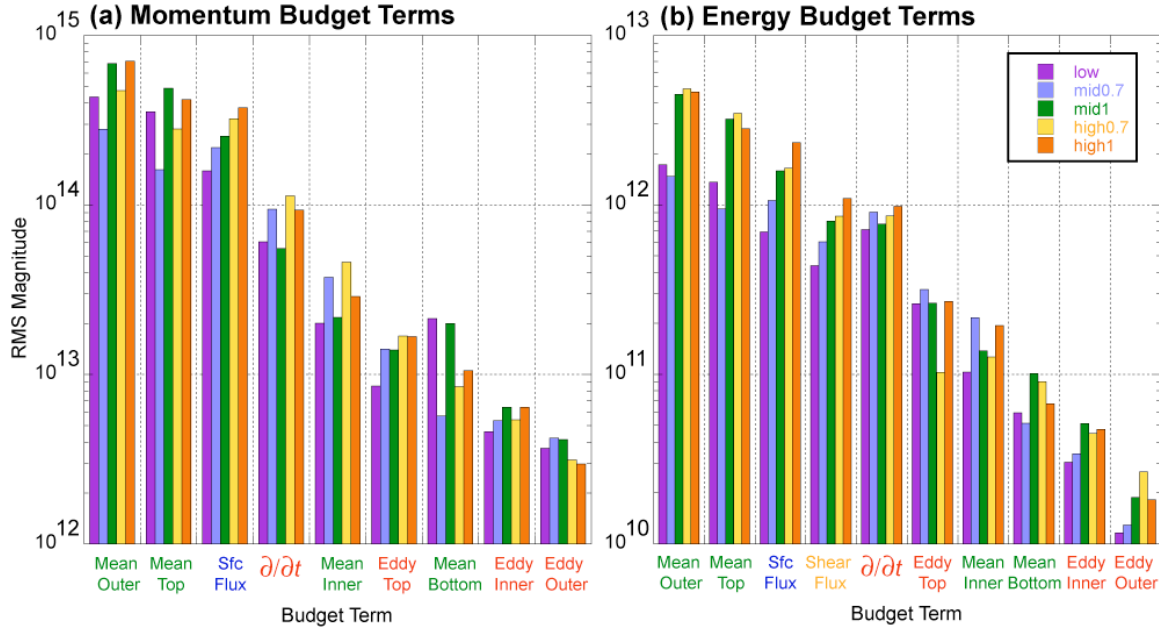
Figure 16.    Root-mean square magnitudes on a logarithmic scale of the (a) momentum budget terms and (b) energy budget terms from the RE87 simulations with different flux configurations (see inset). The colors of the budget terms along the bottom indicate which terms may be calculated or estimated from the CBLAST dataset – green are known terms, red are unknown terms, yellow is an indirectly estimated term, and blue is the desired surface flux term.

## 2.    Sea-Surface Temperature

The sea-surface temperature plays an important role in determining the enthalpy exchange coefficient by determining the saturation enthalpy at the sea surface ( $k^* = c_p T_{SST} + Lq^*$ ) and therefore must be measured accurately. Direct measurements of the SST were made during the Hurricane Fabian missions by AXBTs released by the NOAA aircraft. A comparison of the AXBT temperatures and TRMM microwave imager satellite estimates from the 3-day period prior to the first mission is illustrated in Figure 17 and summarized in Table 2. The TMI-derived sea-surface temperatures are near 28.5° along the track throughout the analysis domain, but the AXBT temperatures are consistently 1–2 degrees lower at the same locations. Since decreases of the SST are known to occur during and after the storm passage, the splash locations of the measurements were plotted in a storm-relative coordinate system (Figure 18). The AXBT measurements were near the eyewall (red annulus) with the exception of AXBTs #4 and

49

#8. On 2 September, the two AXBTs on the right side of the eyewall are ~1 C lower than the one released on the left side. Given the relatively good azimuthal sampling around the eyewall, an average value of 27° C was chosen for this mission. On 3 September, all of the AXBTs near the eyewall agree to within 0.4° C, and are consistently ~1.2° C lower than the TMI temperatures. A slightly higher value of 27.5° C was utilized on this day. It is interesting that the general location of Fabian on 3 September coincides with that of Isabel on 13 September. Since the SST is estimated at 27.5° C on both of these days, it appears that some of the ocean cooling that occurred during Fabian's passage recovered in the 10 days between the two storms. Only a single AXBT was available on 4 September, which was adjusted upward slightly to 28° C, given the warmer SST field derived from TMI in this region.

A comprehensive analysis of the SST for the potential intensity estimates for Hurricane Isabel in BM08 used satellite, buoy, and airborne radiometer measurements (Figure 19). Comparisons of the 3-day TMI product with the AVHHR estimates are good, and lend confidence to the prior estimates. Given the high bias of the TMI estimates in the Fabian case, the 29° C on 14 September used in BM08 was adjusted downward slightly here to 28.5° C. The 28.5° and 27.5° C sea surface temperatures obtained previously for 12 and 13 September, respectively, were not modified. It is possible that these estimates are a little high for these calculations, given the lower temperatures found underneath Fabian's eyewall, but without additional evidence they are the best estimates available of the SSTs.

SST errors do not affect the retrieved enthalpy flux, but do affect the corresponding exchange coefficient via the surface saturation enthalpy. The percentage errors in $C_K$ for 0.5° C SST error increments from both the WRF and RE87 output are shown in Figure 20. The two models agree quite well, which is largely expected since the error is not dependent on storm structure but only on the prescribed saturation enthalpy value. It is reasonable to assume the error is not much larger than 1° C, since all of the SST measurements are within a few degrees of each other, and are directly measured in the Fabian case. This would suggest an error of no more than 20% in the derived $C_K$.

Table 2.    Table of SST Observations for Hurricane Fabian

| AXBT # | D/ HH:MM:SS | AXBT SST | TMI SST | AXBT – TMI Difference | AXBT/TMI Average | Analysis SST |
|---|---|---|---|---|---|---|
| 1 | 2/ 17:25:24 | 26.64 | 28.95 | -2.31 | 27.795 | |
| 2 | 2/ 20:02:29 | 27.61 | 28.65 | -1.04 | 28.13 | |
| 3 | 2/ 20:17:40 | 26.88 | 28.5 | -1.62 | 27.69 | |
| 4 | 2/ 20:49:46 | 26.72 | 28.8 | -2.08 | 27.76 | 27.0 |
| 5 | 3/ 17:12:06 | 27.73 | 28.95 | -1.22 | 28.34 | |
| 6 | 3/ 17:38:25 | 27.4 | 28.65 | -1.25 | 28.025 | |
| 7 | 3/ 19:15:23 | 27.34 | 28.65 | -1.31 | 27.995 | |
| 8 | 3/ 20:34:07 | 27.64 | 28.5 | -0.86 | 28.07 | 27.5 |
| 9 | 4/ 19:44:36 | 27.49 | 29.1 | -1.61 | 28.295 | 28.0 |
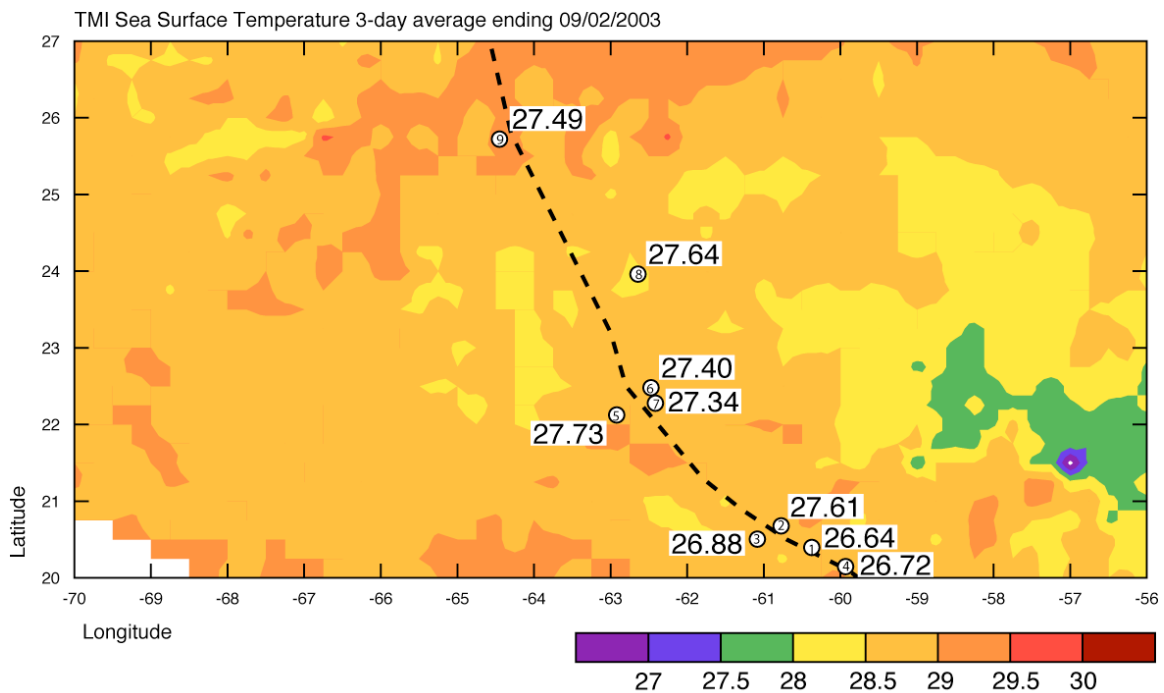


Figure 17.    SST derived from TRMM Microwave Imager satellite (average SST over 31 August to 2 September in color), and AXBT data released into Hurricane Fabian. Track of Hurricane Fabian (dashed best track, from 2 to 5 September) is shown for reference.
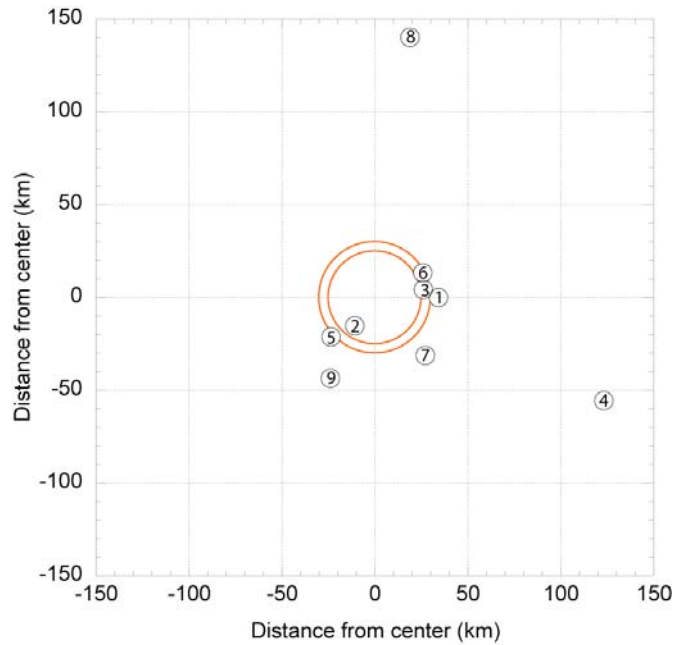
Figure 18.      Storm-relative AXBT splash locations. AXBT numbers correspond to Table 2. Red annulus corresponds to approximate eyewall location at 30 km radius from the storm center.
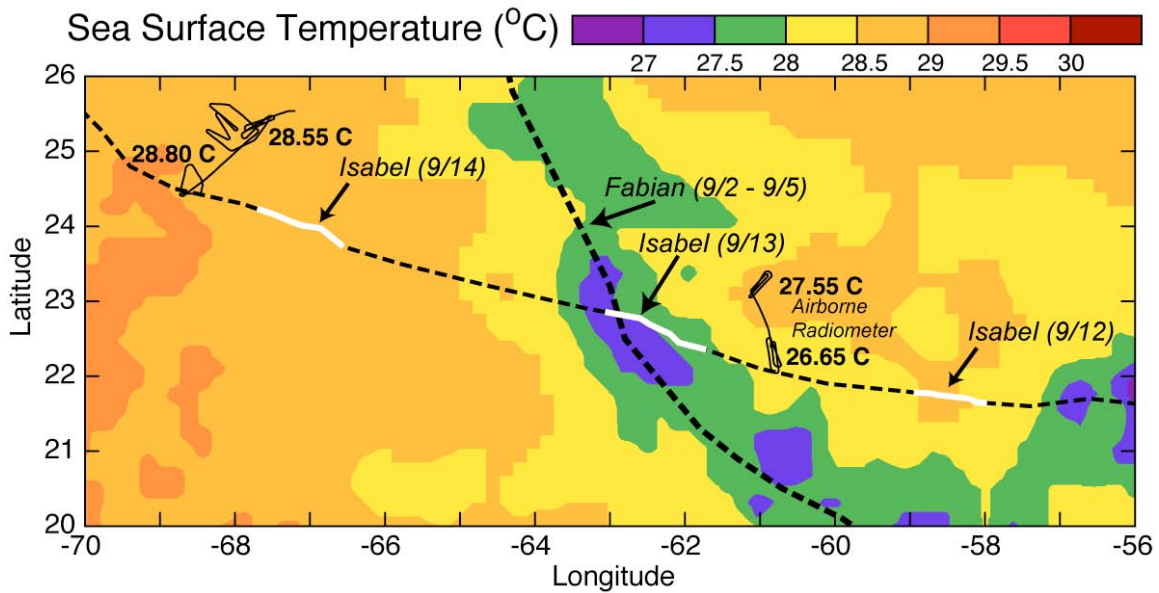


Figure 19.      SST derived from AVHHR satellite (average SST over 4 to 10 September in color), and NOAA WP-3D downward-pointing radiometer (thin line, from ~18Z 13 and 14 September). Tracks of Hurricanes Fabian (dashed best track, from 2 to 5 September) and Isabel (dashed best track, with thick white, solid line indicating analysis periods from 16–23Z on 12 to 14 September) are shown for reference. (From Bell and Montgomery 2008)
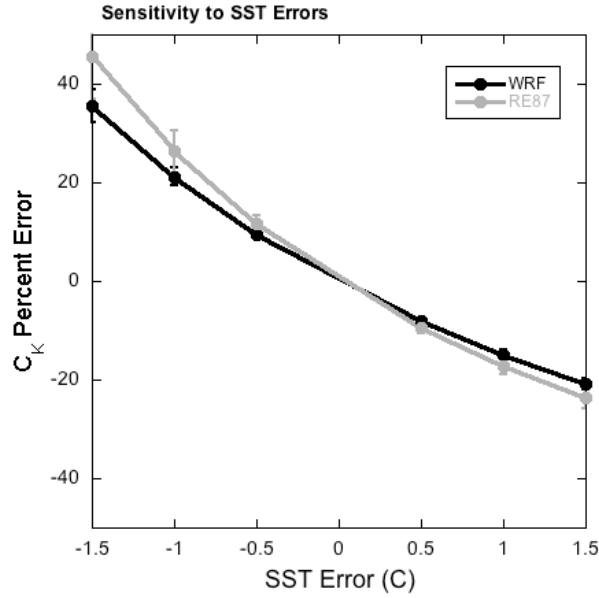
Figure 20.    Retrieved $C_K$ sensitivity to errors in sea-surface temperature using RE87 and WRF model runs. Units are in percent for the $C_K$ error.

## 3.    Circulation Centers

It is well known that an inaccurate center can lead to errors in the Fourier decomposition of a storm's kinematic and thermodynamic structure in cylindrical coordinates (Marks et al. 1992; Lee and Marks 2000; Bell 2006). While a transformation of the data into cylindrical coordinates does not change a field (except for the singular point at the origin), the incomplete representation of the field by a finite series that truncates higher-order harmonics does introduce error. This limitation is particularly important when only the wavenumber zero mode is retained, as aliasing to higher wavenumbers is manifest as errors in the derived axisymmetric winds, energy, and mass fields. For scalar fields, center errors are manifest as radial displacements of the measured quantity, such that sufficient averaging can largely eliminate random errors. For vector fields, a center displacement in the radial direction has the same effect as merely moving the observation inward or outward from the displaced center. Sensitivity tests indicated that this type of error leads to minimal errors in the budget retrieval. However, displacements of the center in the transverse direction lead to a re-partitioning of the winds into the tangential and radial component.

It can be shown from geometrical considerations in a polar coordinate system that the re-projected wind components are given by $\tilde{u} = ur/\tilde{r} + ve/r$ and $\tilde{v} = vr/\tilde{r} + ue/r$, where $e$ denotes the transverse error in the center, $u$ and $v$ are the actual radial and tangential wind components, $r$ denotes the radius of the observation, and tildes indicate erroneous quantities with $\tilde{r} = \sqrt{e^2 + r^2}$. Since $r/\tilde{r} \approx 1$ for typical center errors away from the eye, the percentage errors are approximately given by the second terms in each equation. Given that $v \gg u$, it is clear that the largest errors would be found in the radial component on the inner side of a budget control volume. For example, a 5 km displacement of a 60 m s$^{-1}$ tangential wind at 20 km radius would yield a 15 m s$^{-1}$ error in radial wind. Weighting this error by mass, radius, and energy or angular momentum and integrating over the column/ring yields a large error in the resolved flux across the boundary of the control volume. In cylindrical coordinates, integration errors are compounded as the depth of the volume increases, which lends some support for the use of shallower control volumes that still exceed the depth of the boundary layer. The fact that the error is radially dependent means also that an artificial gradient of the radial wind is introduced, which produces an erroneous residual flux into the volume and inaccurate radial divergence. Since changes in the divergence affect vertical motion, the error also would be spread to the flux across the top of the control volume. All of these error implications add sensitivity to the choice of the control volume.

Sensitivity tests with the RE87 model confirm the large errors described above when applied to an individual model output, whether instantaneous or time-averaged. Standard deviations of the percentage error for both drag and enthalpy coefficients were ~25% per km center error, such that center errors of 4 km had a ±200% variation at the 95% confidence level. It is partly for this reason that individual radial penetrations and dropsonde sequences were not used to calculate the budgets, since a center error can be significant on a single pass. Fortunately, if the center displacements are predominately random, then averaging of multiple passes with independently derived centers reduces the errors in the winds and thermodynamics, which suggests that the analytic results are really a worst-case scenario. However, this also indicates that reducing center errors is critical to obtaining meaningful results from the budget.

Since a variety of ways exist to define the center of a tropical cyclone, there is no unique tropical cyclone center, but there may be an optimal center to minimize aliasing associated with a truncated Fourier representation. The simplest definition of a TC center is where the earth-relative wind goes to zero. For a moving vortex, the *wind* center then depends on the translation speed and is not ideal for most quantitative applications. The most commonly used center in TC studies is the 6-hourly "best track" center published by the National Hurricane Center. These centers are derived from a variety of sources and are accurate to approximately 10 km for strong hurricanes. While some of these centers can be highly accurate when aircraft reconnaissance is available near the 6-hourly interval, the low temporal resolution of the fixes smoothes out any high spatial resolution movement such as trochoidal oscillations (Nolan et al. 2001). Although the best track is sufficiently accurate for comparison with forecast tracks, which typically are concerned with errors >100 km, it is not optimal for deducing axisymmetric structures. In previous studies using the current dataset (Montgomery et al. 2006; Bell 2006; BM08), the centers were determined by the method described by Willoughby and Chelmow (1982), in which flight-level pressure and wind observations are used to find the streamfunction minimum for a axisymmetric vortex in gradient wind balance. In the absence of multiple local minima that may arise from transient mesovortices, this *dynamic* center is accurate to 3 km and is the preferred method for high-resolution centers when only flight-level data are available. A third center-finding method proposed by Marks et al. (1992) used Doppler radar data to determine the *circulation* center that maximizes the axisymmetric tangential wind at the RMW. Since this maximum is an inflection point in the radial gradient of tangential wind, it also maximizes the vorticity and therefore the circulation inside the RMW. An alternate center definition using both the gradients of angular momentum and energy also was considered, but was difficult to implement given the need for accurate gradients of thermodynamic information. In the case of a stationary, circular, vertically aligned vortex in gradient wind balance, the wind, dynamic, and circulation centers would be identical. As a TC translates and its structure departs from axisymmetry and vertical alignment, these centers begin to diverge.

For the current study, the availability of edited, dealiased Doppler radar data made the circulation center an attractive choice. To determine the circulation center, a two-dimensional "simplex" search (Neldar and Mead 1965) on a gridded dual-Doppler wind field (Mohr 1988) with 1.5 km horizontal grid spacing finds the point that maximizes the average value in an annulus around a specified radius. A 3-km annulus was used in this study, and an azimuthal average spanning at least 60 degrees was enforced to prevent small-scale wind maxima from dominating the average. The simplex search compares the average tangential velocity at the three vertices of a triangle whose centroid is an initial guess of the TC center. The algorithm uses reflection, contraction, and expansion of the triangle to find the maximum tangential velocity. To ensure a global maximum was found, the simplex search was initialized at 16 locations over 15 radii bracketing the estimated center and RMW, respectively. A mean center was deduced from the different simplex solutions at 1-km altitude for each radial penetration of the airborne radar. Cubic-spline interpolation of the individual centers over time was then used to create a 1-second track. The track was reviewed subjectively for outliers, and some minor adjustments were made after identifying centers that may have been biased by local wind maxima. The accuracy of individually derived circulation centers is ~3 km due to errors in the gridded dual Doppler analysis and spatial averaging used in the simplex search. However, the use of a broader swath of radar-derived wind data helps to eliminate centers associated with mesoscale vortices that distort the center fixes from the Willoughby and Chelmow (1982) method. Most importantly, since these centers maximize the symmetric tangential wind *by definition*, they also minimize any artificial high-order harmonics in the Fourier decomposition.

An example of the center-finding method for a radial penetration of Hurricane Isabel at 1650 UTC 12 September 2003 is shown in Figure 21. A composite radar reflectivity from the lower fuselage 5 cm, C-band radar (color) reveals the nearly symmetric eyewall with values exceeding 40 dBZ that is superimposed on a swath of winds at 1-km altitude from the tail Doppler radar on the southwest side of the vortex. The white typhoon symbol indicates the location of the radar-derived circulation center, and the white circle indicates the estimated RMW. Note that the vectors are nearly

56

tangential to the white RMW circle, and that the RMW circle also follows the curvature of the outer edge of the eyewall reflectivity well in this region. Discrepancies between the circle and reflectivity elsewhere are likely due to temporal and spatial averaging of the higher beamwidth (e.g., coarser) lower fuselage data. The NHC best-track center interpolated to this time (black closed), and dynamic center from the flight-level data (black open) are also shown for comparison. The best track center in this case is very close to the circulation center, with the dynamic center displaced to the southwest in the low reflectivity region. It is possible that the dynamic center was influenced by one of the large mesovortices present in the eye at that time (Kossin and Schubert 2004; BM08). This comparison indicates that the radar-derived circulation center is the optimal one for the axisymmetric budget calculations.

The NHC best-track and the high-resolution tracks derived from the simplex searches are shown for all six missions in Figure 22. As expected, the tracks are nearly coincident, but the higher resolution motion is apparent in the colored tracks. The largest discrepancy appears to be on 13 September, where the differences are likely due to the different center definitions, but are still well within the large eye and RMW on this day. It is reasonable to assume that no systematic biases are present in the tracks, such that random errors in the center would be largely minimized by the variational analysis technique. Sensitivity tests with minor variations to the observed tracks were consistent with this hypothesis, and did not indicate any significant changes in the retrieved exchange coefficients for displacements on the order of 1–3 kilometers. The error remaining in the exchange coefficients after averaging the observations from multiple radial penetrations is estimated at ±20%.
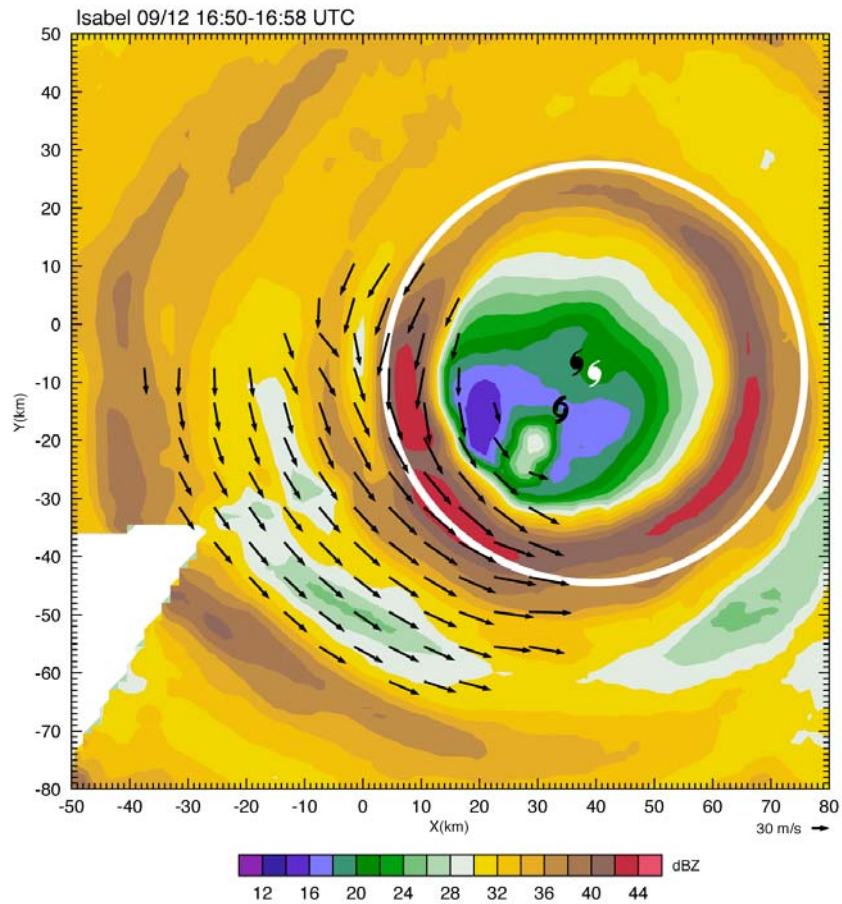
Figure 21.    Radar analysis of Hurricane Isabel from 16:50–16:58 UTC 12 September, showing reflectivity composite from lower fuselage radar in color with dual Doppler horizontal winds at 1-km altitude (vectors). Hurricane symbols indicate centers derived from radar (white), NHC best track (closed black), and aircraft winds (open black). White circle indicates radius of maximum wind from radar-derived center.
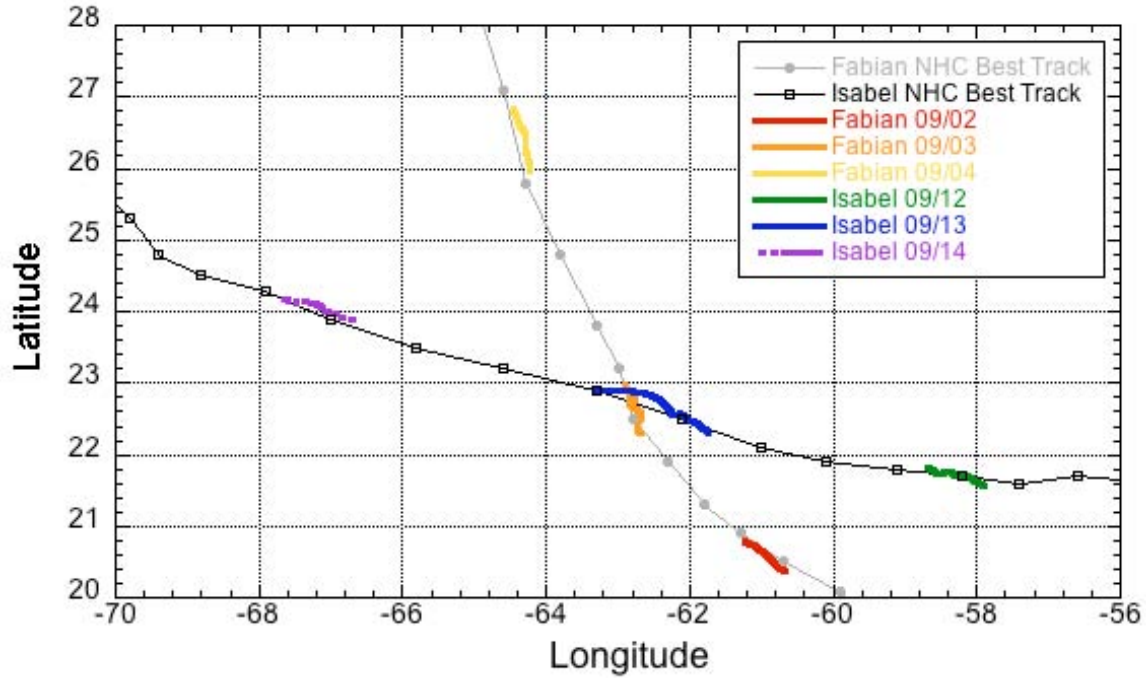
Figure 22.    NHC best tracks (black and gray) and radar-derived tracks (color, see inset) used in this study for Hurricanes Fabian and Isabel.

## 4.    Gridded Analysis

To integrate the kinematic and thermodynamic integrals numerically in Equations (3.15) and (3.33), the data must be available at specific grid points. For the previous TC momentum and energy budget studies, this was done by a manual map analysis that was then interpolated to regular intervals. This analysis was largely superseded by the development of objective analysis techniques that created a gridded data field by weighting the observations by their distance from a particular gridpoint. Modern data assimilation techniques have continued to improve the analysis of data, by including observational error, a priori background estimates of the atmospheric state and, in some cases, time-dependent probabilistic information on the background errors.

For the current study, a variational analysis technique was developed based on the work of Ooyama (1987) and modern data assimilation methods. The objective of this method is a maximum likelihood estimate of the atmospheric state for a given set of observations and error estimates. A detailed derivation and description of the SAMURAI (Spline Analysis at Mesoscale Utilizing Radar and Aircraft Instrumentation) is given in

Chapter IV. Although the statistical correlation between the resulting SAMURAI analysis and the CBLAST observations is very good and yields high confidence in the derived TC structures used in the momentum and energy budgets, errors arising from the gridded representation of the observations must still be considered.

Although variational analysis is superior to objective or manual analysis in a probabilistic sense, shortcomings still exist in the practical implementation due to incomplete knowledge of the observational and background errors. In a variational analysis, the derived structure conforms to new observations where available, and relaxes back to the *a priori* background state where no new information is provided. Given the relative lack of gridded, axisymmetric analyses of mature TC structure, the error estimates for the background state are uncertain. For the current study, a Gaussian background error covariance was assumed with an influence length scale based on the observation density. The background errors were purposefully set high in order for the analysis to conform primarily to the observations where available, but this has the detrimental side effect of making the analysis unconstrained in data-poor regions. Similarly, the background error length scale acts as both an effective distance for the observations and as a spatial filter; a large value helps spread the information provided by an observation but also tends to overly smooth the analysis. An appropriate balance must therefore be struck between these trade-offs. This balance was assessed by varying the specified length scale and subjectively examining the resulting gridded fields of the numerical model output and the CBLAST analyses.

With the exception of the transverse streamfunction $\psi$, the majority of the gridded fields were found to be relatively insensitive to the specific choice of the error length scale other than the level of detail. Since the secondary circulation depends on the derivatives of this streamfunction, even relatively smooth fields of $\psi$ can produce substantial variations in $u$ and $w$ in regions where the derivative is not properly constrained by either the observations or the background field. This deficiency was found to be most significant in the lowest 100 meters of the analysis domain, where the signal from many dropsondes was lost and no Doppler radar information was available. An example of the sensitivity of the radial wind at the surface to dropsonde coverage and

three background error length scales is shown in Figure 23. In the main eyewall region, the radial wind profiles are very similar and provide a good least-squares fit to the observations. In the data gap regions near the eye (10–20 km radius) and outside the eyewall (>50 km radius), the solutions diverge significantly. The most radical is the 4x (e.g., 400 m vertical, 4 km radial) length scale, which has a large oscillation in the radial wind in the data-poor region. However, this was eliminated largely by using the 6x filter. The differences between the 4, 6, and 8x radial winds are pronounced at the outer boundary, with nearly a 40 m s$^{-1}$ difference where no observations are available to constrain the solution. This is partially because the absolute errors in $\psi$ increase with radius as the magnitude of the streamfunction increases, and partially due to the lack of an ideal vertical boundary condition on the streamfunction near the surface. Since $\psi = 0$ at the surface constrains the value but not the derivative, setting the first or second derivative to zero introduces an artificial structure in the radial wind. In this study, a third-order derivative constraint is used to damp oscillations of $\psi$ near the surface, but the magnitude of this constraint is constant over the domain. These tests indicated that the 6x background error length scale is a good trade-off between too much smoothing and the data density constraints, and is adequate for the current study. More research on the proper boundary condition for the cubic spline analysis of the streamfunction is recommended for future applications, with alternative spline coefficients, a variable derivative constraint, or anisotropic background error covariance possibly improving the near-surface solutions in data-poor regions.

An additional factor that improved the analysis was the incorporation of Doppler radar data. In BM08, the Barnes objective analysis of Hurricane Isabel used the equivalent of a ~10x filter to damp noise and spread the dropsonde information across data gaps. By incorporating radar data, the dramatic increase in both azimuthal and radial data density for the kinematic variables adds significant value to the analysis and helps reduce the amount of filtering required. Without the radar data, the surface radial wind sensitivity (Figure 23) extends through a much deeper layer. Ultimately, higher quality and quantity of observations lead to better analysis, such that the highest confidence in the gridded fields was in the eyewall region where the best data coverage

was available. The budget control volumes were therefore centered on the regions with both the best observations and the highest wind speeds.

As an additional test of the errors associated with the gridded analysis, the RE87 model output was treated as simulated observations and analyzed with the identical SAMURAI configuration used for the real observations. A comparison of the "mid0.7" wind field at 168 hours is shown in Figure 24. The analyzed and the raw model fields compare well, and the structure is very similar to that in the "low" output at the same simulation time (c.f., Figure 11). Whereas the raw model and analyzed tangential winds are nearly identical, the analyzed radial winds are noticeably smoother than the raw model output, especially in the peak magnitude of the inflow and outflow at the RMW. The effect of the boundaries is also apparent, with a broader region of strong outflow at 4 km in the analyzed field and a bend in the radial wind contours near the surface. Since the lowest model was 125 m, the specification of winds near the surface is arbitrary in this case and is not necessarily representative of an error. In general, the analysis faithfully reproduces the kinematic structure with a 0.9984 statistical correlation, a ~1% RMS difference of the variables other than the radial and vertical wind. There is a ~28% RMS difference for the radial and vertical wind, with most of the differences occurring near the boundaries. The 6x filter length is perhaps too heavy for a "perfect" data distribution, but is a fair trade-off with the CBLAST data. Given the uncertainties described above, it is estimated that errors arising from the gridded analysis procedure contribute less than a 20% error in the derived exchange coefficients.
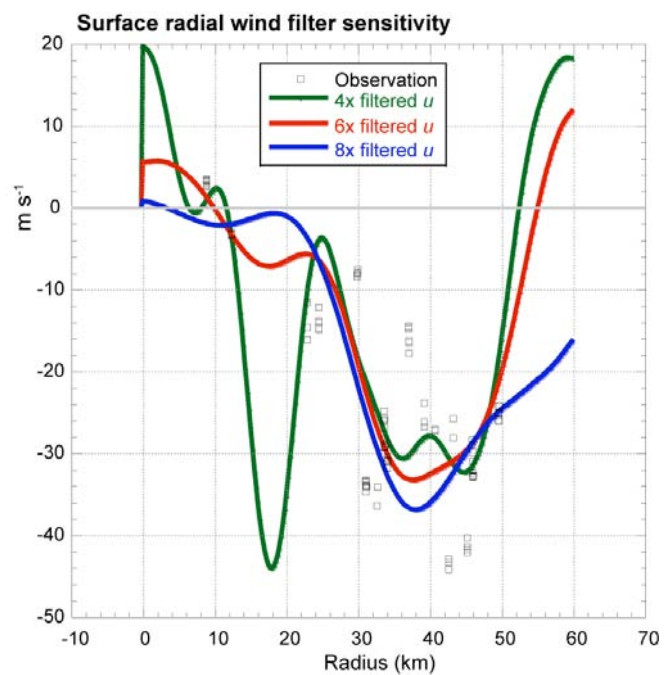
Figure 23.    Surface radial wind sensitivity to background error length scale and gaps in the dropsonde data on 13 September. The dropsonde wind observations below 50-m altitude on 13 September are marked by squares, and three analysis curves with different background error covariance length scales are shown in color (see inset).
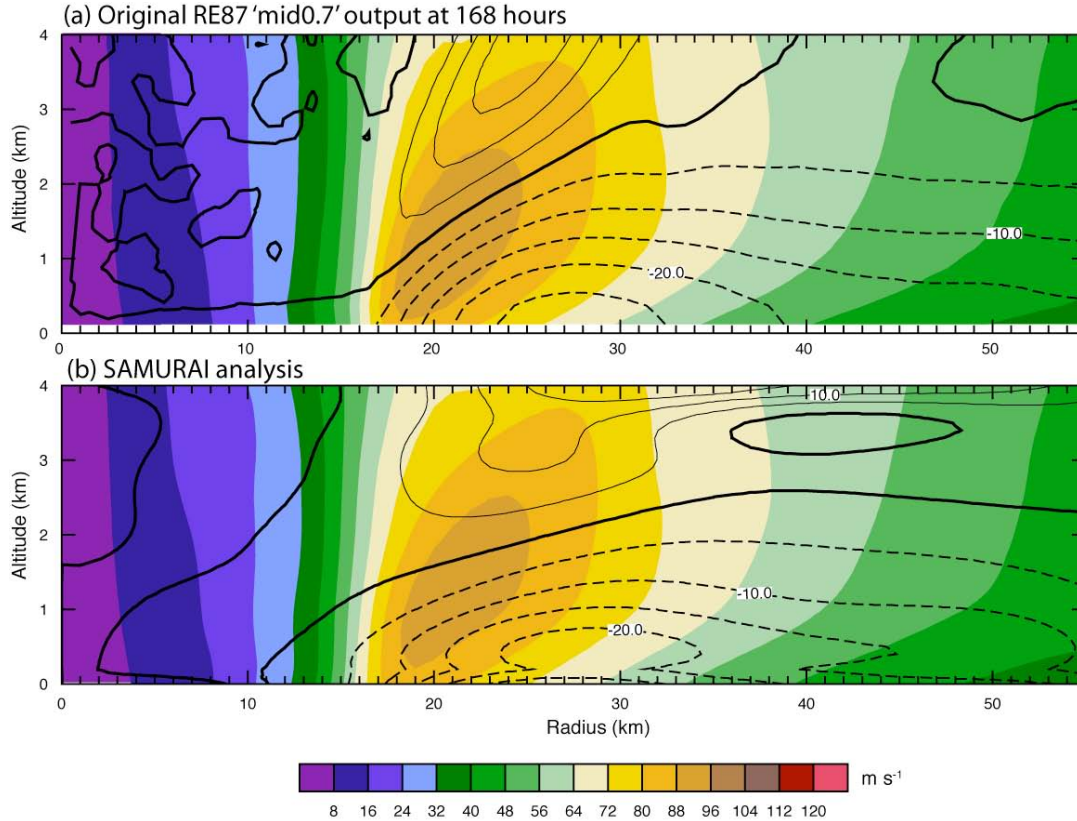
Figure 24.    RE87 raw model output from "mid0.7" simulation at 168 hours (panel a) compared to SAMURAI analyzed fields (panel b). Tangential winds (m s$^{-1}$ shaded, scale at bottom), and radial winds (5 m s$^{-1}$ contours) with dashed contours indicating inflow and solid contours indicating outflow. The thick black contour indicates zero radial wind.

## E.    DERIVED EXCHANGE COEFFICIENT SENSITIVITY USING SIMULATED DATA

The previous analysis of the (i) unresolved budget term magnitudes and (ii) SAMURAI gridded analysis method suggest that errors in the derived bulk exchange coefficients could be significant even if the SST and circulation centers were known exactly. This motivates the following test of the methodology using simulated observations from the numerical model output analyzed by SAMURAI with no instrument or center errors. Using this test, the following questions are addressed:

1.    How precisely can one estimate the exchange coefficients?

2.    Is there an optimal geometrical configuration (width and height) for the budget control volume?

64

To more accurately estimate the minimum uncertainty in the coefficients given "perfect" observations, a series of sensitivity tests was conducted to guide the specification of the optimal configuration of the budget control volume when real data will be used. The 6-hourly averaged output from 168–288 hours from all five of the RE87 runs, and the hourly-averaged "figure-4" analysis from 144–168 hours of the WRF simulation were analyzed with the SAMURAI program using the same configuration as done for the real data. A wide variety of control volumes were then tested and compared with the known exchange coefficients.

One of the first steps was to determine the sensitivity to magnitude of the exchange coefficient using the re-analyzed RE87 output as shown in Figure 25. The large quantity of model output and extensive variety of the control volume parameter space (e.g., variable inner radius, width, and depth) yielded ~21,500 retrievals. From this test, generally more negative percentage errors are found for the "high" drag coefficients ($>3.5\text{x}10^{-3}$), since only a few samples are above zero (Fig. 25a). A slight linear correlation exists in the largest enthalpy coefficients (Fig. 25b), which generally corresponds to increasing average wind speed in the control volume. For the lower magnitude exchange coefficients, no particular dependence is found on the magnitude of the coefficient, with numerous samples containing both high and low percentage errors. Although the percentage error in Figure 25 seems to be a useful metric for examining the problem, absolute errors for the higher magnitude coefficients may be on the same order as the lower values of the exchange coefficients. Since a systematic bias clearly exists for the "high" exchange coefficients, these were removed from further consideration to ensure the magnitudes correspond more closely to the actual retrieved magnitudes from the CBLAST dataset. A total of ~12,900 retrievals remained after the "high" simulations were removed. This subset of the data does not have a systematic low bias, and has percentage errors that correspond to absolute errors with similar magnitudes.

The sensitivity of the drag coefficient to the control volume geometry for the "low" and "mid" simulation samples is shown in Figure 26. The sensitivity to the control volume depth (Fig. 26a) has a parabolic trend with an apparent low bias for almost all depths. However, a positive peak in the distribution is found around 1500 m, which is just

below the inflow top for these simulations. The sensitivity to the control volume width has a decreasing spread of the uncertainty with wider volumes, but also has a consistently low bias at the widest annulus of 22 km. A useful metric for combining these two parameters is shown in Fig. 26c, where the width/depth "aspect ratio" defines the shape of the volume. The spread of the uncertainty decreases from low aspect ratios (e.g., taller, thinner volumes) to high (e.g., shorter, wider volumes), but also indicates a consistently low bias at the higher ratios. The sensitivity to the location of the inner edge of the control volume (normalized by the RMW) has a general low bias but with a peak around 0.8 in the distribution.

The RE87 sensitivity of the enthalpy exchange coefficient (Figure 27) has similar patterns with respect to the depth, width, and aspect ratio of the control volume (Figures 27a-c), and to the location of the inner radius (Figure 27d). The parabolic shape of the depth sensitivity distribution peaks at a slightly higher height, and is more symmetric about the zero error baseline. The other three panels indicate a trend toward a low bias at the upper end of the tested ranges, but not as large of a low bias as the drag coefficient distributions at the same values.

The control volume sensitivity tests for the drag coefficient (Figure 28) and the enthalpy exchange coefficient (Figure 29) with the WRF simulation have similar trends with respect to increasing depth, width, aspect ratio, and inner radius as in the RE87 results, but with different bias characteristics. A parabolic shape is evident in the sensitivity to the depth of the control volumes, with peaks at a lower altitude near 1000 m and 400 m for $C_D$ (Figure 28a) and $C_K$ (Figure 29a), respectively. The percentage errors become more negative for increasing volume width (Figures 29a and 29b). The aspect ratio sensitivity (Figures 28c and 29c) appears to have the most similarity with the RE87 results, and indicates a decreasing spread of uncertainty at higher ratios. However, a distinct difference exists in the overall bias of the WRF results, with most of the $C_D$ sensitivity tests having positive errors and the $C_K$ sensitivity tests having mostly negative errors. Since the WRF model had two sigma layers below 100 m, an additional sensitivity test was performed by varying the lowest level of the control volume (e.g., $z_1$ in Equations (3.15) and (3.33)). This test indicated a general tendency for slightly lower

exchange coefficients with $z_1$ equal to 100 m versus at the surface. However, no discernable high or low bias existed for either level (not shown).

One of the most significant findings from this series of tests is that the errors were not uniform from model to model. No single control volume was found that minimized both the bias and spread of uncertainty for both the drag and enthalpy exchange coefficients in both models. It is probable that the magnitude of the individual unresolved budget terms is different in the 3D WRF simulations versus the 2D RE87 simulations, but the overall errors were comparable. To determine whether this was primarily due to the differences in the 2D versus 3D simulations, or some other facet of the simulations, an additional sensitivity test varying the vertical mixing length in the RE87 model was performed. This parameter partially controls the size of the turbulent eddies in the RE87 simulations, and was set to 200 m in the five original simulations. Lowering this value to 100 m for the "low" flux configuration produced a simulation with a similar overall intensity, but with a slightly shallower inflow layer. The drag coefficient sensitivity to control volume depth is compared for these two simulations and the WRF model in Figure 30. Although the two RE87 simulations have similar error profiles, a shift to a shallower peak in the parabolic profile is found for the 100 m vertical mixing length simulation. This suggests that at least some of the error differences are due to differences in the simulated structure, and not solely the 2D versus 3D geometry of the simulations.

A common feature of all the simulations is a trend toward a decreased spread of the percentage error for larger aspect ratios. This can be interpreted as an increased numerical stability as a larger integrated surface flux term is solved with wider control volumes. A trade-off then exists since wider volumes must account for the variability of the wind speed with radius, but given the larger numerical sensitivity of the exchange coefficients retrieved from thinner volumes, these wider volumes appear to be necessary. The sensitivity tests also indicate a parabolic error trend for increasing depth of the control volume, with a peak in the distribution just below the top of the inflow layer. Although the peaks were not necessarily correlated with a zero bias, they are believed to be related to the levels at which the vertical eddy fluxes become small (i.e., the top of the boundary layer). These vertical eddy fluxes may not go to zero like in the rainband region

as studied by Zhang et al. (2009). However, it is reasonable to assume that the vertical eddy fluxes are smaller at or near the top of the boundary layer compared to the surface fluxes. Sensitivity analysis of the retrieved fluxes from the observations show similar trends in the magnitude of the fluxes with depth of the control volume. The parabolic profile, as opposed to an increase with depth followed by a leveling off, suggests an accumulation of errors in the integrated energy or momentum flux through the sides of the control volume with increasing height. Therefore, both physical and numerical reasons exist to suggest that control volumes with tops near the top of the boundary/inflow layer and a width that includes a sufficiently large integrated surface flux are the best choice for minimizing error.

Since the volume depth is constrained by the inflow layer, the aspect ratio sensitivity gives reasonable guidance on the volume width necessary to reduce the uncertainty of the retrieved $C_K$ and $C_D$. These results suggest a minimum aspect ratio of ~20 before the spread of the percentage error decreases to ~±50%, which would correspond to a width of 20 km for a 1-km deep volume. The data distribution ultimately constrains the maximum width of the control volume because of the uncertainties in the structure arising from fewer observations outside of the eyewall region. Therefore, an aspect ratio range of 20–30 is a reasonable range of the control volume parameter space given the observed inflow depths and data distribution.

A summary of the WRF and RE87 error mean and standard deviation filtered to these aspect ratios is shown in Figure 31. The absolute error (left panel) indicates the smallest bias is found in the retrieved WRF $C_D$ and RE87 $C_K$, with standard devations of $0.76 \times 10^{-3}$ and $0.61 \times 10^{-3}$, respectively. A distinct low bias is found in both the RE87 $C_D$ and WRF $C_K$, with standard deviations of the error of 0.49 and 1.04, respectively. In terms of percentage error (right panel), these standard deviations correspond to 21–55%, with biases ranging from +12 to -59%. The largest biases or standard deviations are not confined to a particular model or exchange coefficient, but appear to be relatively independent. Although the simulations are idealized and the structures are only semi-realistic, it is believed that these results can provide useful guidance on the error characteristics associated with a particular set of control volumes, but do not specifically

68

describe the biases of the real dataset. However, the significant bias and uncertainty of these results do indicate that the methodology is sensitive to the control volume specification, even within this range. It is difficult to say how much of this error is related to the models versus the methodology. It is reasonable to assume that some of this error is due to noise in the models, given the temporal fluctuations in tangential wind apparent in Figure 10. However, the non-negligible magnitude of the unresolved budget terms is likely the main source of error. The errors associated with the control volume dimensions are therefore estimated conservatively at ±50%, but it is acknowledged that they may be higher than this.

A summary of the errors identified by the sensitivity tests is given in Table 3. The potential errors are those that could be present if no steps were taken to address the problem, with the estimated errors those that are still present after the mitigation. The largest source of error appears to be the neglect of the unresolved budget terms, specifically the volume-integrated tendency and vertical eddy fluxes at the top of the control volume. This error is estimated at ±50% but, as mentioned above, this may be an under-estimate. The remaining errors all are estimated to be on the order of ±20% after mitigation. Fortunately, these errors are independent and random, and there is no reason to expect that they would be cumulative. These percentages are reasonable estimates based on the analytical and numerical tests performed with the model data. These tests also have identified the areas for which additional effort was required to ensure the best possible results from the observational dataset. If left unconstrained, the potential errors listed easily overwhelm the magnitudes of the retrieved exchange coefficients. The errors are non-negligible even after mitigation, but still are believed to allow meaningful interpretation of the results.
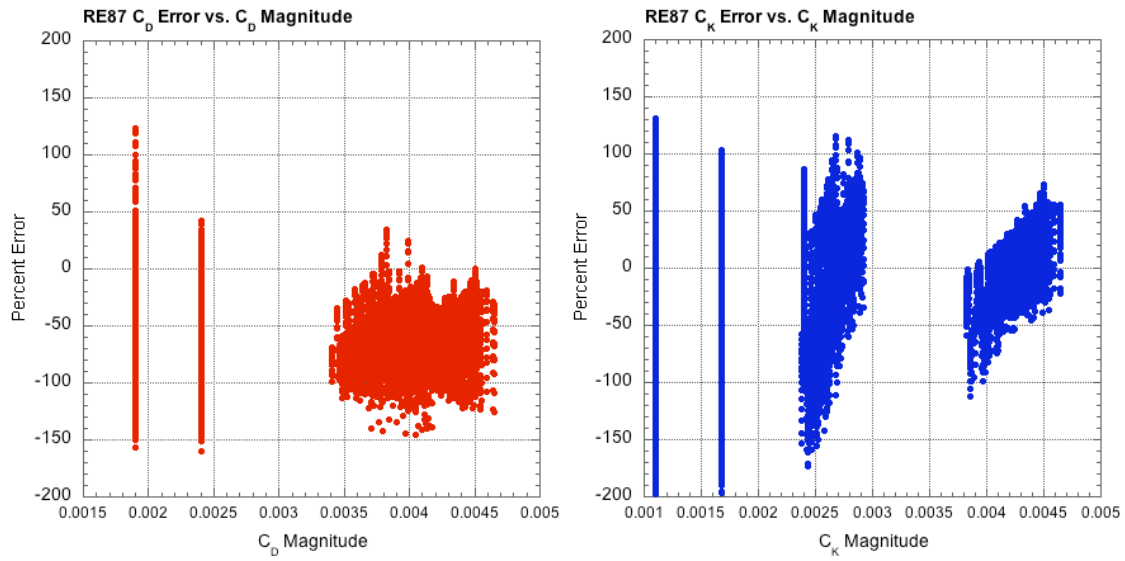
Figure 25.      RE87 sensitivity to the magnitude of the exchange coefficients. Clusters indicate similar magnitude coefficients in each of the five simulations. Each dot represents the percentage error of an individual retrieval of an exchange coefficient using a single control volume at a single (6-hourly or hourly) time interval from one of the five RE87 simulations.

70
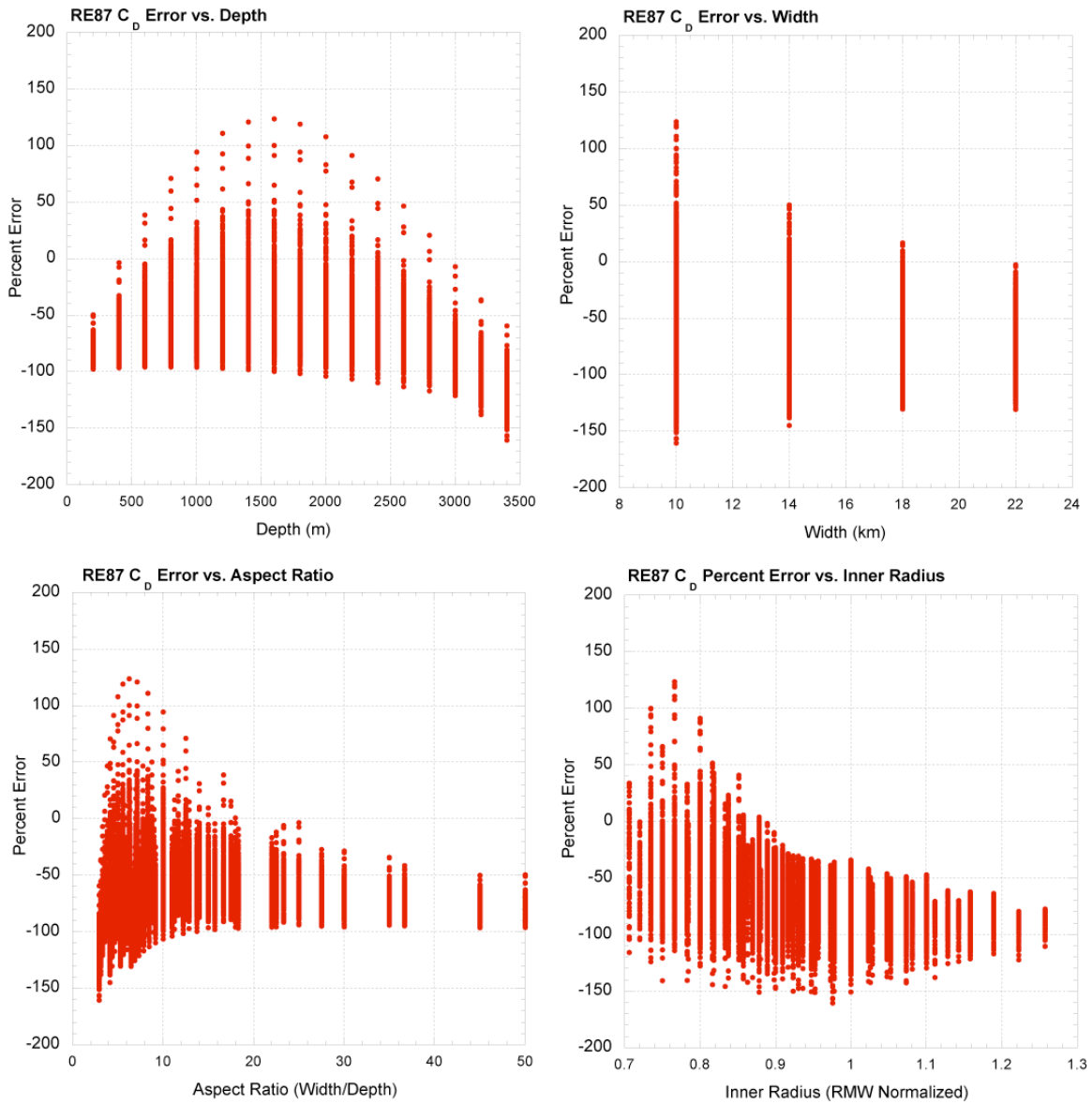
Figure 26.        The percentage error in the retrieved $C_D$ from the RE87 simulations obtained by varying (a) the depth of the control volume, (b) the width of the control volume, (c) the aspect ratio (defined as the width/depth), and (d) the location of the inner radius normalized by the radius of maximum winds. Dots are the same as in Figure 25.

71
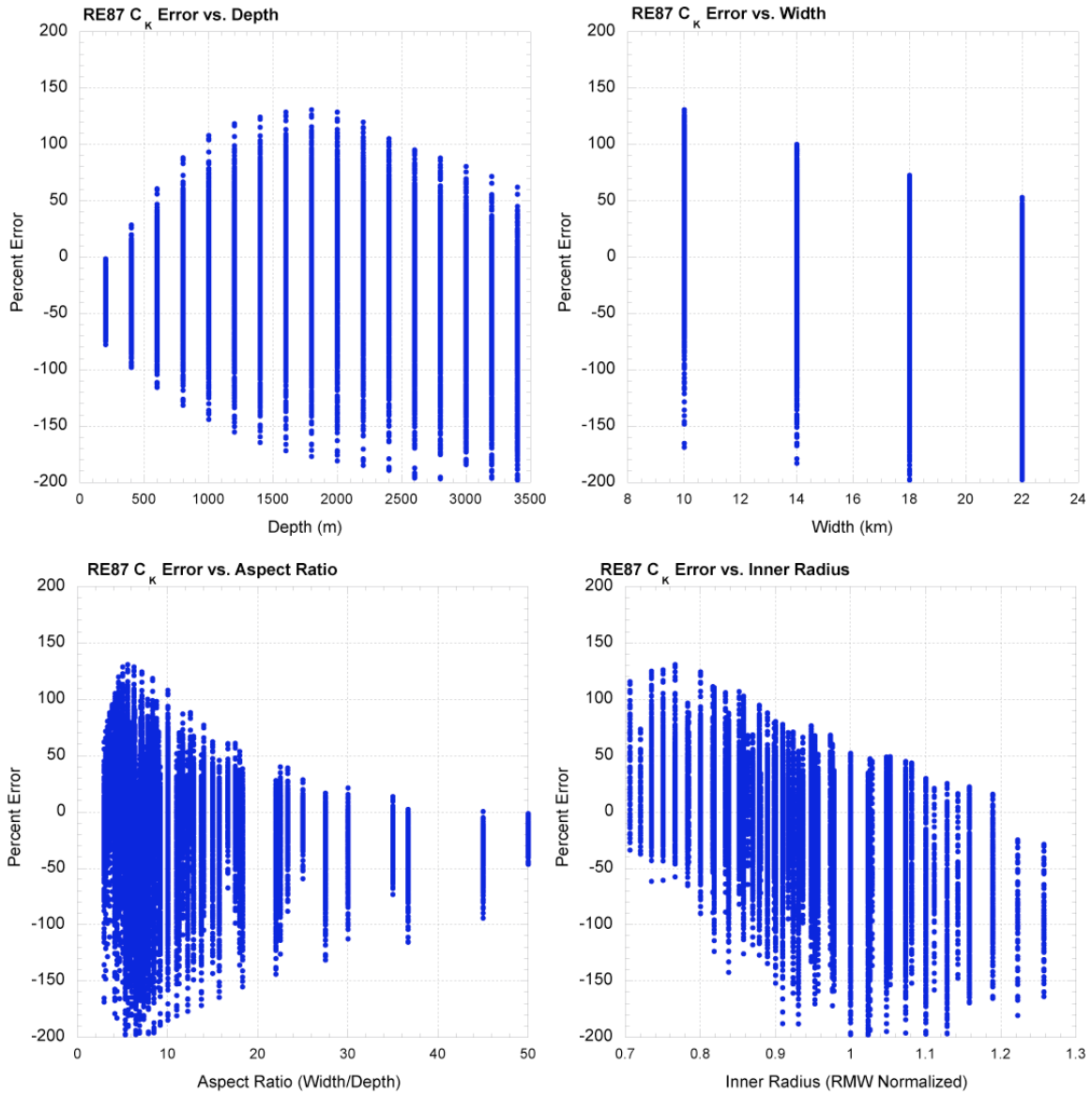
Figure 27.      RE87 $C_K$ sensitivity to control volume specification. Symbols and panels as in Figure 26, except for $C_K$.
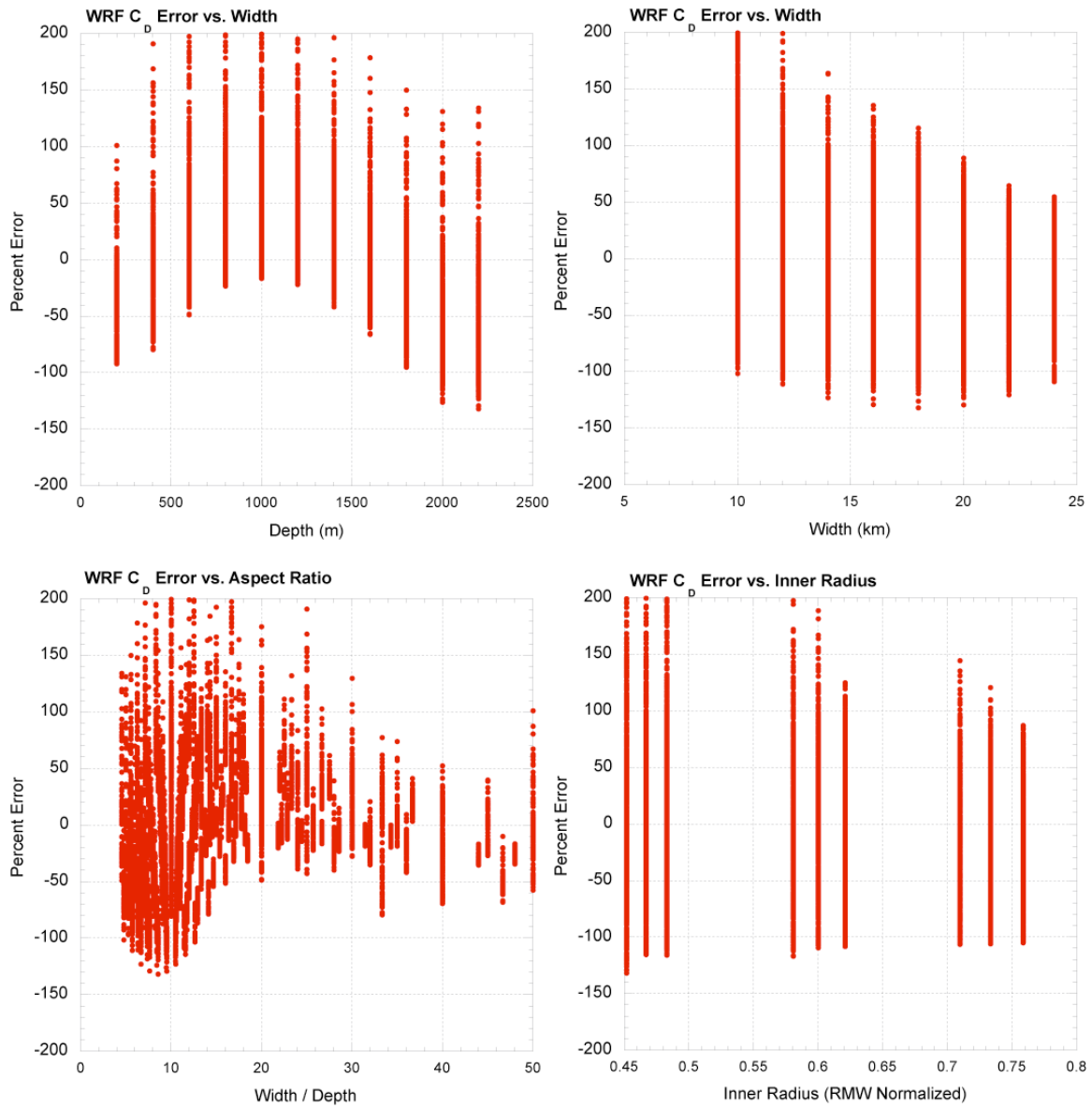
Figure 28.        WRF $C_D$ sensitivity to control volume specification. Symbols and panels as in Figure 26, except for WRF $C_D$.
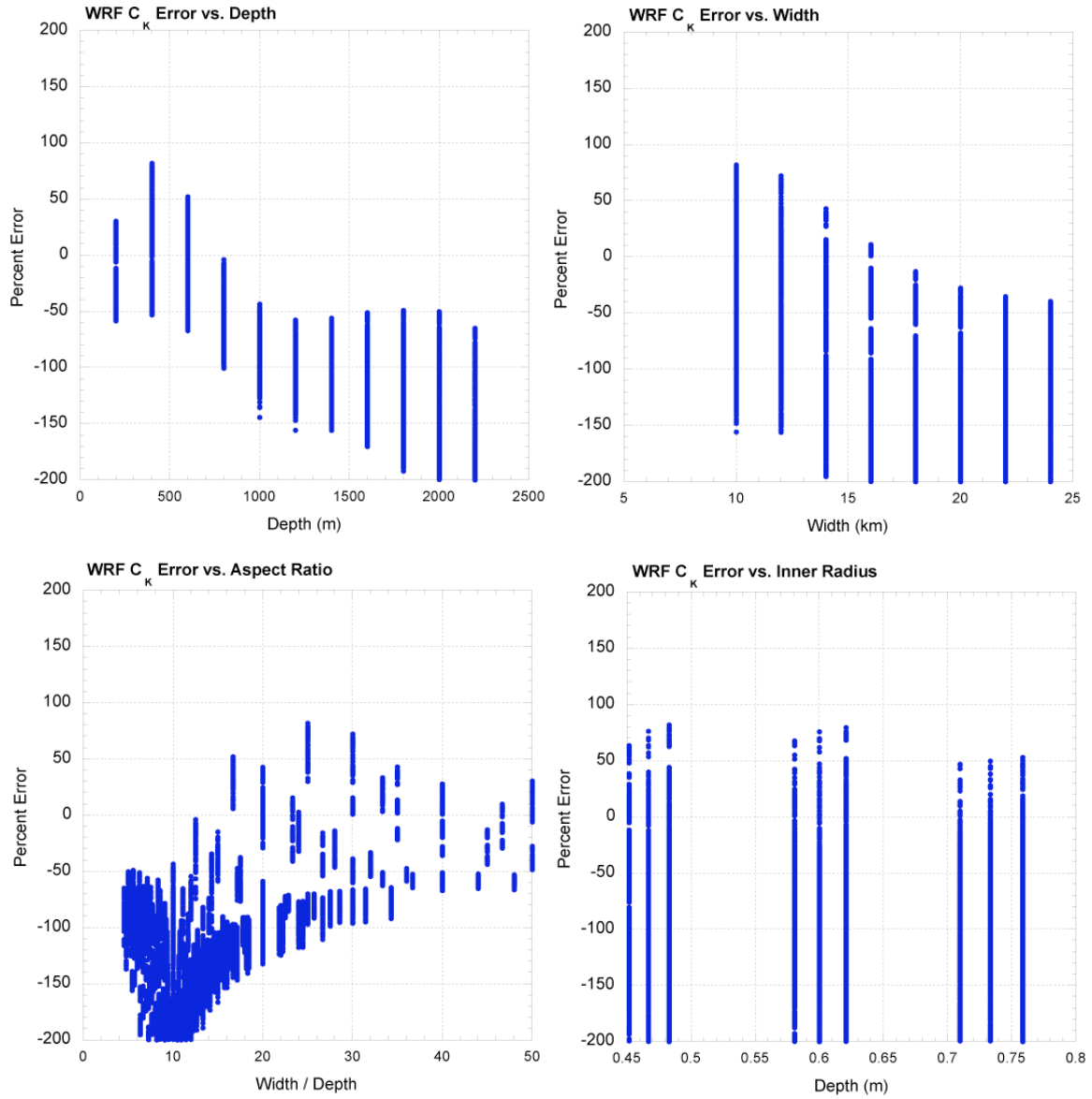
Figure 29.    WRF $C_K$ sensitivity to control volume specification. Symbols and panels as in Figure 26, except for WRF $C_K$.
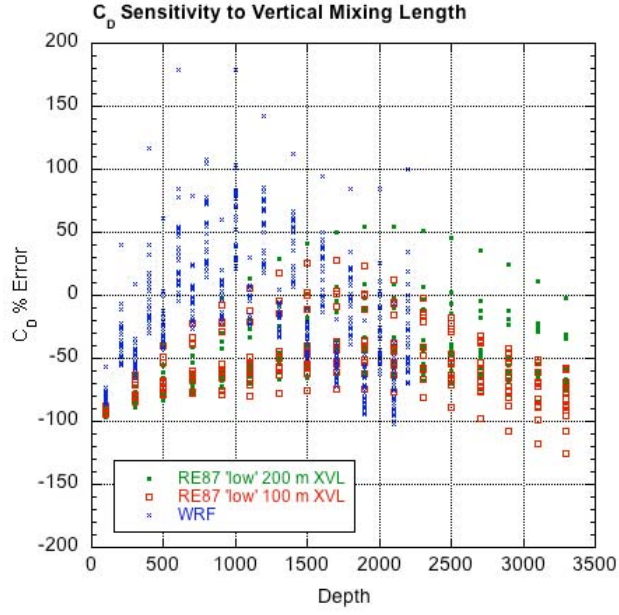
Figure 30.        Percentage error of $C_D$ versus control volume depth for RE87 "low" simulation using 200 m (green) and 100 m (red) vertical mixing length and WRF (blue).
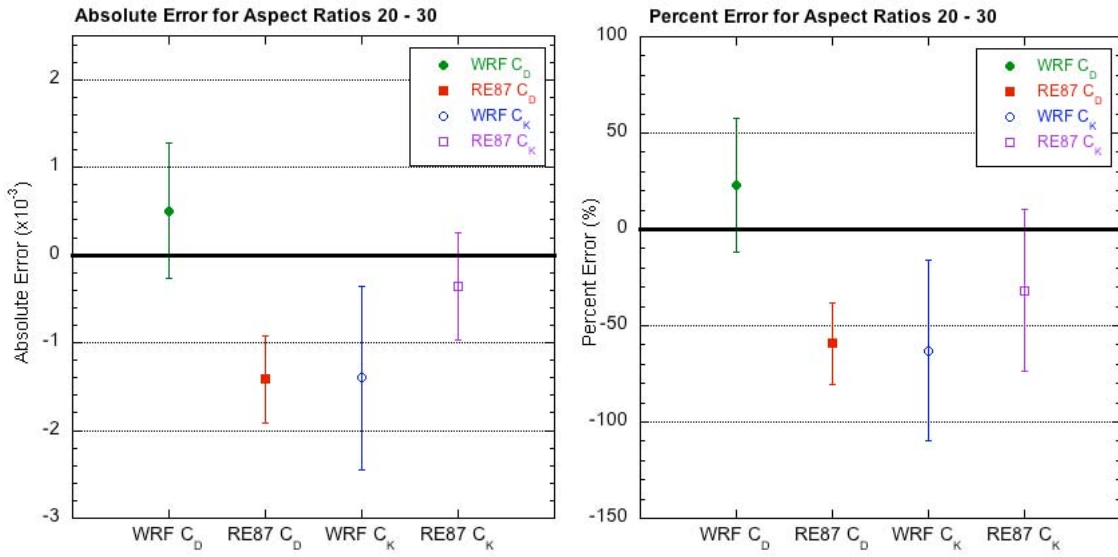


Figure 31.        (a) Absolute and (b) percentage mean bias and standard deviation for control volume aspect ratios of 20–30 for combined WRF and RE87 simulations (see inset).

Table 3.    Summary of estimated errors in budget retrieval. Error percentages are valid for $C_D$ values from 1.9–2.4 x$10^{-3}$ and $C_K$ values from 1.1–2.4 x$10^{-3}$.

| Error Source | Potential Error | Estimated Uncertainty | Mitigation |
|---|---|---|---|
| Mass continuity residual | >500% | 0 | Use streamfunction for analysis |
| Shear flux term | -60% | ±20% | Estimate term using derived $C_D$ |
| Other unresolved budget terms | ±200% | ±50% | Constrain control volume size |
| SST Errors | ~20% per 1° C error | ±20% | Use AXBT data when available |
| Center Errors | ±25% per km error for un-averaged analysis | ±20% | Use high-resolution radar circulation centers and averaging |
| Analysis Errors | Large with hand or objective analysis | ±20% | SAMURAI with 6x filtering |

# IV. SAMURAI ANALYSIS TECHNIQUE

Improvements in objective analysis techniques for gridding meteorological observations have been closely coupled to the increasing volume and variety of data sources used in NWP. The data assimilation problem, in which the best initial conditions for a weather forecast must be derived from sparse observations, is essentially identical to the analysis problem, in which the best estimate of the atmospheric structure must be derived to test scientific hypotheses. In both cases, the researcher or forecaster is attempting to determine the "true" state of the atmosphere from a limited set of observations that contain errors that result from sampling, instrumentation, representation, and inversion. An analysis that is used to produce a forecast also requires balance enforcement necessary to minimize oscillations of the primitive equations, versus a stricter adherence to the observations for purely diagnostic studies.

Early objective analysis techniques, such as those proposed by Cressman (1959) and Barnes (1973), emphasized the primacy of the observations by minimizing the difference between a gridpoint value and nearby observations weighted by their spatial distance. These well-tested algorithms still are commonly employed for diagnostic studies since they provide a simple, functional methodology for deriving gridded atmospheric structure from irregularly spaced data. These methods have been largely superseded within the NWP community by variational and Kalman filter techniques, which is motivated in part by the numerical balance requirements, but is also due to advancements in the application of probabilistic theory to the data assimilation problem. For the current study, these advancements are adopted within a mesoscale analysis framework in order to deduce the most probable axisymmetric TC state for momentum and energy budget calculations. The Spline Analysis at Mesoscale Utilizing Radar and Aircraft Instrumentation (SAMURAI) software program has been developed specifically for this study, with the goal of obtaining an objective analysis that can incorporate aircraft data and maximize the advantages of working within the axisymmetric, cylindrical geometry.

First, a variational (VAR) technique is derived from Bayesian first principles to determine the maximum likelihood estimate of the kinematic and thermodynamic structure. While 3D (or 2D in this case) VAR approaches are not new, the specific design of this implementation was chosen to provide an optimal framework for mesoscale analysis, and especially for tropical cyclones. Given the need for high-quality vortex and mesoscale analysis, particularly for initialization of numerical models, the SAMURAI software can be extended naturally into asymmetric cylindrical and Cartesian geometries in the future.

## A.    DERIVATION OF MAXIMUM LIKELIHOOD ESTIMATE

The derivation starts from a Bayesian approach following Lorenc (1986). Bayes' theorem states that the posterior probability of a state A, given that state B exists, is proportional to the prior probability of state A multiplied by the probability of state B if A exists. That is:

$$P(A \mid B) \propto P(B \mid A)P(A)$$

(4.1)

where state A is defined to be the correct estimate of the atmospheric state given some prior observation information. In this case, the analysis state vector $x$ is equivalent to the true state of the atmosphere $x_t$. The prior probability that this estimate is true is then

$$P(A) = P(x = x_t)$$

(4.2)

Since some error in this estimate is likely, this error is denoted by $x_\varepsilon = x_t - x$, and the spatial covariance of these "background errors" is then $\mathbf{B} = [x_\varepsilon x_\varepsilon^T]$. Here, the fundamental assumption is that the errors are unbiased and the probability distribution is Gaussian about the background estimate. This assumption can be justified by the expectation that the errors are random, as opposed to being systematic. The Central Limit Theorem for a continuous, multivariate system yields:

$$P(x = x_t) = \frac{1}{\sigma\sqrt{2\pi}} exp\left(-\frac{(x-\mu)^2}{2\sigma^2}\right) = \frac{1}{|\mathbf{B}|^{\frac{1}{2}}\sqrt{2\pi}} exp\left(-\frac{1}{2}(x_t - x_b)^T \mathbf{B}^{-1}(x_t - x_b)\right)$$

(4.3)

78

where $|\mathbf{B}|$ is the determinant of the covariance matrix equivalent to the standard deviation $\sigma$ in the univariate distribution, and $x_b$ is the background state estimate equivalent to the sample mean $\mu$. State B is then defined to be the state where the set of observations are obtained by sampling the (true) atmospheric state. That is, $P(\text{B}) = P(y = y_t \mid x = x_t)$. Assuming that perfect observations could be obtained by some forward model $h(x)$ that maps from the true state to observational space, then the error is denoted by $y_\varepsilon = y_t - h(x_t)$ and the covariance is $\mathbf{R} = [y_\varepsilon y_\varepsilon^T]$. These errors encompass instrument and representation errors. This distribution is again assumed to be unbiased and Gaussian which yields a similar probability distribution function:

$$P(y = y_t \mid x = x_t) = \frac{1}{|\mathbf{R}|^{\frac{1}{2}} \sqrt{2\pi}} exp\left( -\frac{1}{2}(y_t - h(x_t))^T \mathbf{R}^{-1}(y_t - h(x_t)) \right)$$

(4.4)

Given these two probability distributions, Bayes' rule is applied to derive the probability of the posterior distribution of state A given state B; e.g., the probability that the atmospheric state is correctly estimated given that measurements of the true state have been obtained. Substituting the PDFs into Bayes' rule yields

$$P(x = x_t \mid y = y_t) = C \cdot exp\left( -\frac{1}{2}(x_t - x_b)^T \mathbf{B}^{-1}(x_t - x_b) + (y_t - h(x_t))^T \mathbf{R}^{-1}(y_t - h(x_t)) \right)$$

(4.5)

where $C$ is a proportionality constant given by

$$C = \frac{P(B)}{\sqrt{2\pi}\,|\mathbf{R}|^{\frac{1}{2}}\,|\mathbf{B}|^{\frac{1}{2}}}$$

(4.6)

Taking the natural logarithm of both sides of (4.5) yields

$$\ln P(x = x_t \mid y = y_t) = \ln C - \left( \frac{1}{2}(x_t - x_b)^T \mathbf{B}^{-1}(x_t - x_b) + (y_t - h(x_t))^T \mathbf{R}^{-1}(y_t - h(x_t)) \right)$$

(4.7)

Thus, the probability that the atmospheric state has been correctly estimated is maximized when the variable term on the right side of Equation (4.7) is at a minimum.

Defining the term in parentheses on the right side of (4.7) as a cost function $J(x)$, and dropping the subscript $t$ for clarity, the maximum likelihood estimate (or identically, the minimum variance) is achieved when

$$
\min\{J(x)\} = \min\{J_b(x) + J_o(x)\} =
$$
$$
\min\left\{\frac{1}{2}(x - x_b)^T \mathbf{B}^{-1}(x - x_b) + (y - h(x))^T \mathbf{R}^{-1}(y - h(x))\right\}
$$

(4.8)

This minimization is achieved when

$$
\nabla J(x) = \mathbf{B}^{-1}(x - x_b) + \mathbf{H}^T \mathbf{R}^{-1}(y - h(x)) = 0
$$

(4.9)

where $\mathbf{H}^T$ is the linearized Jacobian matrix of $h(x)$. Note that if $h(x)$ is linear, the Bayesian solution is equivalent to the least-squares approach.

The form of the cost function in (4.8) and (4.9) is useful, but requires the storage and inversion of the background error covariance matrix. This is an $N \times N$ matrix, where $N = i \times j \times k \times n$ is the dimensional space of the analysis given by the product of the dimensions of the spatial vectors and number of variables. This inversion can be avoided by recasting this equation in an incremental form, which provides an improved structure for estimating the effects of this matrix without requiring its full storage (Courtier et al. 1994; Huang et al. 2000). Suppose that the maximum likelihood estimate can be obtained by an incremental update to the initial background estimate, such that

$$
x = x_b + \delta x
$$

(4.10)

Substituting (4.10) into the cost function (4.8):

$$
J(\delta x) = \frac{1}{2}(\delta x)^T \mathbf{B}^{-1}(\delta x) + (h(\delta x) - d)^T \mathbf{R}^{-1}(h(x) - d)
$$

(4.11)

where $d \equiv y - h(x_b)$ is termed the "innovation vector." To avoid having to invert $\mathbf{B}$, a symmetric matrix $\mathbf{C}$ is defined that has the same eigenvectors as $\mathbf{B}$ and eigenvalues of the square root of $\mathbf{B}$, such that $\mathbf{B} = \sqrt{\mathbf{B}}^T \sqrt{\mathbf{B}} = \mathbf{C}^T\mathbf{C}$ (Lorenc 1997). A control variable vector $q$ is defined as

$$q = \mathbf{C}^{-1}\delta x = \mathbf{C}^{-1}(x - x_b)$$

(4.12)

with the analysis increment in physical space recovered by

$$\delta x = \mathbf{C}q$$

(4.13)

Substituting (4.13) into (4.11) yields

$$J(q) = \frac{1}{2}q^T q + \frac{1}{2}(\mathbf{HC}q - d)^T \mathbf{R}^{-1}(\mathbf{HC}q - d)$$

(4.14)

in which the gradient is derived by differentiating (4.14) with respect to $q$:

$$\nabla J(q) = (\mathbf{I} + \mathbf{C}^T\mathbf{H}^T\mathbf{R}^{-1}\mathbf{HC})q - \mathbf{C}^T\mathbf{H}^T\mathbf{R}^{-1}d$$

(4.15)

This form not only avoids the inversion of **B**, but has several other benefits as well. The identity matrix in the first term of the cost function prevents the smallest eigenvalue of the Hessian matrix $\nabla^2 J$ from becoming less than unity. This form reduces the condition number of the Hessian, and suggests the conjugate gradient algorithm should converge faster than the form in (4.8) (Gao et al. 2004). More importantly, the control variable transform allows for the use of alternate internal state vectors in different coordinate systems. Since the maximum likelihood estimate is highly dependent on the specification of **B**, a form is desired in which the covariance is primarily determined by spatial correlations instead of cross-variable correlations. Thus, variables that are highly coupled (i.e., $u$ and $w$ in the tranverse vortex circulation) can be solved dependently through the use of a single variable (i.e., streamfunction). Likewise, coordinate or spectral transforms can be applied, which further serves to isolate the background errors by effectively diagonalizing the matrix. Lastly, since the background error covariance matrix is now applied in a forward manner, it can be treated as a linear operator that can be modeled by a simplified function, such as a Gaussian filter. This avoids the storage requirements of the $N \times N$ matrix. Specific choices related to **C** used in the SAMURAI technique will be described in the following section.

## B.    AXISYMMETRIC SAMURAI IMPLEMENTATION

The preceding general discussion is now refined for use with axisymmetric hurricane structure and available CBLAST observations. Recall that the probability distributions associated with the background and observation errors are assumed to be Gaussian and unbiased, and the inversion of **B** has been avoided by use of the incremental form of the cost function. However, some description of the **C** and the *h* operators and the control variables is still required. The background error correlations are assumed to be Gaussian and isotropic, which allows for an efficient recursive filter operator that replicates the effects of this correlation (Hayden and Purser 1995). For the solution to be the most effective, control variables are desired in which the analysis fields are smooth and well approximated by this spatial error correlation, which suggests the use of the following control variable state vector in cylindrical space:

$$q(r,z) = \{\rho r v, \psi, h', q_v', \rho_a'\}^T \tag{4.16}$$

where $\rho$ is the total density, $r$ is radius, $v$ is tangential wind, $\psi$ is the transverse streamfunction, $h$ is the saturated moist static energy given by $C_p T + L q_v + gz$, with $C_p$ the dry air heat capacity at constant pressure, $T$ the temperature, $L$ the latent heat of condensation, and $q_v$ the water vapor mixing ratio, $g$ is gravity, $\rho_a$ is the dry air density, and primes represent departures from a static, background reference state.  All of the relevant physical variables can be recovered from this distribution, and these quantities are expected to vary smoothly on the chosen grid. Note that $\rho r v$ is chosen instead of *v* for two reasons: first, to match the physical transform of the streamfunction into mass-weighted velocity components, simplifying the use of radar data by a uniform weight to the radial velocity; and second, to approximate the absolute angular momentum distribution in the inner core. Thus, the first three variables form the primary set for deducing the relevant physical quantities for use in the budget equations. The remaining two quantities are used to isolate the density from the mass-weighted wind components, and temperature from the moist static energy. The use of perturbation quantities allows

the analysis fields to avoid strong vertical gradients associated with the background hydrostatic pressure and water vapor distributions.

To convert the control vector $q$ from gridded variables on a physical grid to analysis increments, the background error covariance is formulated as an operator sequence of a cubic spline transform that is followed by a recursive Gaussian filter:

$$\mathbf{B} = \mathbf{C}^T\mathbf{C} = S_B^T S_A^T S_C^T S_C S_A S_B \tag{4.17}$$

where $S_B$ is a transform from the physical, Gaussian micro-mesh (hereafter referred to as the "mish") to a nodal representation, $S_A$ is a transform from the nodal representation to cubic spline coefficients, and $S_C$ is the recursive Gaussian filter and background error inflation. In matrix form,

$$\delta x = S_C S_A S_B q = \mathbf{DF(P+Q)^{-1}}\Phi q \tag{4.18}$$

This yields a set of spline coefficients in physical space that can be used to determine the atmospheric variables and their spatial derivatives anywhere in the domain. Each of these operators is examined in more detail below.

One of the fundamental aspects that distinguishes the SAMURAI analysis technique from other variational solvers is the use of a Galerkin approach, which is similar to the Fourier spectral transform, but uses the cubic B-spline as a basis (Ooyama 2002). This has the advantages that the interpolation coefficients for a function or its derivative at an arbitrary point on the grid can be easily calculated a priori for each observation or balance constraint, instead of maintaining a memory intensive gridpoint representation of complex interpolation coefficients and finite difference operators. Since the basis is cubic, it is computationally efficient and continuously differentiable to second order. The finite element representation allows for a flexible incorporation of boundary conditions, which is a distinct advantage over pure spectral techniques for non-periodic domains. The disadvantage of this basis is that it is not orthogonal, and thus requires a matrix inversion to obtain the spline coefficients, but this is a fair trade-off with its other desirable characteristics.

The spline transform (in one dimension) is given by:

$$\mathbf{a} = (\mathbf{P} + \mathbf{Q})^{-1} \mathbf{b}$$

(4.19)

where **a** is the state vector of spline coefficients and

$$u(r) = \sum_{m \in M} \phi_m(r) a_m$$

(4.20a)

$$\mathbf{b} = [b_m]^T, \qquad b_m = \int_D \phi_m(r) \breve{u}(r) dr$$

(4.20b)

$$\mathbf{P} = [p_{mm'}]^T, \qquad p_{mm'} = \int_D \phi_m(r) \phi_{m'}(r) dr$$

(4.20c)

$$\mathbf{Q} = [q_{mm'}]^T, \qquad q_{mm'} = \int_D \phi'''_m(r) \phi'''_{m'}(r) dr$$

(4.20d)

$$\phi_m(r) = \Phi\left(\frac{r - r_m}{\Delta r}\right), \quad \text{for } m \in M \text{ and } r \in D$$

(4.20e)

Here, $u(r)$ refers to a continuous representation of any variable, $\breve{u}(r)$ refers to the discrete given values of the variable (in this case, the control variables on the mish) and $\Phi$ refers to the cubic B-spline given by:

$$
\begin{cases}
\dfrac{1}{6}(1 - |\xi|)^3 - \dfrac{2}{3}(1 - |\xi|)^3 & \text{if } 1 \geq |\xi| \geq 0 \\[2mm]
\dfrac{1}{6}(2 - |\xi|)^3 & \text{if } 2 \geq |\xi| \geq 1 \\[2mm]
0 & \text{if } |\xi| \geq 2
\end{cases}
$$

(4.21)

The one-dimensional spline and its derivatives are shown in Figure 32. A third derivative constraint is incorporated into the $S_A$ transform (e.g., $(\mathbf{P} + \mathbf{Q})^{-1}$) to minimize Gibb's oscillations and spline representation errors near the Nyquist scale (2Δx). This also acts as a sharp, 6$^{th}$ order filter when used repeatedly as in the conjugate gradient minimization. For a regular $r,z$ grid, the inverse of $(\mathbf{P} + \mathbf{Q})^{-1}$ is precomputed via a Cholesky decomposition. Since the spacing of the internal control mish is arbitrary, the

integrations needed for $\mathbf{b}$ and $(\mathbf{P}+\mathbf{Q})^{-1}$ are done with a two-point Gaussian quadrature wherein the control gridpoints are chosen to be the quadrature points of the evenly spaced $r,z$ grid. Note that the $S_I$ transform (4.20a) is used in the $\mathbf{H}$ operator converting from spline coefficients to observation space. Homogenous or inhomogeneous boundary conditions can be incorporated easily into the transform by a direct modification of the spline coefficients near the edge of the domain. For this study, the second derivatives of all control variables were set to zero at the boundaries except for $\psi$ and $\rho rv$. The variable $\rho rv$ was set to zero at the axis of rotation ($r = 0$), and $\psi$ was set to zero at the axis of rotation and the surface ($z = 0$). The extension to two dimensions is straightforward, and more details on the cubic spline transform and the effect of the derivative constraint can be found in Hausman (2000) and Ooyama (2002).

The operator combination $S_C = \mathbf{DF}$ is the application of the background error covariance matrix, where $\mathbf{D}$ is the standard deviation of the background error and $\mathbf{F}$ is the recursive filter given by:

$$r_i = \beta p_i + \sum_{j=1}^{n} \alpha_j r_{i-j}$$

$$s_i = \beta r_i + \sum_{j=1}^{n} \alpha_j s_{i+j}$$

$$\beta = 1 - \sum_{j=1}^{n} \alpha_j$$

$$(4.22)$$

with $r$ and $s$ referred to as the advancing and backing steps of the filter. It can be shown that this filter approximates a second-order Gaussian filter with minimal computational cost. This formulation, which is derived in Purser et al. (2003), improves upon previous multi-pass filters by increasing the order $(n)$ of the approximation so that only a single forward and backward pass is required. Analytic results suggest that fourth order is sufficient for most applications.

The resulting state vector after the sequence of transforms is the set of spline coefficients for the state vector increments on the physical radius grid. Lastly, the

variables need to be mapped to observational space. This is done using the two-dimensional form of the cubic spline:

$$x(r,z) = \sum_{n \in N} \sum_{m \in M} \phi_m(r)\phi_n(z)a_{mn}$$

(4.23)

Note that the summation occurs only over a few nodes near the physical point in practice, due to the finite basis representation. The basis function is replaced by the derivatives of $\phi_m$ for the streamfunction to convert to physical variables:

$$\rho r u(r,z) = \sum_{n \in N} \sum_{m \in M} -\phi_m(r)\phi_n'(z)\psi_{mn}$$

$$\rho r w(r,z) = \sum_{n \in N} \sum_{m \in M} \phi_m'(r)\phi_n(z)\psi_{mn}$$

(4.24)

For aircraft and dropsonde observations, the direct measurements of thermodynamic scalars $T$, $p$, and relative humidity are transformed to $h'$, $q_v$, and $\rho'_a$ in the initialization to simplify the minimization. Cartesian wind velocities are then transformed into their cylindrical projections by:

$$\rho u = \rho((\tilde{u} - U_m)x + (\tilde{v} - V_m)y)/r$$

$$\rho v = \rho((\tilde{u} - U_m)y - (\tilde{v} - V_m)x)/r$$

$$\rho w = \rho \tilde{w}$$

(4.25)

where tilde variables are Cartesian wind components, $x$ and $y$ are Cartesian distances to the storm center, and $r$ is the radius to the storm center, which is moving at $(U_m, V_m)$. Radar data requires the projection of the analysis variables given the following transforms:

$$\rho u \left[ (x\sin(\theta)\cos(\gamma) + y\cos(\theta)\cos(\gamma))/r \right] +$$

$$\rho v \left[ x\cos(\theta)\cos(\gamma) - y\sin(\theta)\cos(\gamma))/r \right] +$$

$$\rho w \left[ \sin(\gamma) \right] = \rho \hat{V}_D$$

$$\hat{V}_D = V_D - w_t \sin(\theta) - U_m \sin(\theta)\cos(\gamma) - V_m \cos(\theta)\cos(\gamma)$$

(4.26)

where $\theta$ and $\gamma$ are the radar beam azimuth and elevation, $V_D$ is the observed Doppler velocity, and $w_t$ is the estimated terminal fall speed of the precipitation derived from the

reflectivity. The Joss and Waldvogel (1971) reflectivity/rain relationship $w_t^{rain} = -2.6 \hat{\rho} Z^{.107}$ is used below the melting level, where $\hat{\rho}$ is a density correction (Beard 1985) and $Z$ is the linear reflectivity. For this study, the top of the analysis domain was restricted to 2.5 km such that the rain relationship was used exclusively, but an ice/snow relationship (Atlas et al. 1973) also was coded for use in other applications.

SAMURAI was coded in C++ with the cost function minimization performed by a conjugate gradient algorithm (Press et al. 2002). Several critical loops were parallelized using openMP to accelerate convergence, with identical results to serial execution. For the current study, the radial nodal resolution was set to 1 km, with a vertical resolution of 100 m. After some experimentation, a 6Δx length-scale (6 km radial and 600 m vertical) was chosen for the recursive filter, and a 4Δx scale length was chosen for the third derivative constraint. This defined the approximate spatial influence of a single observation as 6Δx and damped the amplitude of spectral features less than 4 times the grid spacing, with both operators effectively acting as diffusive, low-pass filters.

Single observation tests using synthetic observations were performed to test and debug the C++ code. An example of the analysis increment using a single Doppler radar observation is shown in Figure 33. The instrumentation error of this test observation was set very low to induce a substantial analysis increment for illustrative purposes. Since the Doppler velocity contains information about all three components of motion, a Gaussian shaped response in the tangential velocity and streamfunction results. The analysis of a single Doppler velocity observation is underdetermined in a traditional objective analysis scheme, but in the variational formulation the specified background field provides the additional constraints needed to produce a full wind field. The use of the streamfunction as the control variable induces a toroidal circulation around the observation to conserve mass. When multiple observations are included, the result is the maximum likelihood estimate that satisfies the Bayesian probability derived from the error characteristics of the observations and background analysis. The background error estimates were set liberally to allow strong adherence to the observations and limited dependence on the background field. To ensure the results

were not overly sensitive to the specified background, a second "outer loop" minimization was performed using the results of the first cost function minimization as an updated background field. The specified background errors are shown in Table 1. The tangential wind, mass, and vapor mixing ratio fields from the Barnes analysis in BM08 were used for the Isabel analysis, with simple, analytic fields for Fabian. In all cases, the transverse streamfunction background field was set to zero.

Though the error characteristics of the specific aircraft instrumentation used in this study are well known, the representation errors arising from the use of an axisymmetric coordinate system are not. Aircraft observations were first pre-processed into a moving, storm-relative, cylindrical coordinate system, such that the estimated observation errors were a combination of errors in both the instrumentation and representativeness in 2D-cylindrical space. A full description of the instrumentation and observation errors is given in Chapter V.
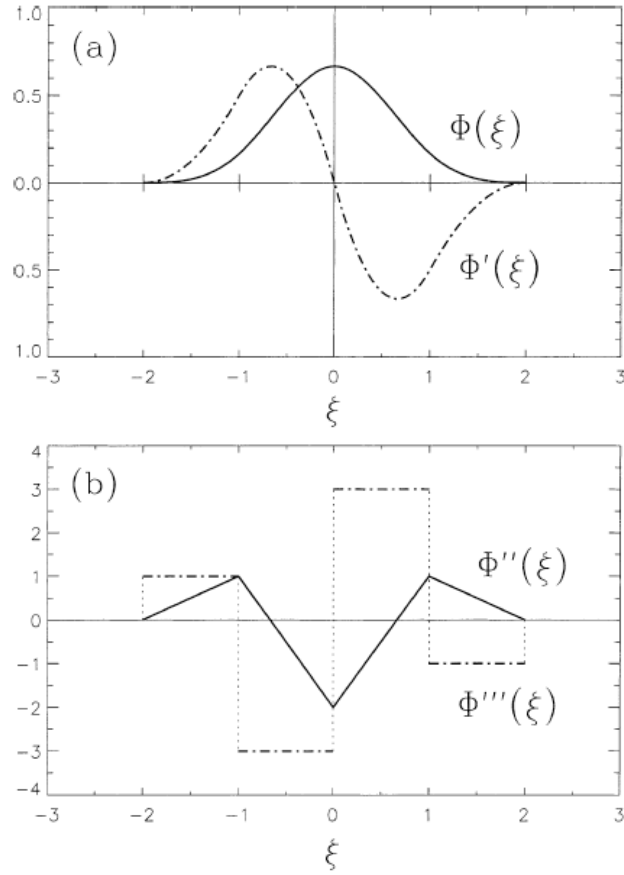
Figure 32.      (a) The cubic B-spline $\Phi$ on the normalized abscissa $\xi$ and its first derivative $\Phi$'; (b) the second and third derivatives. From Ooyama (2002)
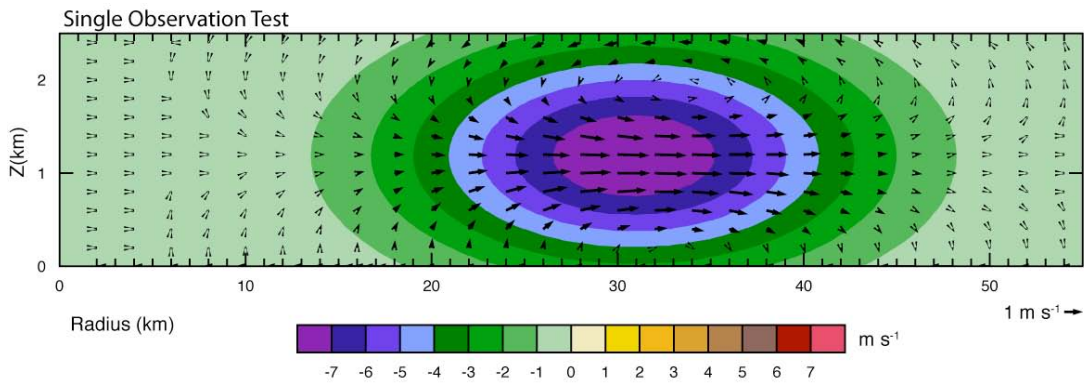


Figure 33.      Single radar observation analysis increment from background state. Color indicates increment in tangential wind, and vectors indicate the increment in the secondary circulation.

THIS PAGE INTENTIONALLY LEFT BLANK

# V. RESULTS

## A. CBLAST DATASET

Six intensive observing periods (IOPs) were conduction in Hurricane Fabian from 2–4 September, and in Hurricane Isabel from 12–14 September, 2003 as part of the CBLAST and NOAA/NESDIS OCEAN WINDS experiments. National Hurricane Center (NHC) best-track intensities were estimated at greater than 120 kt during the ~16–23 UTC time period in which observations were collected in Fabian (Figure 34) and Isabel (Figure 35), which makes both storms major hurricanes on the Saffir-Simpson scale during the six IOPs. Two NOAA WP-3Ds (P3s), the NOAA G-IV, and United States Air Force (USAF) C130 aircraft collected in situ flight-level and dropwindsonde observations, with additional Doppler radar and radiometer data obtained by the P3s only. The dataset is similar to that used in Montgomery et al. (2006), Bell (2006), and Bell and Montgomery (2008), but with the additional use of the University of Massachusetts stepped frequency microwave radiometer (SFMR) and Doppler radar in the axisymmetric composites, and the addition of the Fabian observations.

Flight-level observations at one Hz resolution from the NOAA 42 aircraft used in this study were kindly provided by the NOAA Hurricane Research Division. A rudimentary correction for instrument wetting errors (Zipser et al. 1981; Eastin et al. 2002) was applied to supersaturated dewpoint temperature measurements. This correction assumes that the errors for the temperature and humidity sensors are equal in magnitude but opposite in sign, which was shown by Eastin et al. (2002) to reduce the majority of significant wetting errors but not completely remove the errors.

National Center for Atmospheric Research (NCAR) Global Positioning System (GPS) dropwindsondes measure pressure, temperature, relative humidity (PTH), and horizontal wind speed at two Hz temporal resolution along a Lagrangian trajectory as the sondes fall at 12-15 m s$^{-1}$ in the lower troposphere. This yields a vertical resolution of approximately 5 m. The PTH typical errors are less than 1.0 hPa, 0.2 C, and 5% respectively, and the wind errors are less than 2.0 m s$^{-1}$ (Hock and Franklin 1999).

Vertical velocity was derived by removing the estimated terminal fallspeed of the sondes as a function of pressure (Wang et al. 2009). All dropsondes were quality-controlled to remove noise and other instrument errors with the HRD Editsonde software. Bell (2006) provides an in-depth discussion of the dropsonde data from the CBLAST experiment, including issues related to humidity corrections for some of the data.

The X-band (3.2 cm) wavelength tail Doppler radar employed the fore/aft scanning technique for all missions, which provided radial velocity data in a cone ~20 from the track both fore and aft of the aircraft. The data were first corrected for navigational errors and manually edited to remove ocean returns, radar sidelobes, and other artifacts (Oye et al. 1995; Testud et al. 1995; Bosart et al. 2002). A large number of radial penetrations were edited for the current study, which included all of the multiple dropsonde sequences. The times of the edited radar data used in the analysis are shown in Table 4. Most of these legs were used for circulation center fixes, but some were too short to obtain meaningful results from the simplex search algorithm. One of the more challenging aspects of utilizing this radar dataset was the velocity ambiguity resulting from the use of a low Nyquist velocity during most of the flights. With unambiguous radial velocities of <20 m s$^{-1}$, the Doppler information frequently was "folded" multiple times in conjunction with the very strong winds in the major hurricane eyewalls. The Bargen and Brown (1980) algorithm was used to correctly dealias the majority of the velocities using the in situ aircraft flight-level wind as a reference point, but gaps and noise in the data made additional manual unfolding of many rays necessary. An iterative correction was made for poorly dealiased velocities evident in the dual-Doppler wind fields used for center finding. While some of the individual radar gates still may contain dealiasing errors due to the multiple folds in high gradient areas, they are not likely to affect the analysis winds significantly, given the large number of observations and averaging.

The along-track resolution of the radar scans was ~1.5 km, with a 75-m range resolution along the beam and 1.9 degree beamwidth. In an effort to: (1) provide more uniform spatial resolution; (2) reduce errors associated with individual gates; and (3) thin the voluminous dataset for the variational analysis, the radial velocities were averaged

along each beam over a minimum of five gates that increased in number with range as the beam spread. This averaging reduced the radial resolution to approximately the diameter of the beam, and decreased the number of observations by nearly an order of magnitude. The error was determined from two contributions: (1) the spectrum width of the radial velocity measurements, which represents the variance of the velocity within the pulse volume (Keeler and Ellis 2000); and (2) the estimated error in the terminal fall speed. The sum of these two sources with a minimum value of 2 m s$^{-1}$ was used for the error estimate.

The University of Massachusetts deployed a SFMR for measuring surface wind speed and rain rate on the NOAA-42 aircraft. This C-band (~5 cm) wavelength, downward-pointing radiometer relates brightness temperatures at six different frequencies to surface emissivity and to empirically derived wind speeds. Since wind speed is a nonlinear observation operator, it was assumed here that the tangential velocity comprised the majority of the retrieved wind speed. If the surface inflow angle is less than 30 degrees, then the error caused by this assumption is no more than ~12%. Given uncertainties in the calibration of the instrument and the simplification of the observation operator, the observation error was set to a relatively high value of 10 m s$^{-1}$. Nevertheless, these SFMR wind speed observations provided an important constraint on the surface wind speed when near-surface dropsonde winds were not available.

The combined instrument and representativeness errors for the observations used in this study are shown in Table 5. While there are likely some larger errors associated with individual measurements, these values are believed to be statistically accurate for the bulk of the observations. The analysis composites were not found to be strongly sensitive to the magnitude of the prescribed errors, but did exhibit a general trend toward smoother fields as the instrument error values were increased. If the errors were set too small, then the fields exhibited a tendency toward over-fitting, with a lower root mean square difference between the observations and analysis, but an unrealistic level of detail.

Figure 34.    NOAA Tropical Prediction Center/National Hurricane Center (a) best track and (b) best track intensity for Hurricane Fabian. The three intensive observing periods on 2, 3, and 4 September are highlighted in panel (b).

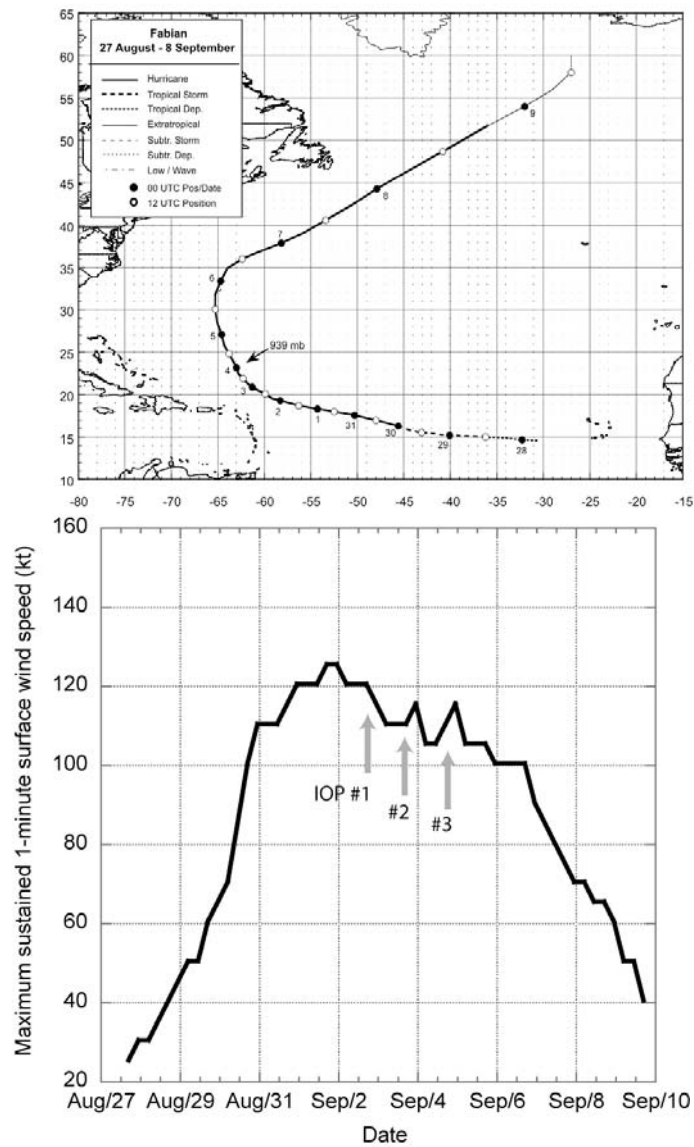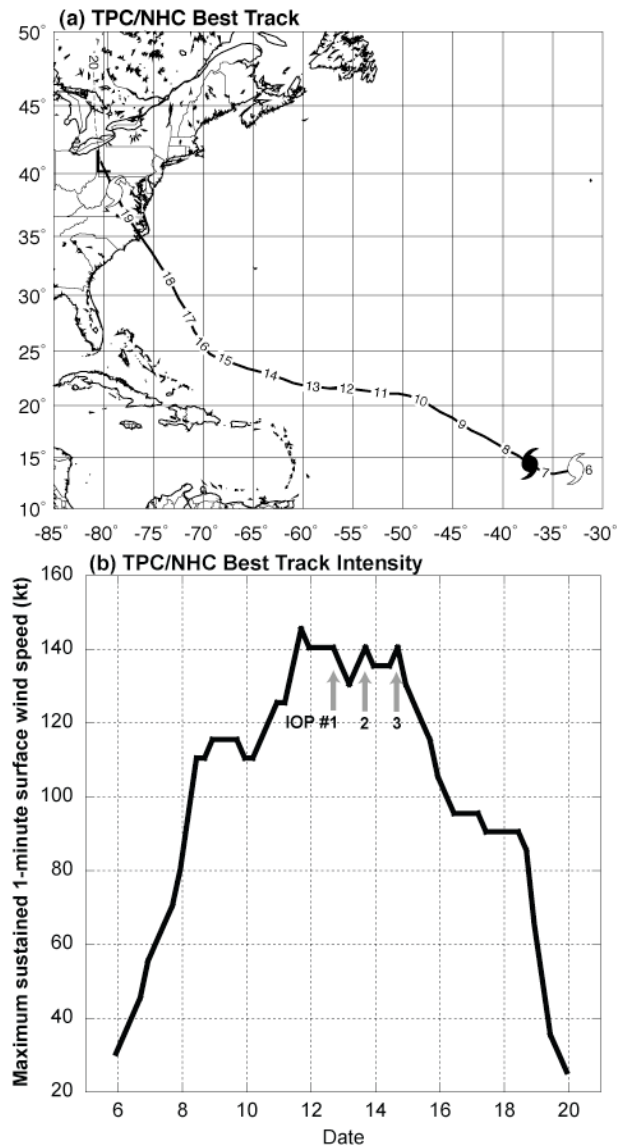Figure 35.    NOAA Tropical Prediction Center/National Hurricane Center (a) best track and (b) best track intensity for Hurricane Isabel. Open hurricane symbol indicates transition to tropical storm strength, filled symbol indicates transition to hurricane strength, and "L" indicates extratropical transition. The three intensive observing periods on 12, 13, and 14 September are highlighted in panel (b).

Table 4. Analysis times for edited Doppler radar data for Fabian during 2 – 4 September and Isabel 12 – 14 September (all times UTC).

| Fabian 02 | Fabian 03 | Fabian 04 | Isabel 12 | Isabel 13 | Isabel 14 |
|---|---|---|---|---|---|
| 1712-1726 | 1704-1714 | 1930-1949 | 1650-1659 | 1620-1642 | 1618-1646 |
| 1930-1941 | 1839-1849 | 2020-2035 | 1721-1726 | 1653-1709 | 1716-1730 |
| 1953-2002 | 1849-1857 | 2120-2139 | 1828-1846 | 1726-1742 | 1816-1830 |
| 2014-2027 | 1929-1939 | 2143-2159 | 1901-1910 | 1748-1807 | 1849-1902 |
| 2101-2114 | 1940-1950 | 2203-2219 | 1943-1948 | 1820-1841 | 1906-1919 |
| 2115-2123 | 2010-2020 | 2234-2250 | 2006-2019 | 1859-1913 | 1936-1947 |
| 2206-2219 | 2100-2110 | | 2024-2036 | 1916-1930 | 1953-2009 |
| 2223-2235 | 2114-2124 | | 2038-2049 | 1936-1950 | 2013-2029 |
| 2244-2252 | 2204-2211 | | 2115-2130 | 1953-2007 | 2035-2050 |
| | | | | 2026-2039 | 2052-2111 |
| | | | | 2043-2055 | 2112-2125 |
| | | | | 2102-2117 | 2130-2147 |
| | | | | | 2151-2207 |
| | | | | | 2209-2225 |

Table 5. Combined instrumentation and representativeness errors used in the SAMURAI composites.

| Instrument (Type) | $\rho u$ error | $\rho v$ error | $\rho w$ error | $q'$ error | $\rho'$ error | $h'$ error |
|---|---|---|---|---|---|---|
| Dropsonde (0) | 2 kg m$^{-2}$ s$^{-1}$ | 2 kg m$^{-2}$ s$^{-1}$ | 4 kg m$^{-2}$ s$^{-1}$ | 2 g kg$^{-1}$ | 10 g m$^{-3}$ | 5 kJ |
| Flight level (1) | 2 kg m$^{-2}$ s$^{-1}$ | 2 kg m$^{-2}$ s$^{-1}$ | 2 kg m$^{-2}$ s$^{-1}$ | 2 g kg$^{-1}$ | 10 g/m$^{-3}$ | 5 kJ |
| Doppler Radar (2) | Min($\sigma$+ 2*sin($\phi$), 2.0) kg m$^{-2}$ s$^{-1}$ | | | | | |
| SFMR (3) | | 10 kg m$^{-2}$ s$^{-1}$ | | | | |

## B. DERIVED STORM STRUCTURES

SAMURAI analyses were conducted for the six CBLAST missions using the data sources, error characteristics, and circulation centers described above. The radar and non-radar observation data distribution for the 2 September mission is shown in Figure 36 in both the radius-height and polar planes. It is clear that the radar data dominates the spatial distribution due to the wide swath of the tail Doppler radar. Comprehensive radar coverage provides good confidence in the kinematic fields throughout the domain, except near the eye where scatterers are limited. Excellent dropsonde coverage is also obtained in the main eyewall region near the RMW, with bracketing observations at flight level and at the surface from the SFMR. Good azimuthal sampling was achieved by the multiple sequences across the eyewall. Since only the flight level and dropsonde data provide thermodynamic data, the highest quality energy analysis is restricted to the ~20–50-km annulus. Note that the closed energy contours at the outer radii (> ~50 km radius) are likely artifacts from the lack of data in these regions, where the analysis relaxes back to the prescribed background state. Similarly, the thermodynamic structure inside of 20-km radius may be unreliable due to a data void region. Control volumes were not extended to these regions due to lack of confidence in the thermodynamic analysis outside of the main dropsonde sequences. However, the analysis was extended to the storm center and just beyond the main dropsonde sequence locations to avoid issues with the prescribed boundary conditions.

A large number of observations was incorporated into the analysis composites. A total of ~711,050 observations of a kinematic or thermodynamic variable were included in the 2 September analysis, with the largest number coming from the radar data. A bar chart showing the relative contributions of each instrument type for this mission is shown in Figure 37. Nearly 600,000 Doppler radar velocities were included, with the second largest contribution coming from dropsondes at ~100,000. Flight level and SFMR observations were more limited due to their single altitude sampling. One of the advantages of the variational analysis is the ability to effectively combine these observations based on their individual error characteristics. The statistical comparison of the observations versus the analysis at the measurement location is shown in Figure 38.

The correlation is greater than 0.99, with a linear fit having only a small intercept bias and slope near 1. The spread of the difference between the observations and analysis is nearly uniform at different magnitudes. The units of the observations are m s$^{-1}$ for kinematic variables, g kg$^{-1}$ for water vapor, kJ for moist static energy perturbation, and 10 g m$^{-3}$ for density. Since all of these variables have similar magnitudes in these units, the statistics are not dominated by any particular measurement.

The prescribed background and observation errors and smoothing parameters control the amount of spread from the one-to-one centerline. The distribution of the differences is shown in Figure 38b, and illustrate an approximately normal distribution centered about zero, which is consistent with the uniform scatterplot in panel a. The large number of observations ensures that any single poor measurement will not bias the analysis significantly, and that the majority of the differences are within the combined observational error and variability of the three-dimensional observations in representing the axisymmetric mean. These statistics suggest a good fidelity of the analysis to the observations without excessive over-fitting.

The data distributions of non-radar observations for the remainder of the missions are shown in Figures 39–43. Radar sampling was similar on all days to the first mission and is not shown. The dropsonde distributions are similar to the first mission, with the exception of little data outside of 40-km radius but excellent azimuthal sampling on 3 September, and limited azimuthal sampling on 4 September. All of the Isabel missions are characterized by comprehensive radial and azimuthal sampling. Note that distributions are slightly different from those shown in BM08 due to the use of radar-derived circulation centers instead of flight-level winds as described in Chapter III, but the patterns are qualitatively the same.

The derived wind fields for Hurricane Fabian are shown in Figure 44. The tangential winds depict a general weakening over the three analysis days, with a decrease in the depth of the strongest winds and slow weakening of the maximum tangential wind by the third day. The reduction in the depth and intensity of the tangential wind was concurrent with a reduction in the inflow depth and magnitude over the three days. The primary updraft also appears to have weakened during these three days. The RMW

remained consistently just inside 30-km radius, with a sharp gradient of tangential wind towards the center. Note that the low-level inflow continues past the RMW on all three analysis days, with the flow turning upwards near the high tangential wind gradient region. The absolute angular momentum and total energy are shown in Figure 45. The secondary circulation generally follows the contours of angular momentum above the inflow layer, with more tilted angular momentum surfaces outside the RMW on the second and third days. The energy contours also depict a toroidal shape that is similar to, but not congruent with, the momentum contours and secondary circulation. A reduced radial energy gradient is apparent on each consecutive day, which is consistent with the weakening trend in the kinematic variables. The oppositely directed gradients of momentum and energy are similar to those found in the numerical simulations in Chapter III.E, but the specific magnitudes and structures of the energy are notably different from the RE87 and WRF simulations.

The analyzed kinematic fields for Hurricane Isabel for all three missions are shown in Figure 46. Note that the inner radius shown is 15 km for clarity due to the larger domain, although the analysis domain was extended to the TC center. The qualitative features of the SAMURAI analysis are similar to the Barnes analysis used in BM08, but with enforced mass continuity of the secondary circulation and a notably sharper resolution of the boundary layer inflow. The characteristic "over-shoot" of the inflow past the RMW is apparent during all three missions as was the case in the Fabian analysis, with a sloping inflow top that coincides with the height of the maximum tangential wind. A gradual weakening and expansion of the tangential wind as described in BM08 is evident, with a well-defined outflow and updraft core just above the maximum tangential wind on all three days. The angular momentum and energy analyses are shown in Figure 47. The consistent structure of the secondary circulation, momentum, and energy contours is similar to in the analyses for Fabian. The total energy structure is also qualitatively similar to the moist entropy structure shown by BM08 (c.f., their Figure 5), as would be expected by their similar thermodynamic variables.

The kinematic and thermodynamic structures apparent in the six analyses are consistent in their depiction of gradually weakening storms just past their peak intensity.

Differences exist in the evolution of the RMW, with Isabel expanding while Fabian remained nearly constant, and in their respective intensities. These six missions make an excellent dataset for the flux retrievals, since they are all nearly steady state, span approximately 20 m s$^{-1}$ in their peak tangential wind speeds, and have a variety of different inflow depths and magnitudes.

The analysis statistics for all six missions are listed in Table 6. The number of observations varies from ~500,000 to more than 1.7 million on 14 September (due to the large domain required to encompass the 45 km RMW), with comparable differences between the analyses and observations on all days. Similar minimum and maximum differences, low skewness, and kurtosis values near 3 suggest nearly normal distributions. One exception to this statement is found on 13 September, where the high kurtosis and larger peak differences are most likely attributed to some faulty velocity dealiasing, but the low mean, RMS, and standard deviation of the differences suggest these are isolated errors. Linear correlations are near 0.99 for all days, with low intercept and slope values near one (not shown) for all distributions. These statistics suggest that the SAMURAI analyses are indeed maximum likelihood estimates for the TC structures in areas of sufficient data density. Since there are no high confidence a priori estimates of the structure available, other than the previous Barnes analysis with the same dataset, the data is only weakly constrained in poor data regions. Fortunately, the rich data regions encompass the areas required to obtain optimal aspect ratios of 20–30 for the control volumes.
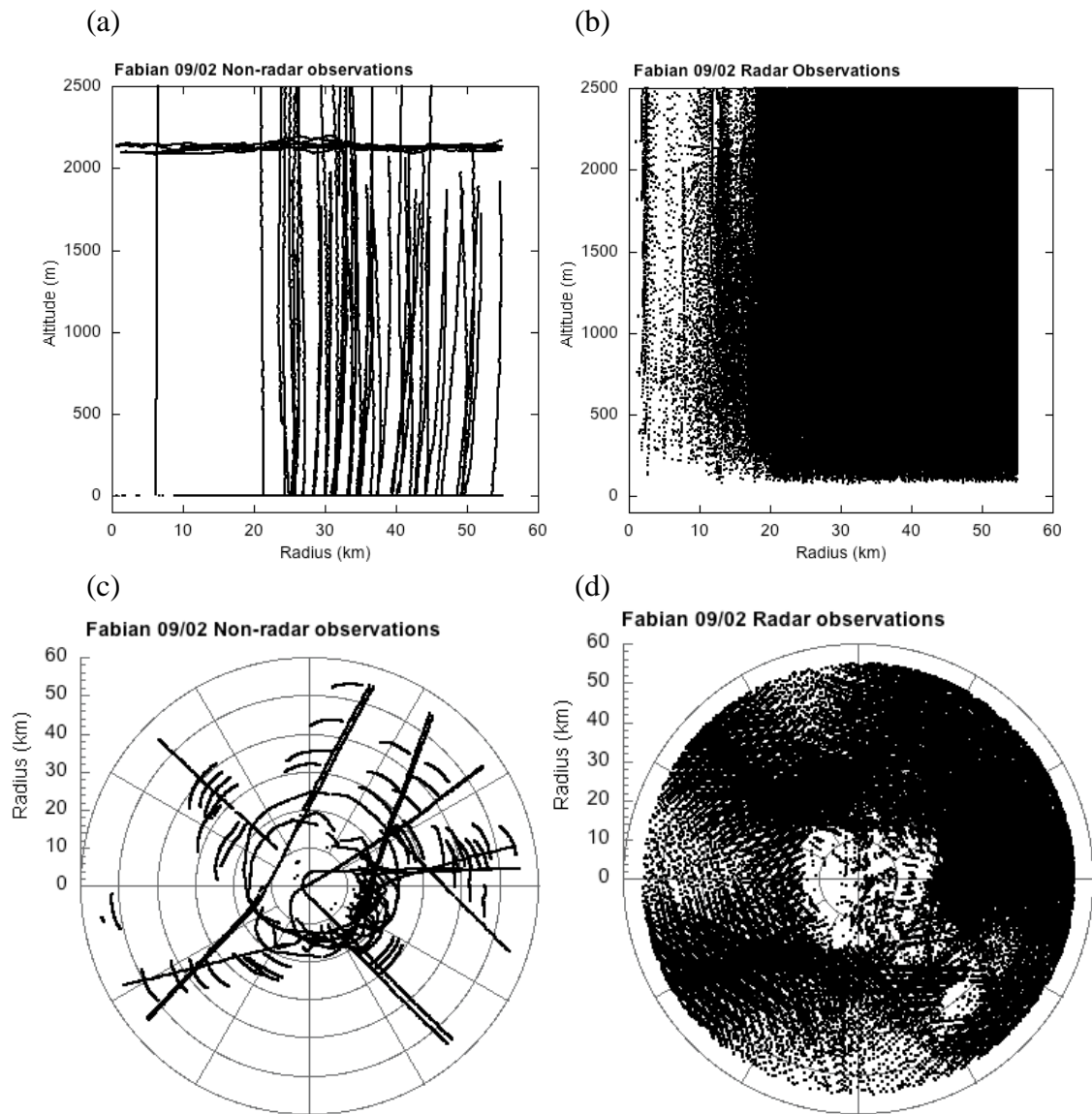
Figure 36.    Spatial distribution of observations on 2 September. (a) Non-radar and (b) radar observations in the radius-height plane. (c) Non-radar and (d) radar observations in the radius-theta plane.
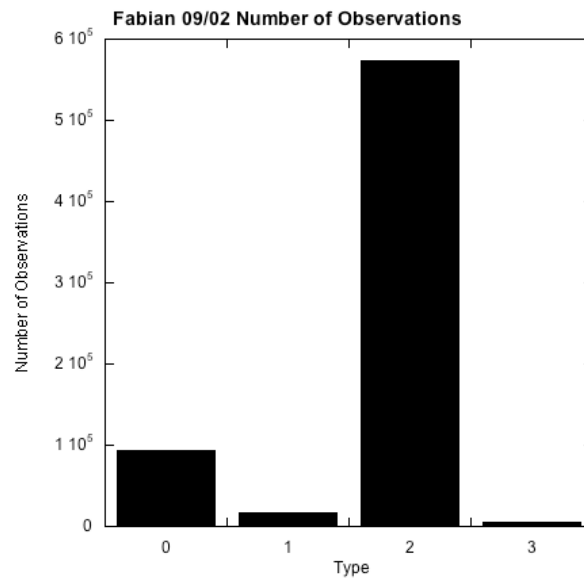
Figure 37.    Number of observations on 2 September for each instrument. Instrument types are given in Table 2.

(a)                                                (b)
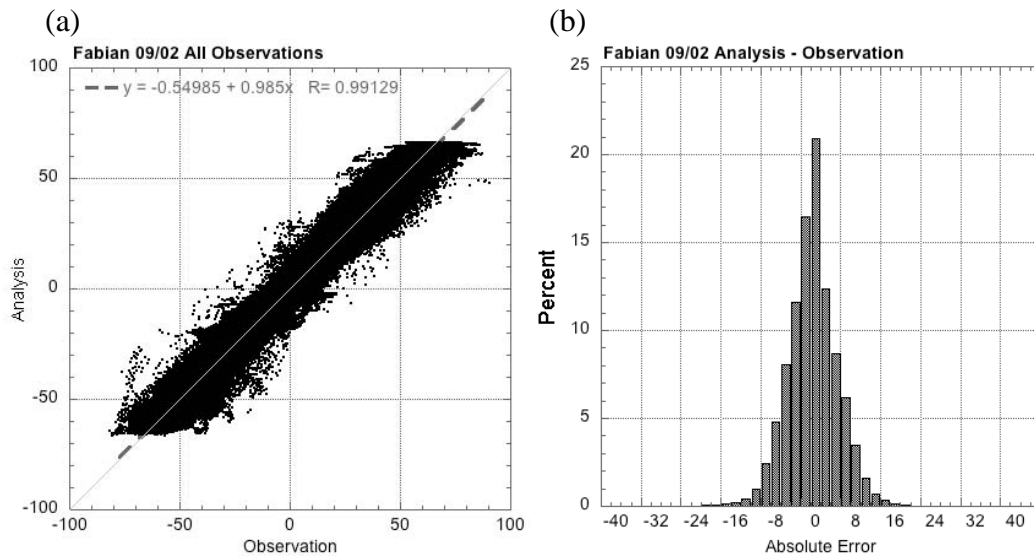


Figure 38.    Analysis versus observations for Hurricane Fabian on 2 September. (a) Scatterplot of all observations and (b) histogram of differences between observations and analysis. Units of each observation are the same as in Table 5.
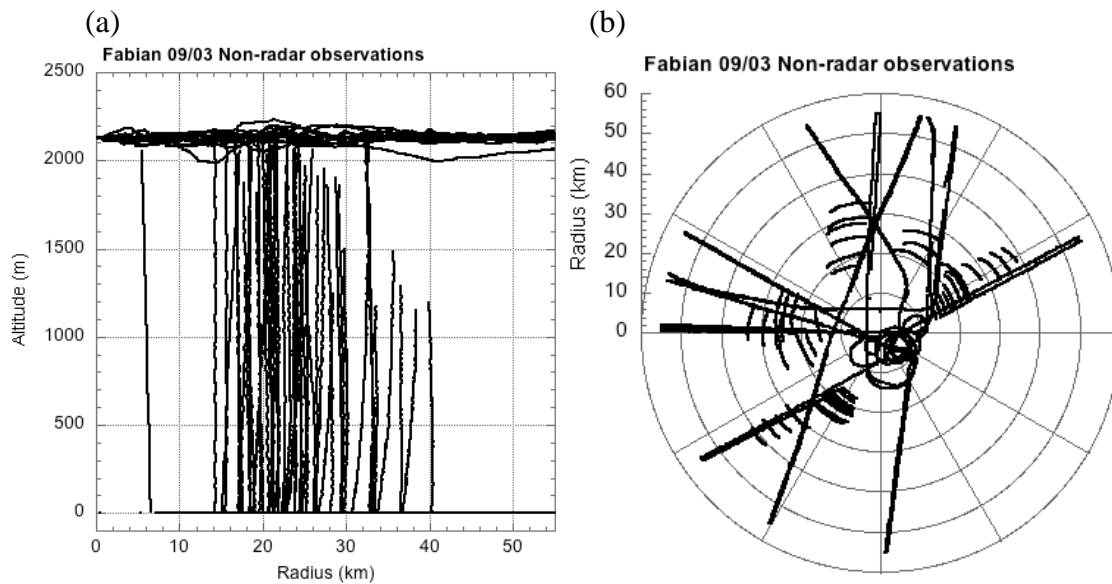
Figure 39. Spatial distribution of observations on 3 September. Non-radar observations in the (a) radius-height plane and (b) in the radius-theta plane.
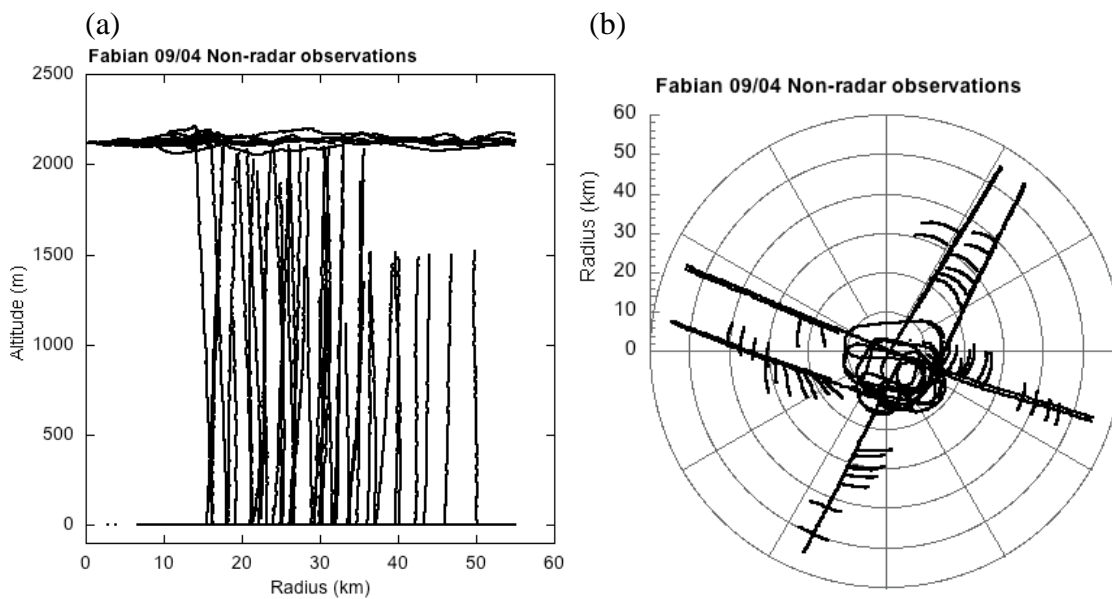


Figure 40. Spatial distribution of observations on 4 September. Non-radar observations in the (a) radius-height plane and (b) in the radius-theta plane.
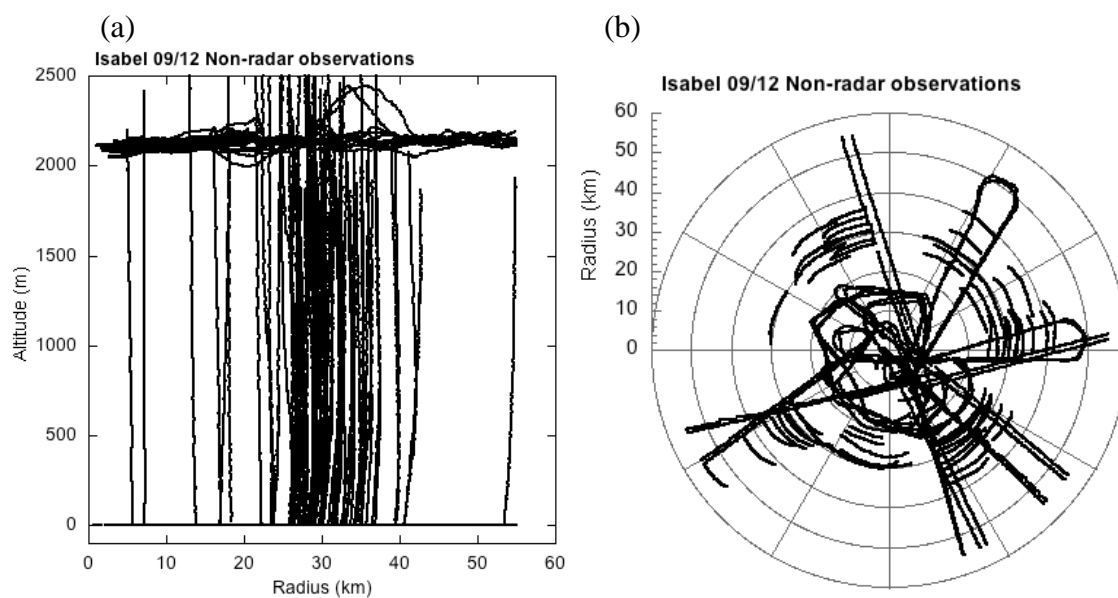
Figure 41.         Spatial distribution of observations on 12 September. Non-radar observations
                  in the (a) radius-height plane and (b) in the radius-theta plane.
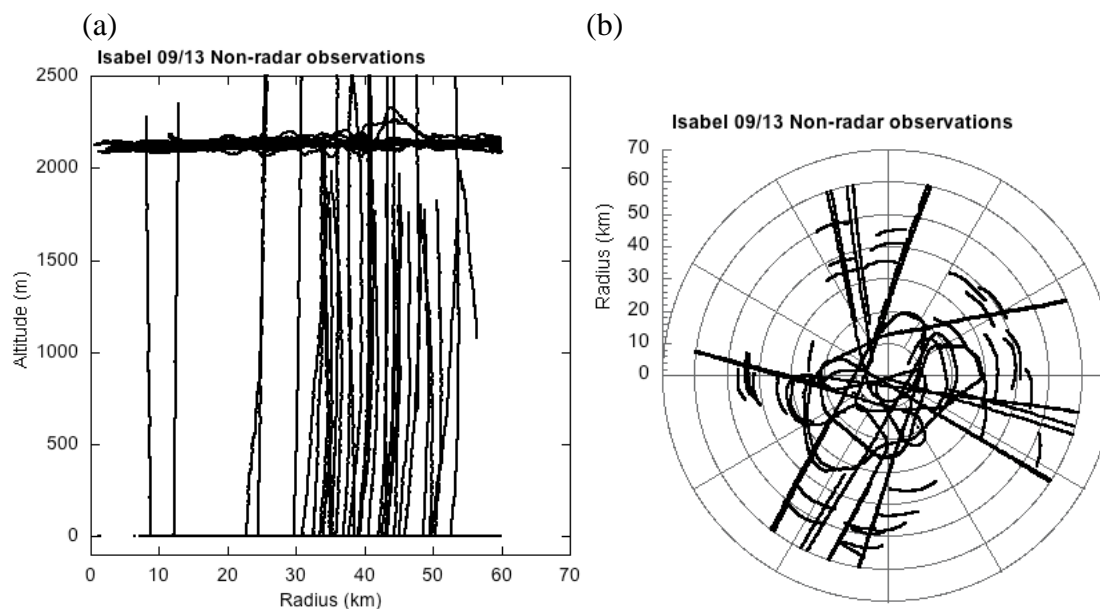


Figure 42.         Spatial distribution of observations on 13 September. Non-radar observations
                  in the (a) radius-height plane and (b) in the radius-theta plane.
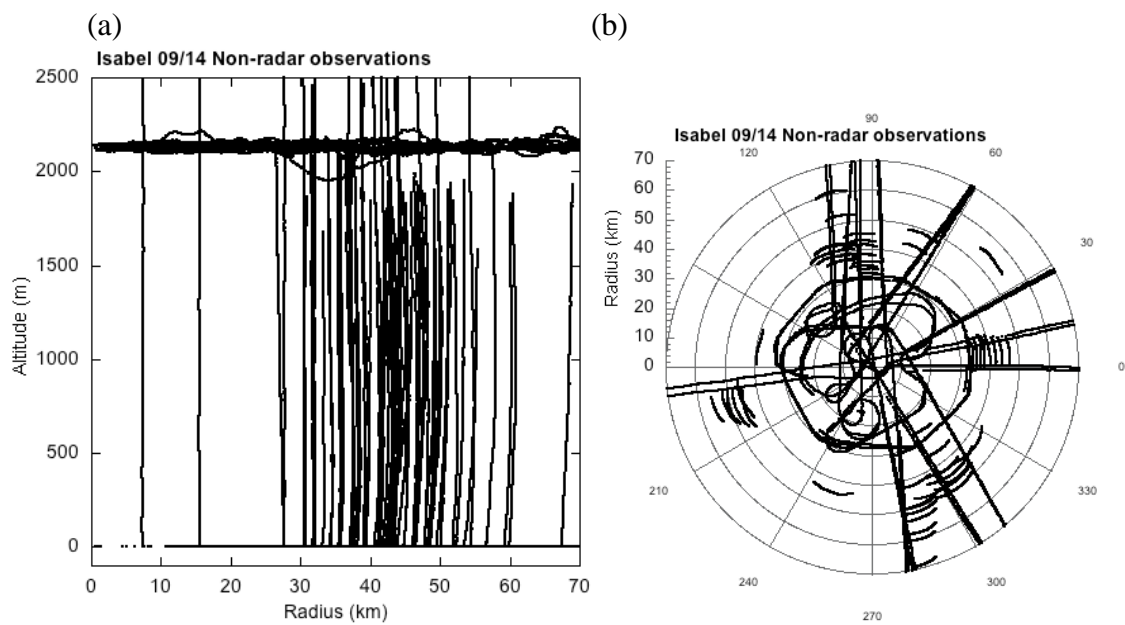
Figure 43.    Spatial distribution of observations on 14 September. Non-radar observations in the (a) radius-height plane and (b) in the radius-theta plane.
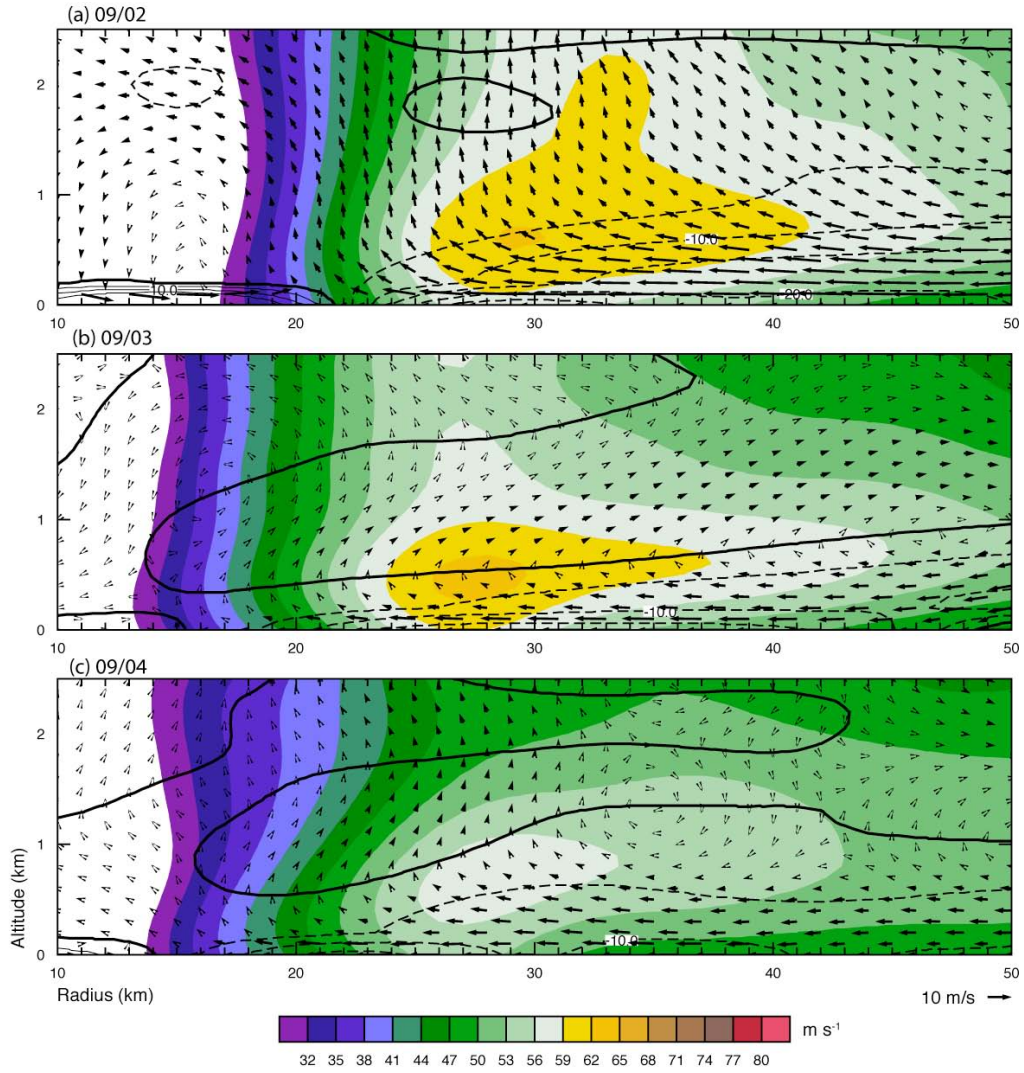
Figure 44.    Fabian axisymmetric tangential wind (color), radial wind (contour), and secondary circulation (vectors) from 2–4 September.
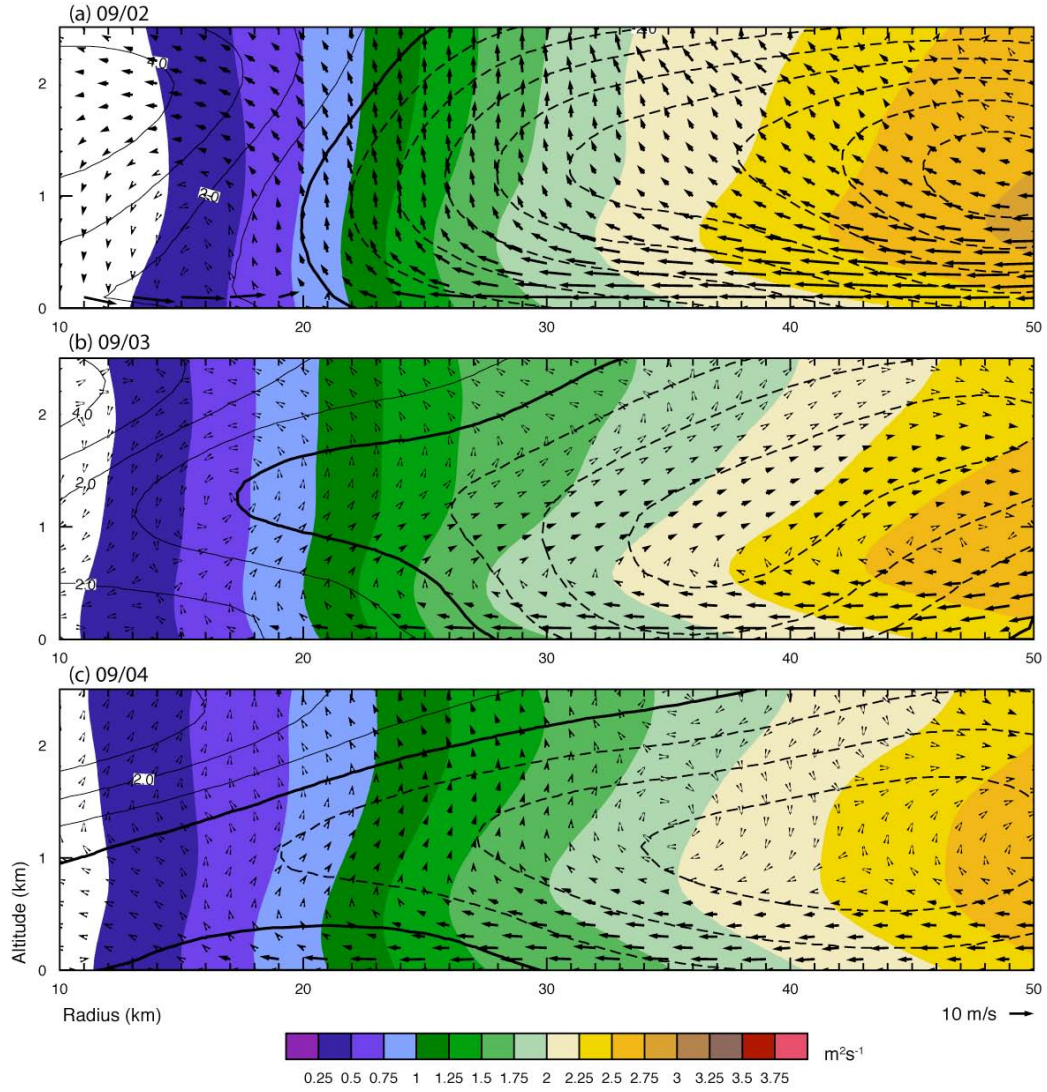
Figure 45.    Fabian axisymmetric angular momentum (color), total energy (350 kJ kg$^{-1}$ + 1 kJ kg$^{-1}$ contours), and secondary circulation (vectors) from 2–4 September.
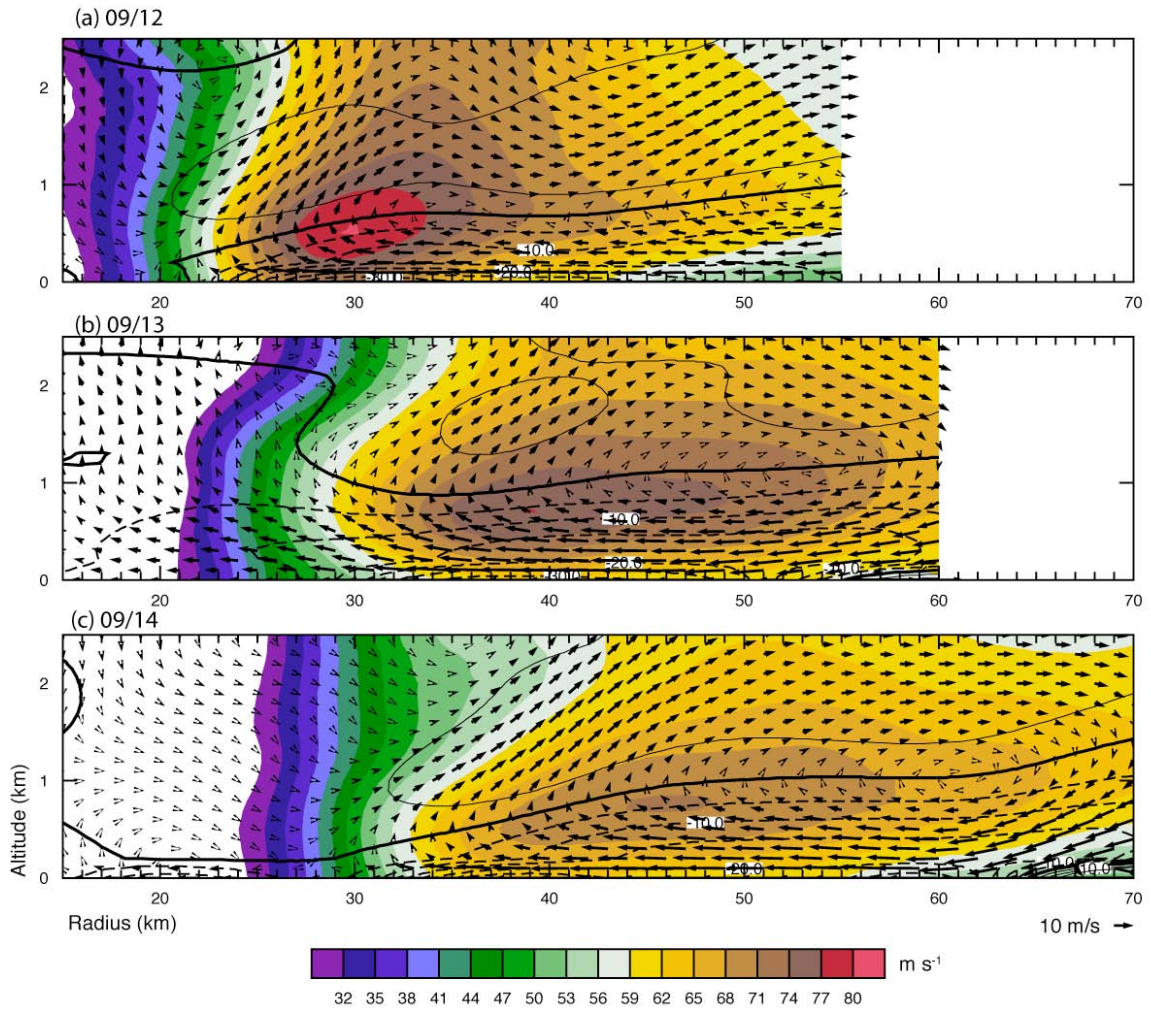
Figure 46.    Isabel axisymmetric tangential wind (color), radial wind (contour), and secondary circulation (vectors) from 12–14 September.
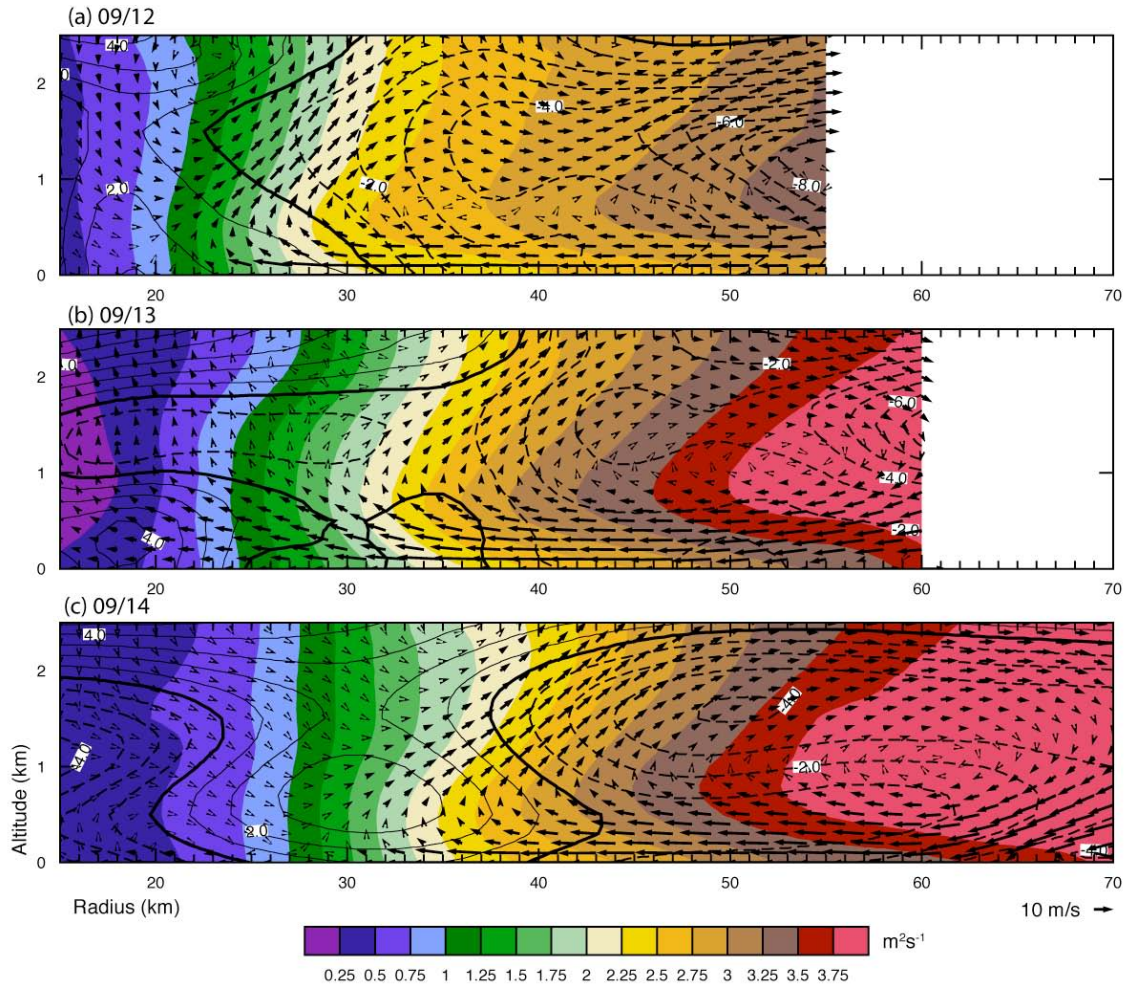
Figure 47.    Isabel axisymmetric angular momentum (color), total energy (350 kJ kg$^{-1}$ + 1 kJ kg$^{-1}$ contours), and secondary circulation (vectors) from 12–14 September.

Table 6.    Statistical differences between analysis and all observations. Units of observations are listed in Table 5.

| Mission | 2-Sep | 3-Sep | 4-Sep | 12-Sep | 13-Sep | 14-Sep |
|---|---|---|---|---|---|---|
| # Obs x10$^5$ | 7.1105 | 8.5040 | 5.4717 | 9.8731 | 6.5533 | 17.448 |
| Minimum | -42.912 | -37.362 | -29.793 | -53.507 | -67.852 | -43.795 |
| Maximum | 41.45 | 41.632 | 36.762 | 41.57 | 71.787 | 34.927 |
| Mean | -0.5821 | -0.50257 | -0.29302 | -0.1334 | -0.13643 | -0.3121 |
| Median | -0.5448 | -0.4461 | -0.2477 | -0.24437 | -0.069 | -0.35765 |
| RMS | 5.0665 | 4.8648 | 5.1959 | 5.0483 | 6.1022 | 4.7359 |
| Skewness | 0.01482 | 0.16971 | 0.19735 | 0.10709 | 0.16345 | 0.089939 |
| Kurtosis | 1.5122 | 2.0388 | 0.60577 | 3.2448 | 13.503 | 1.4067 |
| Correlation | 0.99129 | 0.99192 | 0.98862 | 0.99317 | 0.99099 | 0.99342 |

## C.    AIR-SEA FLUXES

The angular momentum and total energy budgets were resolved using the SAMURAI-derived storm structures shown in the previous section. A range of control volume depths near the top of the inflow layer from 400–1000 m was utilized, with the lowest level at both the surface and at 100 m height. Control volume widths from 10–22 km in 2 km increments were then prescribed, such that the aspect ratio of the volume remained in the 20–30 interval suggested by the sensitivity analysis. The inner radius of the volume was then varied by 2-km increments around a central value of 0.8 normalized inner radius, which yields a total of 72 flux "samples" per mission. An example of the control volumes used on 12 September is shown in Figure 48. These volumes spanned the region in and around the eyewall, such that the average wind speed in the volume was always above 50 m s$^{-1}$ for every mission. This spectrum of control volumes adequately represents a reasonable range of shapes and sizes for obtaining a mean and standard deviation of the budget residual at the eyewall on each day. The exchange coefficient sensitivity to the control volume parameters in this range was similar to that derived from the numerical simulations, with the exception of the WRF $C_K$ depth sensitivity. A weak decreasing trend in $C_K$ with increasing volume depth was deduced from the observations, whereas no distinct decrease above 400 m depth was found as in the WRF simulations. Results with a fixed 1 km control volume top were within 10% and 20% of the mean $C_D$ and $C_K$ values over all depths, respectively.

The retrieved surface stress values are shown in Figure 49. Although considerable spread exists in the individual samples, a general agreement in the stress magnitudes is found with a mean value of 9.4 and standard deviation of 4.6 N m$^{-2}$. A linear fit of the data has a correlation coefficient of 0.22 and only a slight upward trend with wind speed. Missions on 2 and 13 September have the highest stress, but also have two of the deepest inflow layers. The 14 September analysis also has a deep inflow layer, but with a stress more similar to the other missions. As will be shown below, the 12 September retrieval has an anomalously high $C_K/C_D$ ratio compared to the other missions, which suggests that the retrieved stress is possibly too low. It is not clear that this retrieval is an outlier, but more likely that the scatter is due to inherent uncertainties that were revealed in the

sensitivity analysis. Removing this mission from the sample improves the correlation coefficient to 0.53, and results in a more distinct upward trend with wind speed. Dividing by the density integral and taking the square root yields the friction velocity, which is shown in Figure 50. The scatter is less than in the stress retrieval due to the square root dependence, with a mean value of 2.8 m s$^{-1}$ and a 0.7 m s$^{-1}$ standard deviation. These estimates also indicate a slight upward trend with wind speed with a correlation of 0.24, or 0.53 with the 12 September mission removed.

The retrieved enthalpy flux is shown in Figure 51. These are the first known estimates of the enthalpy flux at wind speeds greater than 50 m s$^{-1}$, and likely the highest estimates of heat flux recorded over the ocean surface. There is less scatter than in the stress retrieval, and an increasing linear correlation with wind speed of 0.81. While some of the individual samples clearly are too low (near zero on 3 September) and too high (4000 W m$^{-2}$ on 12 September), the mean enthalpy flux for each mission and trend appears reasonable, with a variation from 764 W m$^{-2}$ at 52 m s$^{-1}$ to 2189 W m$^{-2}$ at 72 m s$^{-1}$. The reasons for the reduced scatter and better correlation in the energy budget compared to the momentum budget are not apparent but, given the high variability in the fluxes from numerical model simulations, this result also is not too disconcerting. It would appear that the derived thermodynamic structure was steadier on the ~6 hour mission timescale than the kinematic structure, but it is impossible to validate this with the current dataset.

The derived drag and enthalpy exchange coefficients are shown in Figure 52. The relatively low scatter of both results is very good considering the potential errors, and the enthalpy exchange coefficients have a better agreement than do the drag coefficients, as would be expected from the previous retrievals. The mean drag coefficient is 2.4 x10$^{-3}$ with a standard deviation of 1.1 x10$^{-3}$, which corresponds to ±46% uncertainty at the 67% confidence level, and a ±93% uncertainty at the 95% confidence level. The mean enthalpy exchange coefficient is 1.0 x10$^{-3}$ with a standard deviation of 0.4 x10$^{-3}$, which is a ±40% uncertainty at the 67% confidence level, and an ±80% uncertainty at the 95% confidence level. These percentage uncertainties are consistent with the sensitivity

analysis in Chapter III that indicated a ~50% standard deviation primarily associated with the neglected budget terms. The drag coefficient results do not indicate a significant wind speed dependence, with only a slightly decreasing linear correlation of only 0.11. The enthalpy coefficient shows a slight increase with wind speed, with a slope of 0.03 $(m\ s^{-1})^{-1}$ and a higher linear correlation of 0.53. Given the uncertainties and the weak slopes of both fits, there is no statistically significant change in either the drag or enthalpy coefficient in this wind speed range.

Histograms of the $C_D$ and $C_K$ samples (Figure 53) suggest that the distribution of the samples is similar and approximately normal in both cases. Low right skewness (0.56 and 0.45 for $C_D$ and $C_K$, respectively) with a slightly rounder peak than normal and negative kurtosis (-0.58 and -0.12, respectively) are found for both coefficients. These distributions yield good confidence that the sample mean values of the distribution are representative of the actual mean bulk exchange coefficients at these wind speeds, with the majority of the variability attributable to random errors associated with the uncertainties examined in Chapter III. The positive skewness suggests that there may be a small low bias in the mean, but this uncertainty is well within the standard deviation of the samples. The cumulative probability distribution (Figure 53, right) graphically illustrates the probability that the exchange coefficients are at or below a particular magnitude. The drag coefficient has a steep slope above 1 $x10^{-3}$, with ~50%, 70%, and 90% probabilities that $C_D$ is less than 2, 3, and 4 $x10^{-3}$, respectively. The maximum estimated drag coefficient is less than 5 $x10^{-3}$ with 99% probability, although this outlier estimate is not that useful given prior estimates' magnitude (Chapter II.B). The slope of the $C_K$ distribution is much flatter than the drag coefficient distribution. The maximum estimated enthalpy exchange coefficient is 2 $x10^{-3}$ with 99% probability, with an ~60% probability that the value is less than 1 $x10^{-3}$. These probabilities assume that the 432 samples obtained from varying the control volume over each of the six missions accurately represent samples from the true population distribution of exchange coefficient magnitudes. Since the numerical simulation sensitivity tests indicated that the uncertainties associated with these control volumes may be similar to those obtained with

the real data, and the other error sources are also primarily random over the six missions, this is believed to be a fair assumption.

Dividing the mean $C_K/C_D$ gives an average ratio of 0.4, with a variation from 0.17 to 1.05 by adding and subtracting a single standard deviation to each coefficient in each direction. The ratios of $C_K/C_D$ calculated from the different samples and the cumulative probability distribution are shown in Figure 54. With the exception of 12 September, the retrieved ratios are in relatively good agreement. The mean value of all individually calculated ratios is 0.48 with a standard deviation of 0.27, which is similar to the 0.4 ratio and uncertainty obtained by dividing the mean $C_K$ and $C_D$ from all the samples. A linear fit shows an increasing ratio with wind speed with a correlation of 0.58, but this is primarily due to the large ratios above 70 m s$^{-1}$. It is unclear why the 12 September mission appears to be an outlier, but this is probably due to unresolved errors as opposed to a significant change in the ratio above 70 m s$^{-1}$. It cannot be ruled out that the drag coefficient is reduced at these wind speeds. Since the enthalpy exchange coefficient for this mission agrees well with the other five, the drag coefficient derived for this day probably is too low, although this discrepancy could be because Hurricane Isabel may have undergone an eyewall replacement cycle shortly after this mission, and this cycle was accompanied with a change in the angular momentum structure and a larger integrated budget tendency term. Even with this mission included, the cumulative probability distribution of all $C_K/C_D$ ratios indicates an ~80% probability that the ratio is less than 0.75, and a 93% probability it is less than 1.0. Without the 12 September values these probabilities increase to 91% and 97%, respectively (not shown).
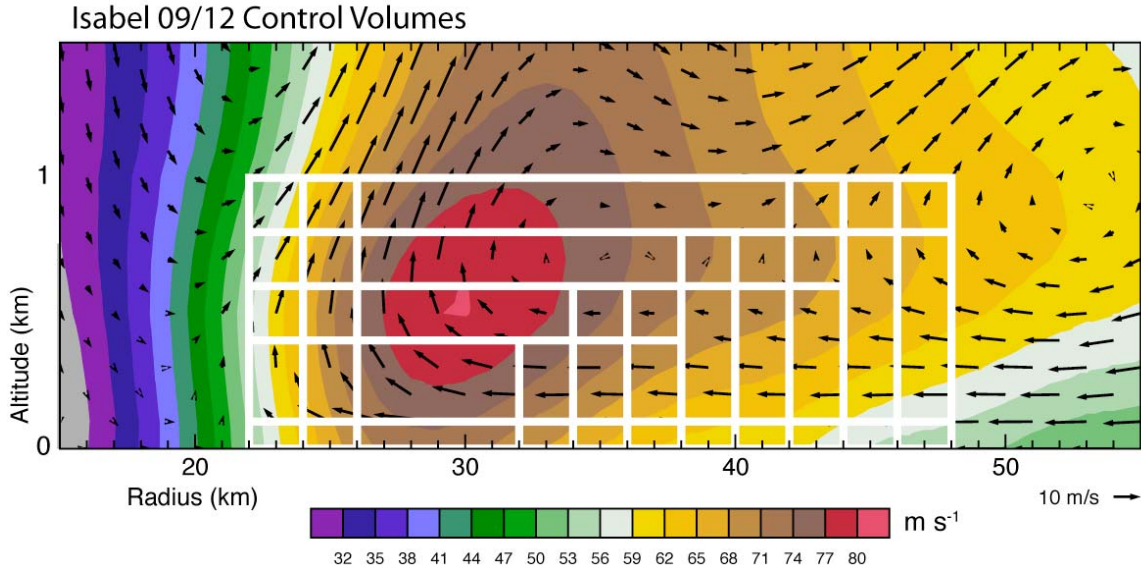
Figure 48.      Control volumes used for flux retrieval on 12 September. Tangential wind (color) and secondary circulation (vectors) are shown for reference.
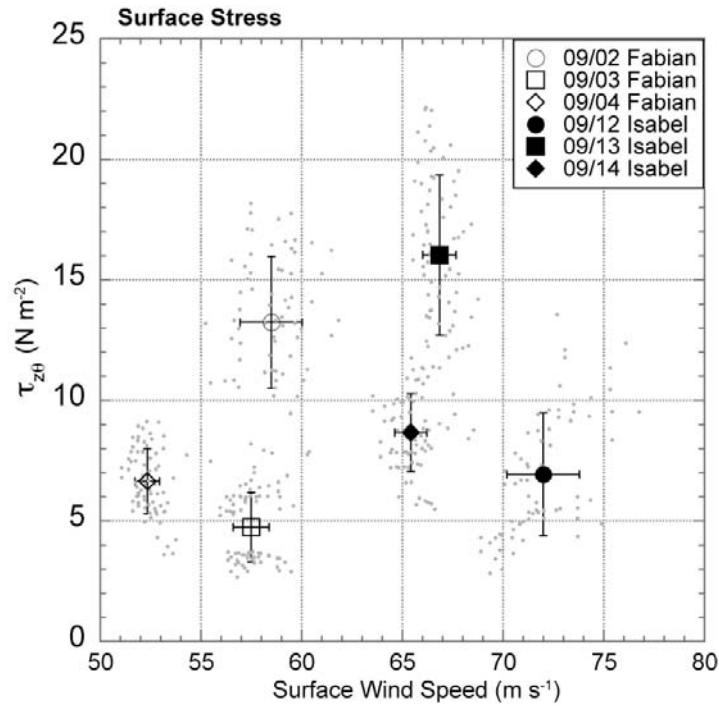


Figure 49.      Derived surface stress ($\tau_{z\theta}$) from budget retrieval. Gray dots indicate individual samples from different control volumes, and large symbols indicate mean values from each research mission. Error bars indicate one standard deviation in $\tau_{z\theta}$ (vertical) and average surface wind speed (horizontal).

114
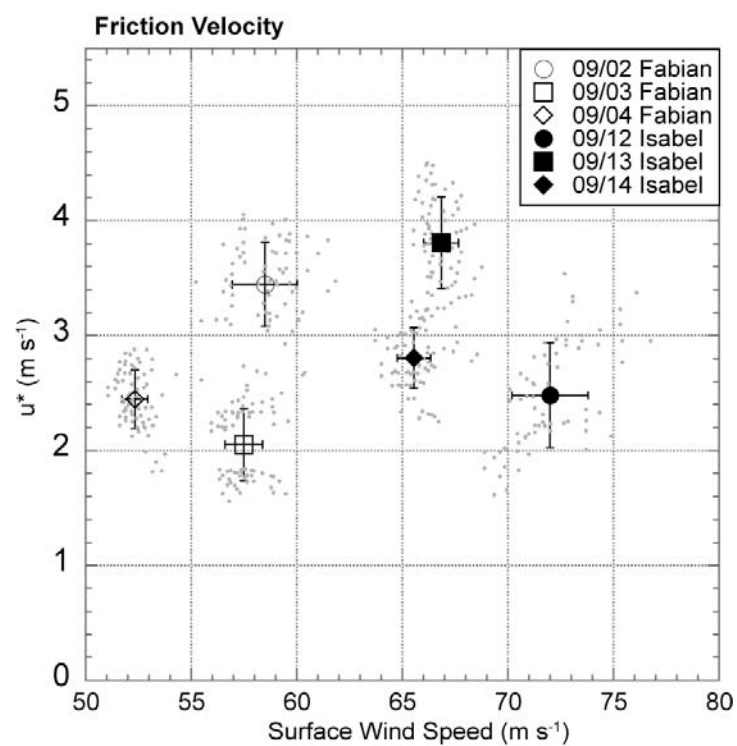
Figure 50.     As in Figure 49, except derived friction velocity (u*) from budget retrievals.
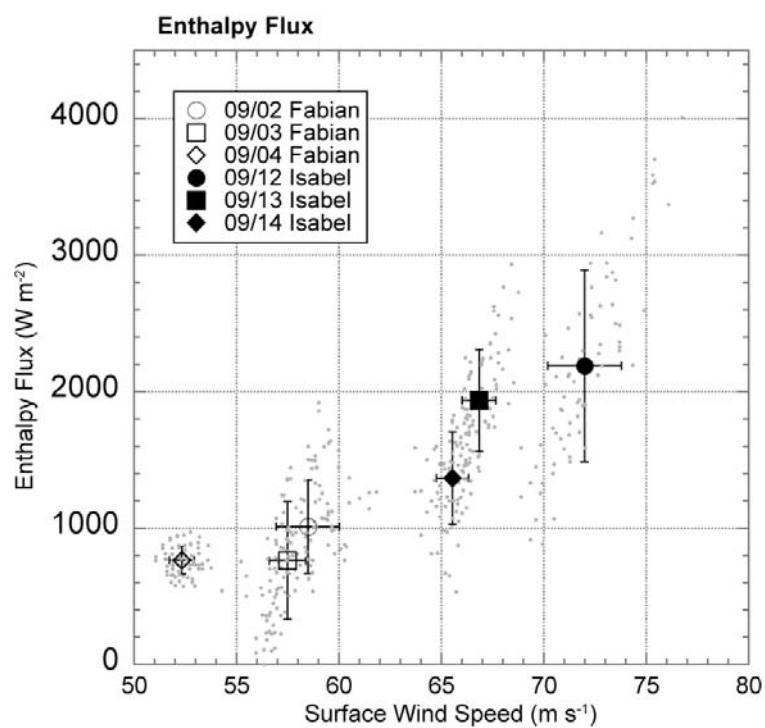


Figure 51.     As in Figure 49, except derived enthalpy flux from budget retrievals

115
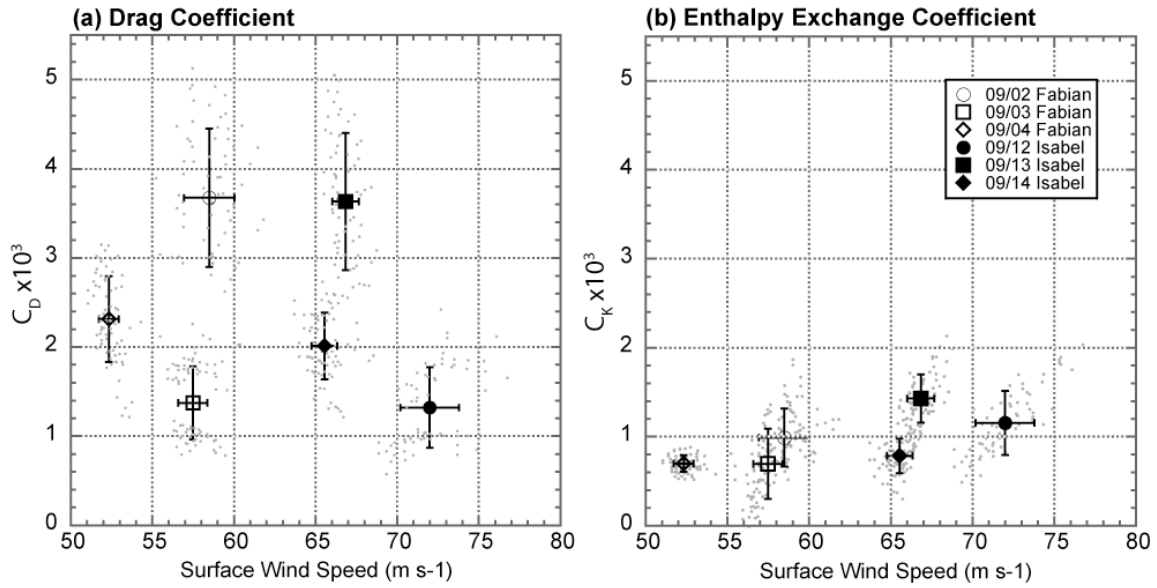
Figure 52.    As in Figure 49, except derived bulk exchange coefficients from budget retrievals.
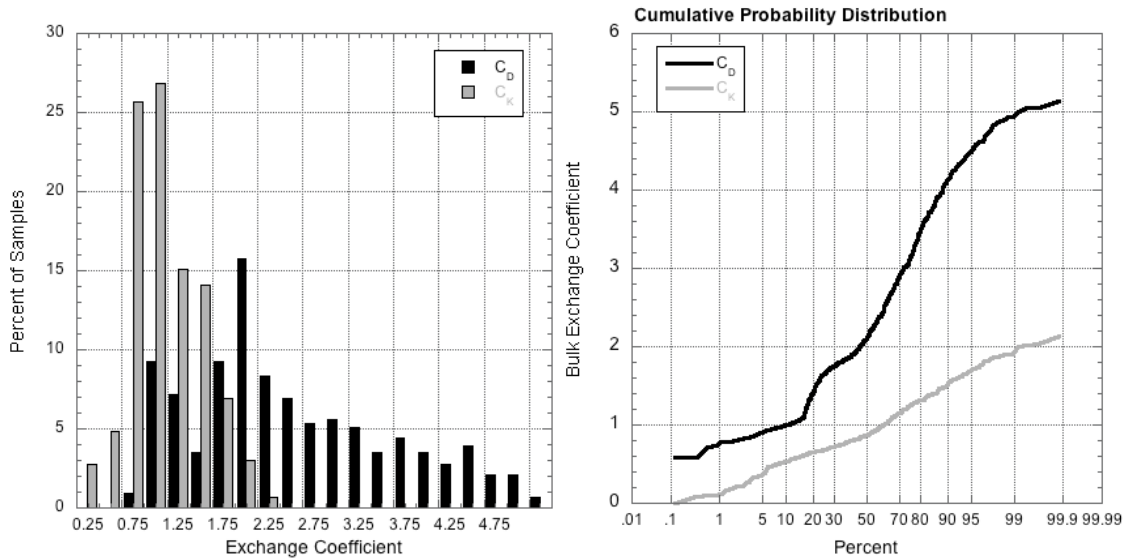


Figure 53.    Histogram of the percentage of samples in $0.5 \times 10^{-3}$ bins for $C_D$ (black) and $C_K$ (gray) for all retrievals (left). Cumulative probability distributions for $C_D$ (black) and $C_K$ (gray) retrievals (right).
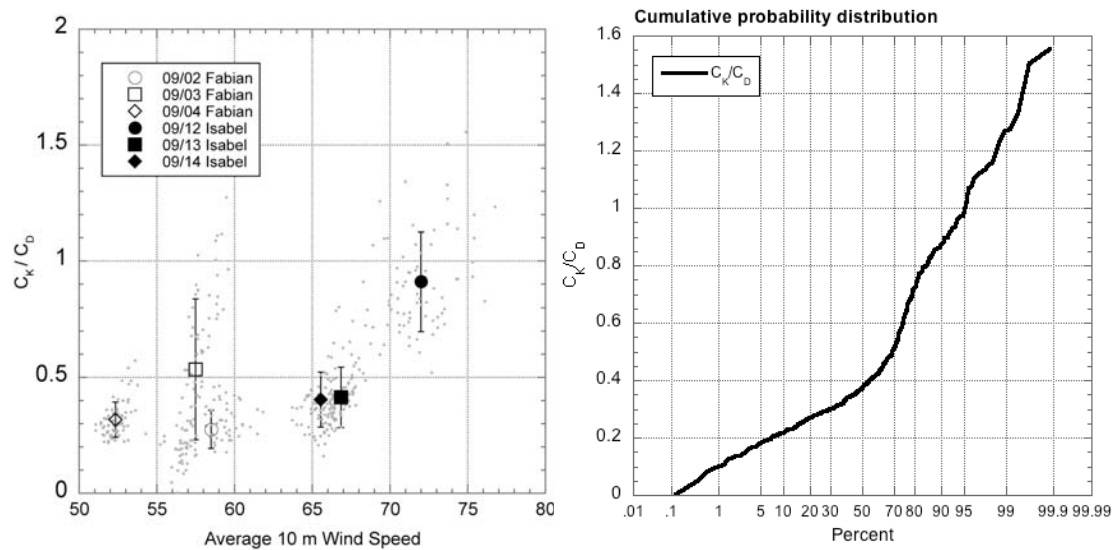
Figure 54.     Ratio of $C_K/C_D$ from budget method. Left panel has symbols as in Figure 49. Right panel shows cumulative probability distribution from all samples.

THIS PAGE INTENTIONALLY LEFT BLANK

# VI.  SUMMARY AND CONCLUSIONS

The magnitude of surface fluxes in major hurricanes has been very difficult to determine, and the resulting uncertainty remains an important aspect of both research and operations involving tropical cyclones. For the first time, enthalpy fluxes, the bulk enthalpy exchange coefficient, and the ratio of $C_K/C_D$ have been estimated at major hurricane wind speeds using a budget methodology. The results presented in this study also augment the limited stress and drag coefficient estimates above 50 m s$^{-1}$. This study improves upon previous studies using a budget method for estimating the surface fluxes in hurricanes by expanding the budgets to include total energy, by using improved data quality and quantity, by the use of a more sophisticated analysis technique, and by including a comprehensive error analysis. The six CBLAST missions into major Hurricanes Fabian and Isabel provided a unique opportunity to apply this budget method at a range of surface wind speeds from 52–72 m s$^{-1}$ and to obtain a good statistical sampling of flux retrievals. The new variational analysis scheme called SAMURAI was developed from first principles to determine the maximum likelihood estimate of the axisymmetric structure for the budgets by incorporating flight level, dropsonde, SFMR, and Doppler radar data. Although the derived exchange coefficients have some uncertainty, the sensitivity analysis using simulated data has allowed for a mitigation of some of the very large potential errors, and provides confidence in the quantitative uncertainty estimates. The main sources of error identified were: residuals in the mass continuity equation; unresolved volume-integrated tendency terms; unresolved vertical eddy flux terms at the top of control volume; sea-surface temperature errors; circulation center errors; and analysis errors. The "shear flux" term also was found to be important in the energy budget, and was included through an estimate of the drag coefficient obtained from the angular momentum budget. A total of 432 samples from 72 control volumes over the six analysis days provides a good sampling of the data that takes into account errors associated with the budget retrieval.

Estimates of the drag coefficient from the current research in relation to previous studies are shown in Figure 55. The black symbols are taken from French et al. (2007)

that represent the eddy correlation CBLAST estimates and the laboratory estimates from Donelan et al. (2004). The blue symbols are taken from Vickery et al. (2009) showing the flux-profile estimates obtained from dropsondes. The current results are shown in green, along with 95% confidence intervals. Although the spread in the budget estimates from this study is non-trivial, the retrieved magnitudes are in general agreement with the previous studies that the drag coefficient does not continue to increase beyond ~30 m s$^{-1}$. At the upper end of the 95% confidence level, the mean drag coefficient from some of the runs is near the extrapolated Large and Pond (1981) curve (dash-dot black curve), but the mean drag coefficient averaged over all the samples is lower at 2.4 x10$^{-3}$ with a ±46% uncertainty at the 67% confidence level. At the edge of the probability distribution, the 93% uncertainty at the 95% confidence level does not preclude the possibility that the drag coefficient is near the extrapolated value, but the cumulative distribution indicates that the magnitude has a 90% probability of being less than 4 x10$^{-3}$.

The individual enthalpy exchange coefficient samples are shown with previous estimates in Figure 56. A similar degree of scatter exists in the present results as those from the HEXOS and CBLAST eddy correlations, and the mean value of 1.0 x10$^{-3}$ with an ±80% uncertainty at the 95% confidence level is very similar to both the field and laboratory results. The good 0.81 linear correlation of the enthalpy flux with wind speed, and consistency of the exchange coefficients from the different missions yields good confidence in these results. Viewed as percentage errors, the uncertainty in the drag and the enthalpy exchange coefficients is similar. However, the enthalpy coefficient has a lower uncertainty in terms of absolute error. A linear fit of the enthalpy coefficient indicates a slight increase with wind speed above 50 m s$^{-1}$, but this increase is well within the uncertainty range and cannot be concluded definitively. This statistical sample indicates that the enthalpy coefficient has an ~70% probability of being equal to or less than 1.2x10$^{-3}$, which is the approximate value determined at wind speeds greater than 15 m s$^{-1}$. These results suggest that it is probable that the enthalpy exchange coefficient is not dependent on wind speed in hurricane conditions. Since the current results implicitly include the effects of sea spray, this would also suggest that spray effects do not change the enthalpy exchange coefficient. One hypothesis is that the spray flux has simply

replaced the interfacial flux at these wind speeds, which leads to a similar overall enthalpy flux. However, this cannot be assessed by the current methodology.

The results from this study have several theoretical and practical implications. The magnitudes of the drag and enthalpy exchange coefficients above 50 m s$^{-1}$ provide some support of the similarity hypothesis of Emanuel (2003) that the drag and enthalpy coefficients would remain constant at extreme wind speeds. The retrieved $C_K/C_D$ ratios from the present study are shown with previous estimates in Figure 57. These results indicate that the ratio is likely less than the ~1.0 estimate derived by Emanuel (2003) at the ~28 C temperature range, and perhaps may be as low as 0.4. The uncertainty in the coefficients and limited sea-surface temperature range precludes testing of the hypothesis that the enthalpy exchange coefficient is SST-dependent. There is an ~80% probability from these retrievals that the ratio is less than the 0.75 ratio proposed as a threshold for hurricane development by Emanuel (1995). Recent theoretical and computational analyses suggest that this discrepancy is largely due to gradient wind imbalance in the boundary layer (Smith et al. 2008; Bryan and Rotunno 2009). These results are also consistent with recent three-dimensional numerical simulations that intensified to major hurricane status with $C_K/C_D$ ratios as low as 0.1 (Montgomery et al. 2010). Although evidence is accumulating that potential intensity may not be as sensitive to $C_K/C_D$ as originally formulated, this does not diminish the importance of having accurate estimates of these parameters at major hurricane wind speeds. These results suggest that the lower bound of the E-PI range for Hurricane Isabel presented in BM08 would be the most accurate (c.f., their Figure 1), which yields potential intensity estimates below 50 m s$^{-1}$. These new estimates of $C_K$ and $C_D$ should help to improve potential intensity theory and understanding of tropical cyclone intensity change. From a modeling perspective, these estimates should provide additional confidence in an improved physical basis for surface layer schemes that do not increase the drag or enthalpy coefficient as the wind speeds increase above 50 m s$^{-1}$. A continued examination of the physics parameterizations at high wind speeds in WRF and COAMPS, especially the new COAMPS-TC that is currently under development, will be conducted as part of future research.

Several additional areas beyond this study deserve further attention. With this proof of concept in place, fluxes in other storms with sufficient research data quality could be examined to improve the statistical sampling and potentially expanding the wind speed ranges presented in this paper. Several tropical cyclones with good reconnaissance and research data exist that would be candidates. In order to improve the method, the budget error analysis indicates that two of the largest sources of error are the unresolved tendency term and circulation center errors. One possible approach would be to relax the axisymmetric constraint, and reformulate the budgets in a Cartesian coordinate system centered on a particular region of the storm. This would remove truncation errors associated with the axisymmetric cylindrical transform, but would likely increase errors associated with the unresolved terms. If multiple passes could be conducted through a region, the tendency term could be estimated on relatively short timescales. The inclusion of radar data to completely document the kinematics in the control volume would be optimal. Since it is unclear whether this approach would reduce the uncertainty, a comprehensive sensitivity analysis similar to the one conducted herein is recommended. Lastly, the SAMURAI analysis package will continue to be developed, with a natural extension to three dimensions and the Cartesian domain, and with the addition of other data sources and analysis variables that are relevant for mesoscale studies. The usefulness of the software for tropical cyclone data assimilation applications with numerical weather models also will be investigated.
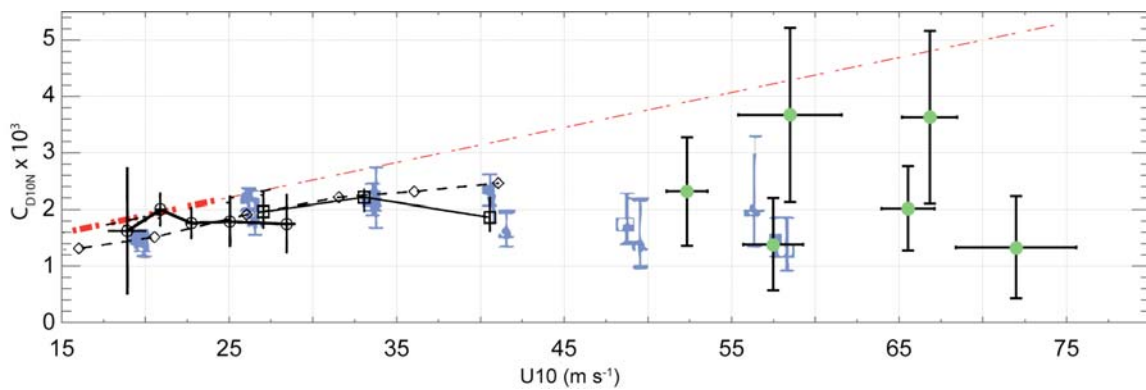


Figure 55.    Mean drag coefficients from this study (green circles) compared with previous studies. Black symbols adapted from French et al. (2007) and blue symbols adapted from Vickery et al. (2009). Red line indicates measured (thick) and extrapolated (thin) Large and Pond (1981) drag coefficient.
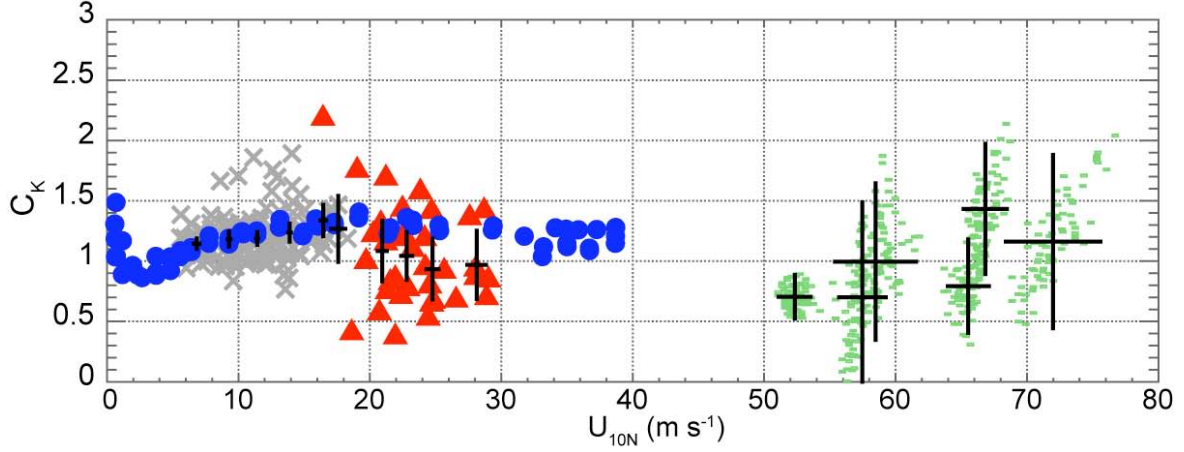
Figure 56.    Wind speed dependence of $C_K$ from this study (green squares) compared with previous studies as summarized by Haus et al. (2010). ASIST laboratory results (blue circles) and CBLAST (red triangles) measurements shown with HEXOS results (gray x's). The mean and 95% confidence intervals are shown in black.
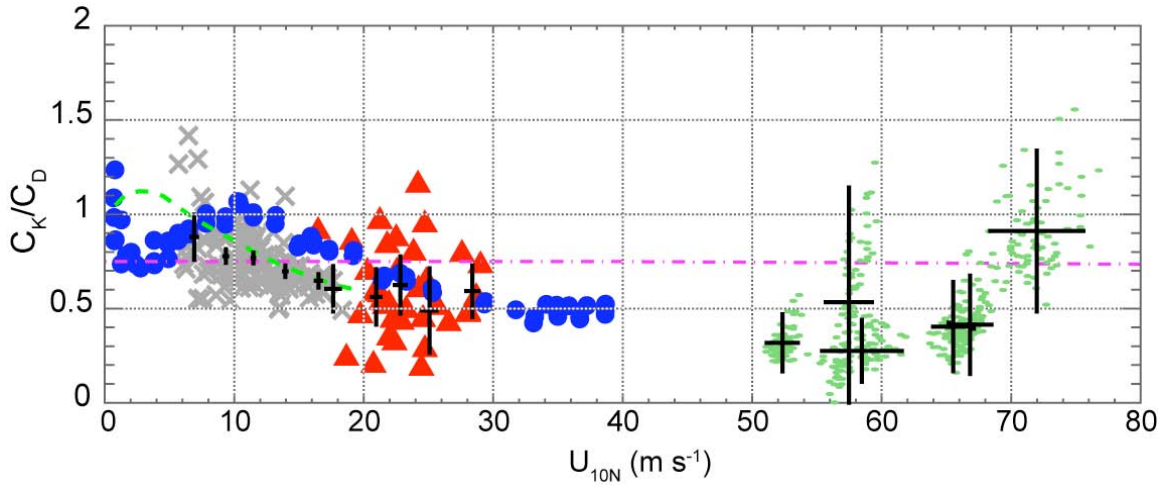


Figure 57.    Wind speed dependence of $C_K/C_D$ from this study (green squares) compared with previous studies as summarized by Haus et al. (2010). ASIST laboratory results (blue circles) and CBLAST (red triangles) measurements shown with HEXOS results (gray x's). The mean and 95% confidence intervals are shown in black. Purple dashed line indicates 0.75 ratio.

123

THIS PAGE INTENTIONALLY LEFT BLANK

# LIST OF REFERENCES

Aberson, S. D., M. T. Montgomery, M. Bell, and M. Black, 2006: Superintense winds in hurricane Isabel (2003). Part II: Extreme wind speeds. *Bull. Amer. Met. Soc.*, **87**, 1349–1354.

Atlas, D., R. C. Srivastava, and R. S. Sekhon, 1973: Doppler radar characteristics of precipitation at vertical incidence. *Rev. Geophys. Space Phys.*, **11,** 1–35.

Bao, J.-W., S. A. Michelson, and J. M. Wilczak, 2002: Sensitivity of numerical simulations to parameterizations of roughness for surface heat fluxes at high winds over the sea. *Mon. Wea. Rev.,* **130**, 1926–1932.

Bargen, D. W., and R. C. Brown, 1980: Interactive radar velocity unfolding. *Preprints, 19th Conference on Radar Meteorology, Miami Beach, Amer. Meteor. Soc.,* 278–285.

Barnes, S. L., 1973: Mesoscale objective analysis using weighted time-series observations. NOAA Tech. Memo. ERL NSSL-62, National Severe Storms Laboratory, Norman, OK 73069, 60 pp.

Beard, K., 1985: Simple altitude adjustments to raindrop velocities for Doppler radar analysis, *J. Atmos. and Oceanic Technol.*, **2**, 468–471

Bell, M. M., 2006: Observed structure, evolution, and potential intensity of category five Hurricane Isabel (2003) from 12–14 September. M.S. thesis, Dept. of Atmospheric Science, Colorado State University, 98 pp.

——, and M. T. Montgomery, 2008: Observed structure, evolution, and potential intensity of category five Hurricane Isabel (2003) from 12–14 September. *Mon. Wea. Rev.*, **136**, 2023–2045.

Black, M. L., R. W. Burpee, and F. D. Marks Jr., 1996: Vertical motion characteristics of tropical cyclones determined with airborne Doppler radial velocities. *J. Atmos. Sci.*, **53**, 1887–1909.

Black, M. L., E. A. D'Asaro, W. M. Drennan, J. R. French, P. P. Niiler, T. B. Sanford, E. J. Terrill, E. J. Walsh, and J. Zhan, 2007: Air-sea exchange in hurricanes: Synthesis of observations from the Coupled Boundary Layer Air-Sea Transfer experiment. *Bull. Amer. Met. Soc.*, **88**, 357–374.

Bosart, B. L., W.-C. Lee, and R. M. Wakimoto, 2002: Procedures to improve the accuracy of airborne Doppler radar data. *J. Atmos. Oceanic Technol.*, **19**, 322–339.

Braun, S. A., and W.-K. Tao, 2000: Sensitivity of high-resolution simulations of hurricane Bob (1991) to planetary boundary layer parameterizations. *Mon. Wea. Rev.*, **128**, 3941–3961.

Bryan, G. H., and R. Rotunno, 2009: The maximum intensity of tropical cyclones in axisymmetric numerical model simulations. *Mon. Wea. Rev.*, **137**, 1770–1789.

Courtier, P., J.-N. Thepaut, and A. Hollingsworth, 1994: A strategy for operational implementation of 4D-VAR, using an incremental approach. *Quart. J. Roy. Meteor. Soc*, **120**, 1367–1387.

Cram, T. A., J. Persing, M. T. Montgomery, and S. A. Braun, 2005: A Lagrangian trajectory view on transport and mixing processes between the eye, eyewall and environment using a high resolution simulation of Hurricane Bonnie (1998). *J. Atmos. Sci.*, **64**, 1835–1856.

Cressman, G. P., 1959: An operational objective analysis system. *Mon. Wea. Rev.*, **87**, 367–374.

Davis, C., W. Wang, S. Chen, Y. Chen, K. Corbosiero, M. DeMaria, J. Dudhia, G. Holland, J. Klemp, J. Michalakes, H. Reeves, R. Rotunno, C. Snyder, and Q. Xiao, 2008: Prediction of landfalling hurricanes with the Advanced Hurricane WRF model. *Mon. Wea. Rev.*, **136**, 1990–2005.

Deardorff, J. W., 1972: Parameterization of the planetary boundary layer for use in general circulation models. *Mon. Wea. Rev.*, **100**, 93–106.

DeCosmo, J., K. B. Katsaros, S. D. Smith, R. J. Anderson, W. A. Oost, K. Bumke, and H. Chadwick, 1996: Air–sea exchange of water vapor and sensible heat: The Humidity Exchange over the Sea (HEXOS) results. *J. Geophys. Res.*, **101**, 12001–12016.

Donelan, M. A., B. K. Haus, N. Reul, W. J. Plant, M. Stianssnie, H. C. Graber, O. B. Brown, and E. S. Saltzman, 2004: On the limiting aerodynamic roughness of the ocean in very strong winds. *Geophys. Res. Lett.,* **31,** L18306.

Drennan, W. M., J. A. Zhang, J. R. French, C. McCormick, and P. G. Black, 2007: Turbulent fluxes in the hurricane boundary layer. Part II: Latent heat flux. *J. Atmos. Sci.*, **64**, 1103–1115.

Eastin, M. D., P. G. Black, and W. M. Gray, 2002: Flight-level instrument wetting errors in hurricanes. Part I: Observations. *Mon. Wea. Rev.,* **130,** 825–841.380.

Emanuel, K.A., 1986: An air-sea interaction theory for tropical cyclones. Part I: Steady-state maintenance. *J. Atmos. Sci*. **43**, 585–604.

——, 1995: Sensitivity of tropical cyclones to surface exchange coefficients and a revised steady-state model incorporating eye dynamics. *J. Atmos. Sci.*, **52**, 3969–3976.

——, 2003: A similarity hypothesis for air–sea exchange at extreme wind speeds. *J. Atmos. Sci.*, **60**, 1420–1428.

French, J. R., W. M. Drennan, J. A. Zhang, and P. G. Black, 2007: Turbulent fluxes in the hurricane boundary layer. Part I: Momentum flux. *J. Atmos. Sci.*, **64**, 1089–1102.

Gao, J., M. Xue, K. Brewster, and K. K. Droegemeier, 2004: A three-dimensional variational data analysis method with recursive filter for Doppler radars. *J. Atmos. Oceanic Technol.*, **21**, 457–469.

Haus, B. K., D. Jeong, M. A. Donelan, J. A. Zhang, and I. Savelyev, 2010: Relative rates of sea-air heat transfer and frictional drag in very high winds. *Geophys. Res. Lett.*, **37**, L07802, doi:10.1029/2009GL042206.

Hausman, S. A., K. V. Ooyama, and W. H. Schubert, 2006: Potential vorticity structure of simulated hurricanes. *J. Atmos. Sci.*, **63**, 87–108.

Hawkins, H. F., and D. T. Rubsam, 1968: Hurricane Hilda, 1964. II. Structure and budgets of the hurricane on October 1, 1964. *Mon. Wea. Rev.* **96**, 617–636.

——, and S. M. Imbembo, 1976: The structure of a small, intense hurricane—Inez 1966. *Mon. Wea. Rev.* **104**, 418–442.

Hayden, C. M., and R. J. Purser, 1995: Recursive filter for objective analysis of meteorological fields: Applications to NESDIS operational processing. *J. Appl. Meteor*, **34**, 3–15.

Hong, S.-Y., Y. Noh, and J. Dudhia, 2006: A new vertical diffusion package with an explicit treatment of entrainment processes. *Mon. Wea. Rev.*, **134**, 2318–2341.

Huang, X.-Y., 2000: Variational analysis using spatial filters. *Mon. Wea. Rev*, **128**, 2588–2600.

Hock, T. F., and J. L. Franklin, 1999: The NCAR GPS dropwindsonde. *Bull. Amer. Meteor. Soc.*, **80**, 407–420.

Hughes, L. A., 1952: On the low-level wind structure of tropical storms. *J. Meteor.*, **9**, 422–428.

Jarosz, E., D. A. Mitchell, D. W. Wang, and W. J. Teague, 2007: Bottom-up determination of air–sea momentum exchange under a major tropical cyclone. *Science*, **315**, 1707–1709.

Jeong, D., B. K. Haus, and M. E. Donelan, 2010: Enthalpy transfer across the air-water interface in high winds including spray. *J. Atmos. Sci.,* submitted.

Jordan, C. L., 1952: On the low-level structure of the typhoon eye. *J. Meteor.*, **9**, 285–290.

——, 1958: Mean soundings for the West Indies area. *J. Meteor.*, **15**, 91–97.

Joss, J., and A. Waldvogel, 1970: A method to improve the accuracy of radar-measured amounts of precipitation. *Proc. 14th Radar Meteorology Conf.,* Tucson, AZ, Amer. Meteor. Soc., 237–238.

Keeler, R. J., and S. M. Ellis, 2000: Observational error covariance matrices for radar data assimilation. *Phys. Chem. Earth*, **25**, 1277–1280.

Kessler, E., 1969: On distribution and continuity of water substance in atmospheric circulations. *American Meteorological Society, Meteorol. Monogr.*, **10,** 32-84.

Kleinschmidt, E., 1951: Grundlagen einer theorie der tropischen zyklonen. *Arch. Meteorol. Geophys. Bioklimatol.*, **A4**, 53–72.

Large, W. G., and S. Pond, 1981: Open ocean momentum flux measurements in moderate to strong winds. *J. Phys. Oceanogr.*, **11**, 324–336.

——, and ——,, 1982: Sensible and latent heat flux measurements over the ocean. *J. Phys. Oceanogr.*, **12**, 464–482.

Lee, W-C., and F. D. Marks, 2000: Tropical cyclone kinematic structure retrieved from single Doppler radar observations. Part II: The GBVTD-simplex center finding algorithm. *Mon. Wea. Rev.*, **128**, 1925–1936.

Lorenc, A. C., 1986: Analysis methods for numerical weather prediction. *Quart. J. Roy. Meteor. Soc*, **112**, 1177–1194.

Malkus, J. S., and H. Riehl, 1960: On the dynamics and energy transformations in steady-state hurricanes. *Tellus*, **12**, 1–20.

Marks, F. D. Jr., R. A. Houze, and J. Gamache, 1992: Dual-aircraft investigation of the inner core of Hurricane Norbert. Part I: Kinematic structure. *J. Atmos. Sci.*, **49**, 919–942.

Miller, B. I., 1962: "On the momentum and energy balance of Hurricane Helene (1958)," *National Hurricane Research Project Report* No. **53,** U.S. Weather Bureau, Washington, D.C., 19 pp.

——, 1964: A study of the filling of Hurricane Donna 1960: Over land. *Mon. Wea. Rev.*, **92**, 389–406.

——, 1969: Experiments in forecasting hurricane development with real data. National Hurricane Research Laboratory Report, Miami, Fla., 28 pp.

Mohr, C. G., 1988: CEDRIC—Cartesian Space Data Processor. National Center for Atmospheric Research, Boulder, CO, 78 pp.

Montgomery, M. T., M. M. Bell, S. D. Aberson, and M. L. Black, 2006: Hurricane Isabel (2003): New insights into the physics of intense storms. Part I: Mean vortex structure and maximum intensity estimates. *Bull. Amer. Meteor. Soc.*, **87**, 1335–1347.

——, R. Smith, and S. Nguyen, 2010: Sensitivity of tropical cyclone models to the surface drag coefficient. *Quart. J. Roy. Meteor. Soc*, submitted.

Moss, M. S., and S. L. Rosenthal, 1975: On the estimation of planetary boundary layer variables in mature hurricanes. *Mon. Wea. Rev*, **103**, 980–988.

Nelder, J. A., and R. Mead, 1965: A simplex method for function minimization. *Comput. J.,***7**, 308–313.

Noh, Y., W. G. Cheon, S. Y. Hong, and S. Raasch, 2003: Improvement of the K-profile model for the planetary boundary layer based on large eddy simulation data. *Bound.-Layer Meteor.*, **107**, 421–427.

Nolan, D. S., M. T. Montgomery, and L. D. Grasso, 2001: The wavenumber-one instability and trochoidal motion of hurricane-like vortices. *J. Atmos. Sci*, **58**, 3243–3270.

Ooyama, K. V., 1969: Numerical simulation of the life cycle of tropical cyclones. *J. Atmos. Sci.*, **26**, 3–40.

——, 1987: Scale controlled objective analysis. *Mon. Wea. Rev.*, **115**, 2479–2506.

——, 2002: The cubic-spline transform method: Basic definitions and tests in a 1D single domain. *Mon. Wea. Rev.*, **130**, 2392–2415.

Palmén, E., and H. Riehl, 1957: Budget of angular momentum and energy in tropical cyclones. *J. Meteor*, **14**, 150–159.

Persing, J., and M. T. Montgomery, 2003: Hurricane superintensity. *J. Atmos. Sci.* **60**, 2349–2371.

Powell, M. D., P. J. Vickery, and T. A. Reinhold, 2003: Reduced drag coefficient for high wind speeds in tropical cyclones. *Nature*, **422**, 279–283.

Press, W. H., S. A. Teukolsky, W. T. Vetterling, and B. P. Flannery, 2002: *Numerical recipes in C++, the art of scientific computing*. Cambridge Univ. Press, 1002 pp.

Purser, R. J., W.-S. Wu, D. Parrish, and N. M. Roberts, 2003: Numerical aspects of the application of recursive filters to variational statistical analysis. Part I: Spatially homogeneous and isotropic Gaussian covariances. *Mon. Wea. Rev*, **131**, 1524–1535.

Rappaport, E. N., J. Franklin, L. Avila, S. Baig, J. Beven, E. Blake, C. Burr, J.-G. Jiing, C. Juckins, R. Kanbb, C. Landsea, M. Mainelli, M. Mayfield, C. McAdie, R. Pasch, C. Cisko, S. Stewart, and A. Tribble, 2009: Advances and challenges at the National Hurricane Center. *Wea. Forecasting*, **24**, 395–419.

Rotunno, R., and K. A. Emanuel, 1987: An air-sea interaction theory for tropical cyclones. Part II: Evolutionary study using a nonhydrostatic axisymmmetric model. *J. Atmos. Sci.* **44**, 542–561.

Rosenthal, S. L., 1971: The response of a tropical cyclone model to variations in boundary layer parameters, initial conditions, lateral boundary conditions, and domain size. *Mon.Wea. Rev.*, **99**, 767–777.

Shapiro, L. J., and J. L. Franklin, 1995: Potential vorticity in Hurricane Gloria. *Mon. Wea. Rev.*, **123**, 1465–1475.

Smith, S. D., R. J. Anderson, W. A. Oost, C. Kraan, N. Maat, J. DeCosmo, K. B. Katsaros, K. Burnke, L. Hasse, and H. M. Chadwick, 1992: Sea surface wind stress and drag coefficients: The HEXOS results. *Bound.-Layer Meteor.*, **60**, 109–142.

Smith, R. K., 2006: Accurate determination of a balanced axisymmetric vortex in a compressible atmosphere. *Tellus*, **58A**, 98–103.

——, M. T. Montgomery, and S. Vogl, 2008:A critique of Emanuel's hurricane model and potential intensity theory. *Quart. J. Roy. Meteor. Soc.*, **134**, 551–561.

——, and M. T. Montgomery, 2009: Hurricane boundary layer theory. *Quart. J. Roy. Meteor. Soc.*, in review.

Vickery, P. J., D. Wadhera, M. D. Powell, and Y. Chen, 2009: A hurricane boundary layer and wind field model for use in engineering applications. J. *Appl. Meteor. Climat.*, **48**, 381–405.

Wang, J., J. Bian, W. O. Brown, H. Cole, V. Grubisic, and K. Young, 2009: Vertical air motion from T-REX radiosonde and dropsonde data. *J. Atmos. and Oceanic Technol.,* **26**, 928–942.

Zhang, J. A., P. G. Black, J. R. French, and W. M. Drennan, 2008: First direct measurements of enthalpy flux in the hurricane boundary layer: The CBLAST results. *Geophys. Res. Lett.*, **35**, L14813. doi:10.1029/2008GL034374.

——, W. M. Drennan, P. G. Black, and J. R. French, 2009: Turbulence structure of the hurricane boundary layer between the outer rainbands. *J. Atmos. Sci.*, **66**, 2455–2467.

Zipser, E. J., R. J. Meitin, and M. A. LeMone, 1981: Mesoscale motion fields associated with a slowly moving GATE convective band. *J. Atmos. Sci.,* **38,** 1725–1750.

THIS PAGE INTENTIONALLY LEFT BLANK

# INITIAL DISTRIBUTION LIST

1.    Defense Technical Information Center
      Ft. Belvoir, Virginia

2.    Dudley Knox Library
      Naval Postgraduate School
      Monterey, California

3.    Michael Bell
      Naval Postgraduate School
      Monterey, California

4.    Michael Montgomery
      Naval Postgraduate School
      Monterey, California

5.    Kerry Emanuel
      Massachusetts Institute of Technology
      Cambridge, Massachusetts

6.    Patrick Harr
      Naval Postgraduate School
      Monterey, California

7.    Russell Elsberry
      Naval Postgraduate School
      Monterey, California

8.    Qing Wang
      Naval Postgraduate School
      Monterey, California

9.    Francis Giraldo
      Naval Postgraduate School
      Monterey, California

10.   Philip Durkee
      Naval Postgraduate School
      Monterey, California